High-power, continuous-wave optical parametric oscillators from visible to near-infrared

Goutam K. Samanta

Universitat Politècnica de Catalunya

Barcelona, March 2009

Doctorate Program: **Photonics**

Duration: **2006-2009.**

Thesis advisor: **Prof. Majid Ebrahim-Zadeh**

Thesis submitted in partial fulfillment of the requirements for the degree of Doctor of Philosophy of the Universitat Politècnica de Catalunya

March 2009

dedicated to my loving parents

I slept and dreamt that life was joy. I awoke and saw that life was service. I acted and behold, service was joy.

– Ravindranath Tagore
(Nobel laureate)

Declaration

I hereby declare that the matter embodied in the thesis entitled **"High-power, continuous-wave optical parametric oscillators from visible to near-infrared"** is the result of investigations carried out by me at the ICFO-Institute of Photonic Sciences, Castelldefels, Barcelona, Spain under the supervision of Prof. Majid Ebrahim-Zadeh, and that it has not been submitted elsewhere for the award of any degree or diploma.

In keeping with the general practice in reporting scientific observations, due acknowledgment has been made whenever the work described is based on the findings of other investigators.

Goutam K. Samanta

Certificate

I hereby certify that the matter embodied in this thesis entitled **"High-power, continuous-wave optical parametric oscillators from visible to near-infrared"** has been carried out by Mr. Goutam K. Samanta at the ICFO-Institute of Photonic Sciences, Castelldefels, Barcelona, Spain, under my supervision, and that it has not been submitted elsewhere for the award of any degree or diploma.

Prof. Majid Ebrahim-Zadeh
(ICFO, Research Supervisor)

Acknowledgments

There has been so much help from everyone I have got to know and have met during the course of my PhD that I would like to thank deeply. Although I am trying to name all the people that I can think of at the time of writing, there will be many others who I may fail to mention.

In the first place, I would like to record my gratitude to Prof. Majid Ebrahim-Zadeh for his supervision, advice, and guidance from the very early stage of this research, as well as giving me extraordinary experiences throughout the work. Above all and the most needed, he provided me enormous encouragement and support in various ways. His truly scientific intuition has made him a constant oasis of ideas and passions in science and technology, which exceptionally inspire and enrich my growth as a student, a researcher and a scientist that I want to be. His ever friendly attitude made me free to express, explore and implement new ideas. I am indebted to him more than he knows.

Special thanks to my labmates Adolfo, Chaitanya, Omid and Ritwick for creating such a great friendship in the lab, and for sharing instruments, various scientific thoughts, and also sharing a lot of funny and light moments during lunch and coffee breaks. I would also like to acknowledge Adolfo for translating my thesis abstract into Spanish. It is my pleasure to thank Dr. Mike Yarrow from Radiantis for his technical advice. I would also like to thank all my friends: Debasis, Prasun, Rajan, Pavan, Anisha, Manoj, Osamu, Dhriti, Mousumi, Susanta, Ardhendu, Dhriti, Sudhir and many others for their friendly supports and for sharing their views (scientific and non-scientific).

I want to express my gratitude to Prof. Lluis Torner, Director of the ICFO-

Institute of Photonic Sciences and his management team, for financial support during my research work and for making the ICFO such a wonderful place for research.

I convey special acknowledgment to the purchasing unit for their indispensable help dealing with travel funds and purchasing instruments, and human resources unit for taking all the responsibilities of administration and bureaucratic matters during my stay in ICFO and helping me to concentrate only on my research. This work would not be possible without the timely support from the mechanical workshop of ICFO. Therefore, I would like to thank all the previous and present members of the mechanical workshop.

Many thanks go in particular to Dr. Ujjwal Sen and Dr. Aditi Sen (De). I am much indebted to both of them not only for their valuable advice in scientific discussions, but also for their immense support to make my stay in Barcelona pleasant. I would also tribute special thanks to Aditi-didi, who did not let me feel the scarcity of Indian curry in Barcelona with her expert cooking capabilities.

To my childhood icon, Prof. Nikhil K. Singha, Indian Institute of Technology-Kharagpur, India, I would like to thank him for being the first person who grew my interest in science. I am proud to record his suggestions and immense support since my school life.

I am grateful to all my teachers and professors in the schools and Universities for sharing their immense knowledge in wide range of fields and preparing me for the advanced studies with a clear picture of the basic sciences.

Where would I be without my family? My parents deserve special mention for their inseparable love, support and encouragements, even from a very far distance. My father, Ajit Ranjan Samanta and mother, Kalpana Samanta, in the first place are the persons who put the fundament in my learning character, showing me the joy of intellectual pursuit ever since I was a child. Manasi, Tulasi, and Atasi, thanks

for being supportive and caring siblings. I am so grateful for every single thing that they have done for me. They are always the motivation for everything I have done in my life.

Words fail me to express my appreciation to my wife Moumita, whose dedication, love and persistent confidence in me since our bachelor of technology study, has taken the load off my shoulder. I owe her for being supportive for scientific and technological discussions, passions, ambitions and also in the family matters despite her burdened research schedule in Indian Space Research Organization. My life is so much happier and more fulfilled with her presence in my heart. Therefore, I would also thank Mr. Jagannath Dutta's family for letting me take her hand in marriage, and accepting me as a member of their family, warmly. Furthermore, special thanks to my mother-in-law, Sukla Dutta, who has always encouraged me towards my research work and always lent her helping hand in all my difficulties. Special thanks to my uncle Satish Das and my beloved sister-in-law Nabanita.

Finally, I would like to thank everybody who was important to the successful realization of thesis, as well as expressing my apology to those whom I could not mention personally one by one.

Abstract

This thesis presents the development of a new class of high-power, continuous-wave (cw) optical parametric oscillators (OPOs) with extended tunability from the visible to the near-infrared (near-IR). While lasers have been in use for nearly 50 years, it is still difficult to develop laser systems that can cover many regions of the optical spectrum, from the ultraviolet (UV) and visible to the near- and mid-infrared wavelength range, with potential applications in the fields such as spectroscopy, remote sensing, trace-gas detection, and many more.

Development of cw OPOs in singly-resonant oscillator (SRO) configurations, the focus of this thesis, is challenging due to the high-threshold pump power (several watts). In addition, with visible pumping, photorefractive and thermal lensing effects become important issues to overcome. Therefore, the realization of practical cw SROs requires optimal cavity design, suitable nonlinear materials, and high-power lasers with high spectral and spatial quality.

High-power, single-frequency, cw SROs based on 30-mm-long MgO-doped, stoichiometrically grown, periodically-poled $LiTaO_3$ (MgO:sPPLT) have been developed. The oscillators were pumped in the green by a frequency-doubled, cw diode-pumped Nd:YVO_4 laser at 532 nm. With a single grating period of 7.97 μm, continuous signal and idler covering the 848$-$1430 nm region is obtained by temperature tuning between 52 °C and 248 °C. In a linear cavity configuration and with double-pass pumping, an oscillation threshold of 2.88 W has been obtained; and single-pass idler powers in excess of 1.51 W have been generated over the 1104$-$1430 nm region for 6 W of pump power at an extraction efficiency of 25.2% and a photon conversion efficiency of 56.7%.

For single-frequency performance of the cw SRO across the 848−1430 nm range, we have used a compact ring cavity configuration along with a frequency selecting element (etalon). Using the same MgO:sPPLT crystal, the SRO oscillation threshold of 2.84 W has been obtained, and single-pass idler powers in excess of 1.59 W have been generated over the 1104−1430 nm range with a maximum SRO extraction efficiency of 25.2% and pump depletions as high as 67%. The single-frequency idler output has a linewidth of ∼7 MHz. Under free-running conditions and in the absence of thermal isolation, the idler power exhibits a peak-to-peak stability of 16% a over 5 hours duration.

Although the cw SRO can provide optical radiation across the 848−1430 nm range, the high output power was only available over the range of 1104−1430 nm, due to the high reflectivity of the cavity mirrors employed for SRO operation. Using finite output coupling of the resonant wave, we have extended the available practical output power across the entire tuning range. The cw out-coupled SRO (OC-SRO) can deliver a total power of up to 3.6 W at 40% extraction efficiency with a linewidth of 3 MHz across the 848−1430 nm range. The signal power shows a peak-to-peak power stability of <10.7% over a 40 minutes period in a TEM_{00} spatial mode with M^2 <1.52. Without any active stabilization, the resonant signal exhibits a natural long-term frequency stability of <75 MHz over 15 minutes and short-term frequency stability of <10 MHz over 10 seconds periods, demonstrating the potential of the system for spectroscopic applications.

Using internal second-harmonic-generation of the resonant, near-infrared signal radiation of the MgO:sPPLT cw SRO in a 5-mm-long BiB_3O_6 crystal, we have generated 1.27 W of cw, single-frequency blue power over a tunable range of 425−489 nm with a linewidth of 8.5 MHz in a Gaussian spatial beam profile. The blue source is frequency-stable to better than 280 MHz, limited by the resolution of the

wavemeter.

We have also developed cw green light sources, in a simple, single-pass experimental configuration by frequency-doubling the radiation from a fiber laser using MgO:sPPLT and periodically-poled $KTiOPO_4$ (PPKTP) crystals, generating as much as 9.6 W of green radiation in TEM_{00} spatial beam profile (M^2 <1.33) with a single-pass efficiency of 32.7% in MgO:sPPLT. This green light source has also successfully been used to pump cw SROs and will in the future be used to pump Ti:sapphire lasers.

Using this frequency-doubled green light source, we have demonstrated cw OC-SRO providing a stable single-frequency output power up to 2 W across the tuning range of 855−1408 nm, with peak-to-peak power stability of <11.7%, frequency-stability of <10 MHz over 10 seconds, in TEM_{00} (M^2 <1.26) spatial beam profile.

Abstract

Códigos UNESCO: 220913, 220910, 220909, 220923

Esta tesis presenta el desarrollo de una nueva clase de osciladores ópticos paramétricos (OPOs) de onda continua (cw) y alta potencia con extendida sintonización desde el visible al infrarrojo (IR) cercano. A pesar de que los láseres están en uso desde hace casi 50 años, todavía es difícil desarrollar sistemas láser que puedan cubrir muchas regiones del espectro óptico en los rangos de longitud de onda desde el ultravioleta (UV) y visible hasta el infrarrojo cercano y medio, con potenciales aplicaciones en campos como la espectroscopia, sensores remotos, detección de trazas de gases, entre muchas otras.

El desarrollo de cw OPOs en configuraciones de oscilador simplemente resonante (SRO), objetivo principal de esta tesis, es un gran desafío debido al alto umbral de potencia de bombeo (varios watts). Además, cuando se emplea bombeo visible, los efectos fotorrefractivo y de lente térmica adquieren especial relevancia y son difíciles de superar. Por lo tanto, la realización de cw SROs prácticos requiere de un óptimo diseño de cavidad, adecuados materiales no lineales y láseres de alta potencia con excelente calidad tanto espectral como espacial.

Se han desarrollado cw SROs de alta potencia y frecuencia única basados en cristales de $LiTaO_3$ de 30-mm de longitud, de crecido estequiométrico, con dopado de MgO y periódicamente pulidos (MgO:sPPLT). Los osciladores fueron bombeados en el verde mediante el láser de cw Nd:YVO_4 bombeado por diodos y doblado en frecuencia. Utilizando un único periodo de red de 7.97 μm, se ha obtenido cobertura

continua de los campos señal y pivote en el rango 848−1430 nm por sintonización de temperatura entre 52 °C y 248 °C. Empleando una configuración de cavidad lineal y bombeo de doble paso, se ha logrado un umbral de oscilación de 2.88 W y se han generado potencias superiores a 1.51 W para el campo pivote en simple paso dentro del rango 1104−1430 nm para 6 W de potencia de bombeo, eficiencia de extracción del 25.2% y eficiencia de conversión de fotón del 56.7%.

Con el objetivo de operar el cw SRO en frecuencia única a través del rango 848−1430 nm, hemos utilizado una configuración compacta de cavidad en anillo junto a un elemento para la selección de frecuencia (etalon). Utilizando el mismo cristal de MgO:sPPLT, se ha obtenido un umbral de oscilación del SRO de 2.84 W y se han generado potencias superiores a 1.59 W para el campo pivote en paso único dentro del rango 1104−1430 nm con una eficiencia máxima de extracción del 25.2% y agotamiento del bombeo tan alto como el 67%. La salida del campo pivote en frecuencia única tiene un ancho de línea de ∼7 MHz. Bajo condiciones de sistema libre y en ausencia de aislamiento térmico, la potencia del campo pivote exhibe estabilidad de pico a pico de 16% durante 5 horas. A pesar de que el cw SRO puede proveer radiación óptica en el rango 848−1430 nm, la alta potencia de salida solo se consiguió obtener en el rango 1104−1430 nm a causa de la alta reflectividad de los espejos de la cavidad para operar en SRO. Utilizando un acoplamiento de salida finito de la onda resonante, hemos extendido la disponibilidad de prácticas potencias de salida a través de todo el rango de sintonía. El cw SRO con acoplador de salida (OC-SRO) puede entregar un apotencia total de hasta 3.6 W con una eficiencia de extracción del 40% y con un ancho de línea de 3 MHz en el rango 848−1430 nm. La potencia del campo señal muestra fluctuaciones en potencia de pico a pico <10.7% durante 40 minutos y modo espacial TEM_{00} con M^2 <1.52. En ausencia de estabilización activa, el campo señal resonante exhibe una estabilidad en frecuencia

natural a largo término con fluctuaciones <75 MHz durante 15 minutos, así como a corto término con fluctuaciones <10 MHz durante 10 segundos, demostrando el potencial del sistema para aplicaciones en espectroscopia.

Utilizando generación interna de segundo harmónico del campo señal resonante en el rango del infrarrojo cercano del MgO:sPPLT cw SRO mediante un cristal de BiB_3O_6 de 5-mm de longitud, hemos logrado generar 1.27 W de potencia cw y frecuencia única en el azul dentro del rango de sintona 425−489 nm y con un ancho de línea de 8.5 MHz y un perfil espacial del haz de tipo Gaussiano. La estabilidad en frecuencia de la fuente azul es mejor que 280 MHz, donde la limitación viene impuesta por la resolución del medidor de longitud de onda empleado.

Adicionalmente, hemos desarrollado fuentes verdes en cw en una sencilla configuración experimental de único paso, mediante el doblado en frecuencia de un láser de fibra con cristales de MgO:sPPLT y $KTiOPO_4$ pulido periódicamente (PPKTP), generando hasta 9.6 W de radiación verde en modo espacial TEM_{00} (M^2 <1.33) con una eficiencia de paso único de 32.7% en MgO:sPPLT. Esta fuente verde has sido también empleada exitosamente para bombear cw SROs y será utilizada para bombear láseres de Ti:sapphire.

Mediante esta fuente verde doblada en frecuencia, hemos demostrado que el cw OC-SRO proporciona una salida estable en frecuencia única con potencia de hasta 2 W a través del rango de sintonía 855−1408 nm, con estabilidad en potencia de pico a pico <11.7%, estabilidad en frecuencia <10 MHZ durante 10 segundos y modo espacial TEM_{00} (M_2 <1.26).

Publications

Journal publications:

1. *High-power, continuous-wave, singly resonant optical parametric oscillator based on MgO:sPPLT*

   G. K. Samanta, G. R. Fayaz, Z. Sun, and M. Ebrahim-Zadeh

   Optics Letters **32**, 400-402 (2007).

2. *1.59 W, single-frequency, continuous-wave optical parametric oscillator based on MgO:sPPLT*

   G. K. Samanta, G. R. Fayaz, and M. Ebrahim-Zadeh

   Optics Letters **32**, 2623-2625 (2007).

3. *Continuous-wave singly-resonant optical parametric oscillator with resonant wave coupling*

   G. K. Samanta and M. Ebrahim-Zadeh

   Optics Express **16**, 6883–6888 (2008).

4. *Continuous-wave, single-frequency, solid-state blue source for the 425489 nm spectral range*

   G. K. Samanta and M. Ebrahim-Zadeh

   Optics Letters **33**, 1228–1230 (2008).

5. *High-power, continuous-wave, second-harmonic generation at 532 nm in periodically poled $KTiOPO_4$*

   G. K. Samanta, S. Chaitanya Kumar, C. Canalias, V. Pasiskevicius, F. Laurell, and M. Ebrahim-Zadeh

   Optics Letters **33**, 2955–2957 (2008).

6. *9.6 W, stable, continuous-wave, single-frequency, fiber-based green source at 532 nm*

   G. K. Samanta, S. Chaitanya Kumar, and M. Ebrahim-Zadeh

   Optics Letters **34**, 1561–1563 (2009).

7. *Continuous-wave, stable, singly-resonant oscillator pumped by fiber-based green source at 532 nm*

   G. K. Samanta, S. Chaitanya Kumar, Ritwick Das, and M. Ebrahim-Zadeh

   Optics Letters (Communicated) 2009.

8. *High power, single frequency, continuous wave, second-harmonic-generation of ytterbium fiber laser using PPKTP and MgO:sPPLT*

   S. Chaitanya Kumar, **G. K. Samanta**, and M. Ebrahim-Zadeh

   Optics Express (Communicated) 2009.

Conference publications:

1. *Efficient generation of tunable cw single frequency green radiation by second harmonic generation in periodically-poled $KTiOPO_4$*

   Z. Sun, **G. K. Samanta**, G. R. Fayaz, M. Ebrahim-Zadeh, C. Canalias, V. Pasiskevicius, and F. Laurell

   Conf. Lasers Electro-Opt (CLEO), Baltimore, USA Paper CTuK1 , May 2007.

2. *1.5 W, Green-Pumped, Continuous-Wave, Singly-Resonant Optical Parametric Oscillator Based on MgO:sPPLT*

G. K. Samanta, G. R. Fayaz, Z. Sun, and M. Ebrahim-Zadeh

Conf. Lasers Electro-Opt (CLEO), Baltimore, USA Paper CTuK4, May 2007.

3. *High-power, single-frequency, continuous-wave optical parametric oscillator based on MgO:sPPLT*

   G. K. Samanta, G. R. Fayaz, Z. Sun, and M. Ebrahim-Zadeh

   CLEO-Europe/EQEC, Munich, Germany Paper CD3-5-MON, June 2007.

4. *Performance enhancement of continuous-wave, singly resonant optical parametric oscillator using signal coupling*

   G. K. Samanta and M. Ebrahim-Zadeh

   Conf. Lasers Electro-Opt (CLEO), San Jos, USA Paper CTuY2, May 2008.

5. *Tunable, continuous-wave, single-frequency, solid-state source for the blue*

   G. K. Samanta and M. Ebrahim-Zadeh

   3rd EPS-QEOD Europhoton Conference, Paris, France 31th August -5th September (2008).

6. *Tunable, continuous-wave, solid-state source for the blue*

   G. K. Samanta and M. Ebrahim-Zadeh

   IEEE Photonics Global @ Singapore, Singapore Paper D1-1-03, December (2008).

7. *Tunable, high-power, solid-state sources for the blue and ultraviolet*

   G. K. Samanta, A. Esteban-Martina, M. Ghotbi, and M. Ebrahim-Zadeh (**Invited**)

   Proc. SPIE, Vol. **7197**, 719702 (2009).

Contents

Chapter 1

Introduction

The laser is one of the inventions that brought science very much ahead in the last few decades due to its wide variety of applications including laser spectroscopy, photochemistry, reaction dynamics, material processing, information technology, and medical diagnostics. The development of semiconductor diode lasers made laser science and technology an important part and parcel in our daily life, from bar-code readers in supermarkets to music players, and also moved the laser technology forward to develop the efficient diode-pumped, solid-state lasers. Although lasers have been in use for nearly 50 years, many regions of the optical spectrum, especially in the ultraviolet (UV), visible, and near- to mid-IR, remain inaccessible to lasers due to the unavailability of the suitable gain materials. Figure 1.1 shows the wavelength coverage of some tunable lasers, out of which Ti:sapphire laser is the most prominent laser commercially available with a tuning range of nearly 650−1100 nm, and widely used in scientific and technological applications. The wavelength regions from 475 to 630 nm must be reached by dye lasers, but it is difficult to operate in narrow-linewidth, single-frequency operation. There are some other solid-state and gas lasers such as Nd-lasers, fiber lasers, He-Ne, and CO_2 laser for discrete wavelengths or narrow tunable wavelength regions.

Optical parametric oscillators (OPOs) have the ability to cover many regions in the optical spectrum inaccessible by conventional lasers (Fig. 1.1), offerimg a solid-state design with practical output powers at high efficiencies, and in all time scales from the cw and long-pulse microsecond regime to nanosecond, picosecond, and even ultrafast sub-20 fs time-scales.

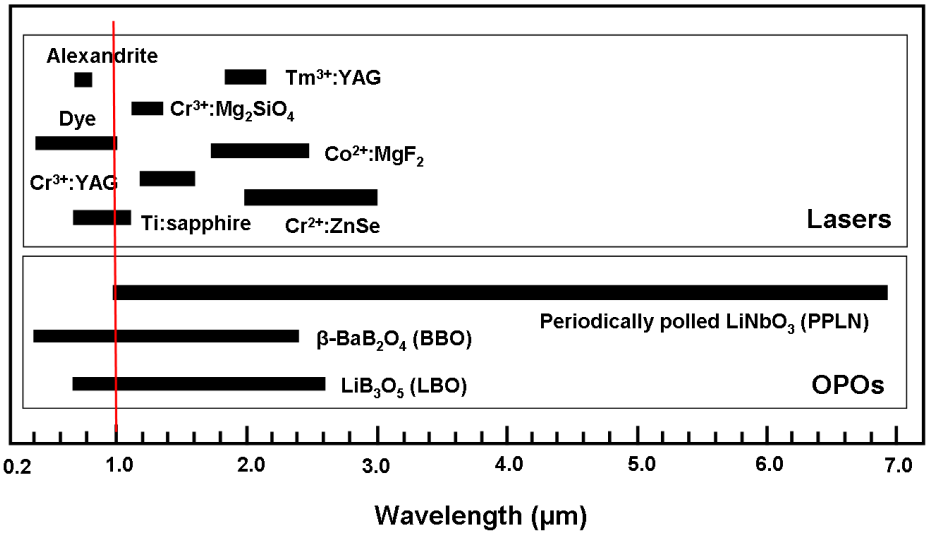

Figure 1.1: Comparison of the tunable radiations available from lasers and optical parametric oscillators [1].

The OPO is a device that converts a fixed pump-laser wavelength to two lower-energy, longer wavelength photons known as the *signal* and the *idler*. The operation of an OPO is critically dependent on the spectral and spatial quality of the pump laser and also on the properties of the nonlinear optical materials. Therefore, due to the unavailability of suitable laser sources and proper nonlinear optical materials, development of the practical OPOs was held back for many years after the demonstration of the first prototype device by Giordmaine and Miller in 1965 [2]. As a result, OPOs were not considered useful coherent light sources for many applications for more than 20 years. The development of new nonlinear optical materials and new laser sources with improved spectral and spatial coherence in the 1980s

again prompted a major insurgence of interest in the development of pulsed OPOs. Today, there are established technologies for pulsed OPOs in the spectral regions from mid-IR [3] to visible [4], and down to ultraviolet (UV) [5] using, for instance; β-BaB_2O_4 (BBO), LiB_3O_5 (LBO) and BiB_3O_6 (BIBO) as the nonlinear crystals.

The high-power, spectrally pure, all-solid-state sources especially in the continuous-wave (cw) time scale with tunability from the UV up to the mid-IR are of great importance for numerous applications. Although, for many years, the dye laser and the Ti:sapphire laser were the most widely established technologies for this purpose, popular in this regards in spite of their complexity and high cost, cw OPOs can potentially provide such radiation in a much simpler and cost-effective design. However, cw OPOs have traditionally been the most challenging class of devices due to substantially lower nonlinear gains available under cw pumping. Therefore, they require high-power pump lasers (typically several watts), optical materials with high nonlinearity, or the deployment of multiply resonant cavities in order to reduce the threshold pump power and achieve successful operation. Like lasers, the optical feedback is also provided in OPOs, deploying an optical cavity with correct choice of the mirrors. Depending on the number of waves resonating in the optical cavity, the OPOs are termed as singly resonant oscillator (SRO), doubly resonant oscillator (DRO), triply resonant oscillator (TRO) and pump-resonant or pump-enhanced (PE-) SRO. The various OPO configurations are further explained in details in Chapter 2.

Despite the highest operation threshold power over other OPO configurations, cw SROs offer the most viable solution for parametric generation of high-power, cw, single-frequency radiation over extended spectral regions. The first cw SRO was developed by Yang et al. [6] in 1993 using birefringent KTP crystal. Since then, the development of new quasi-phase-matched (QPM) materials and improved

laser sources in the mid-1990s opened up new advancements in the field of cw SROs [7–10].

The vast majority of cw SROs developed to date have been based on periodically-poled lithium niobate, well-known as PPLN, providing spectral coverage from ∼1 μm to the absorption edge of the material near ∼5 μm [7–10]. Photorefractive damage induced by the visible pump or signal radiation precludes the use of PPLN for wavelengths below ∼1 μm (as marked by the red line in Fig. 1.1). Therefore, the development of cw OPOs for the UV to the near-infrared (near-IR) regions, especially in high-power SRO configurations, necessitates the search for new QPM materials. Periodically-poled lithium tantalate (PPLT) is one such promising material due to its increased resistance to photorefractive damage even though it has a lower nonlinear coefficient (d_{eff} >10 pm/V) as compared to PPLN (d_{eff} >17 pm/V). Although PPLT has been used to demonstrate pulsed OPO [11] and cw PE-SROs [12], a stable, widely-tunable, single-frequency cw SRO pumped in the visible and emitting near-IR to UV has not yet been demonstrated except for those presented in this thesis and subsequently [13; 14] afterwards.

Our generic approach is shown in the Fig. 1.2. We used a commercial, fixed-frequency, narrow-linewidth solid-state laser in the visible and a compact frequency-doubled fiber laser to pump the cw SRO. The SRO source emits cw radiation tunable in the near-IR. To extend the emission into the visible range, we frequency doubled the signal. By sum frequency mixing between the generated signal and the pump, one could generate (this is our future project) UV radiation down to 325 nm. On the other hand, one could also in principle generate radiation in the entire visible range and down to UV by changing the grating period of the PPLT crystal.

In this thesis, we present a cw SRO pumped in the visible. The SRO provides output radiation in near-IR with a wide tunability across 848−1430 nm wavelength

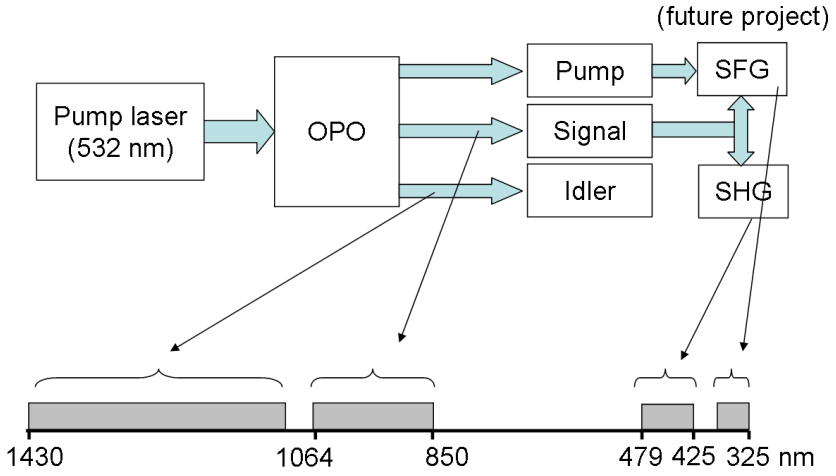

Figure 1.2: Concept of the development of tunable light sources.

range and in the blue across 425−489 nm, which to our knowledge, is the first cw SRO based on PPLT crystal with largest emission range in the blue as compared to other existing and reported cw blue sources. The output exhibits high-power in good spatial beam quality and excellent spectral properties: narrow-linewidth and high frequency-stability. In addition, we have developed a compact, high-power green source with stable, single-frequency operation and a good spatial beam profile by single-pass frequency doubling of a high-power fiber laser. This green source has also been used successfully in order to realize cw SRO operation. Since the performance of the near-IR cw SRO, blue cw SRO and the cw green source have excelled by the above description, they all have been treated in separate Chapters.

This thesis is organized into 9 Chapters. Chapter 2 provides an introduction to nonlinear optics and optical parametric oscillation. As the successful operation of a cw SRO device necessitates proper design criteria, we have discussed some of the important designed issues in Chapter 3. Using the necessary design criteria, we have developed cw SROs using PPLT crystal in linear cavity and its stable,

single-frequency operation in a ring cavity configuration, as described in Chapter 4. Although the cw SRO can provide optical radiation across 848−1430 nm, the high output power was only available across 1104−1430 nm due to the high reflectivity of the cavity mirrors at resonant wavelength range in order to sustain SRO operation. Using a finite output coupling of the resonant wave, we have extended the available practical output power across the entire tuning range as presented in Chapter 5. To extend cw SRO operation into the visible, we have used internal second-harmonic-generation of the resonant near-infrared signal radiation of the cw SRO to generated widely tunable blue radiation, as depicted in Chapter 6. There is only one commercially available, high-power green laser (Coherent Verdi), used to pump visible and near-IR cw SROs. In Chapter 7, we therefore present the operation of alternative high-power green lasers using single-pass frequency-doubling of a fiber laser in two different periodically-poled crystals and compare their performances at high pump powers. Using such a high power, home-made green source, we demonstrated cw SRO operation in the near-IR, as presented in Chapter 8. And, finally, we conclude our work with future outlook in Chapter 9.

Chapter 2

Basics of nonlinear optics

2.1 The origin of optical nonlinearity

Optics is the study of the interaction of electromagnetic radiation and matter. When an electromagnetic wave interacts with a dielectric material, it induces a polarization; the dipole moment per unit volume. The dipole moment primarily arises due to the displacement of the valence electrons from their stationary orbits. The direction and magnitude of the polarization are dependent on the magnitude, the direction of propagation, and the polarization direction of the applied electric field inside the medium. The induced polarization, $\mathbf{P}$, can be expressed as a power series of the applied electric field in the form

$$\begin{aligned} \mathbf{P} &= \epsilon_0(\chi^{(1)}\mathbf{E} + \chi^{(2)}\mathbf{E}^2 + \chi^{(3)}\mathbf{E}^3 + ...) \\ &= \mathbf{P}^L + \mathbf{P}^{NL} \end{aligned} \tag{2.1}$$

where ϵ_0 is the permitivity of the vacuum, $\mathbf{E}$ is the electric field component of the electromagnetic wave, and $\chi^{(m)}$ is the susceptibility tensor of mth order with the

rank (m+1). The linear polarization is defined as:

$$\mathbf{P}^{L} = \epsilon_0 \chi^{(1)} \mathbf{E} \tag{2.2}$$

and the nonlinear polarization is represented as:

$$\mathbf{P}^{NL} = \epsilon_0 (\chi^{(2)} \mathbf{E}^2 + \chi^{(3)} \mathbf{E}^3 + ...) \tag{2.3}$$

In daily life, the strength of the electric field is relatively small, and hence the induced polarization is proportional to the electric field, and the material response can be solely described by Equation (2.2), resulting reflection, refraction, dispersion, and diffraction. However, if the light is intense enough, the relative displacement of the electron cloud from its nucleus is nonlinear with the electric field, and the higher-order terms of Equation (2.3) have to be taken into account, generating new frequencies. Typically, only laser light is sufficiently intense to produce new frequencies. Therefore, the beginning of the field of nonlinear optics is considered as the demonstration of second-harmonic-generation (SHG) in quartz [15], after the invention of the first working laser [16] in 1960. As nonlinear optics is a very vast field, therefore, the brief discussion on the nonlinear processes given here will be limited to the interactions that involve the second-order nonlinear susceptibility, $\chi^{(2)}$. Other interactions can be found in a multitude of references [17–19].

2.2 Second-order nonlinear processes

The second-order nonlinear polarization can be represented as follows:

$$\mathbf{P}^{NL} = \epsilon_0 \chi^{(2)} \mathbf{E}\mathbf{E} \tag{2.4}$$

where $\chi^{(2)}$ is the second-order nonlinear susceptibility tensor, which exists only in a medium without center of inversion in the point symmetry group, i.e, in non-centrosymmetric materials. We will use d-tensor notation rather than $\chi^{(2)}$ in the remaining of this dissertation, as it is more common in the experimental literature. It is defined as [18; 19]:

$$d_{ijk} = \frac{\chi^{(2)}_{ijk}}{2} \tag{2.5}$$

Using Kleinman symmetry [19], i.e. all interacting frequencies are far from resonances, the tensor can be contracted into a 3×6-element matrix, so that

$$\begin{pmatrix} P_x \\ P_y \\ P_z \end{pmatrix} = 2\epsilon_0 K \begin{bmatrix} d_{11} & d_{12} & d_{13} & d_{14} & d_{15} & d_{16} \\ d_{21} & d_{22} & d_{23} & d_{24} & d_{25} & d_{26} \\ d_{31} & d_{32} & d_{33} & d_{34} & d_{35} & d_{36} \end{bmatrix} \begin{pmatrix} E_x^2 \\ E_y^2 \\ E_z^2 \\ E_y E_z + E_z E_y \\ E_x E_z + E_z E_x \\ E_x E_y + E_y E_x \end{pmatrix} \tag{2.6}$$

where K is the degeneracy factor, which takes the value of 1/2 for SHG and optical rectification, and 1 for the other conversion processes. If we assume an applied electric field consisting of two distinct frequency components, ω_1 and ω_2, as presented in the form:

$$\mathbf{E}(t) = \mathbf{E}_1 e^{-i\omega_1 t} + \mathbf{E}_2 e^{-i\omega_2 t} + c.c. \tag{2.7}$$

then, using Equations (2.4) and (2.7), the second-order nonlinear polarization, $\mathbf{P}^{NL}$, can be represented as a function time as follows:

$$\mathbf{P}^{NL}(t) = \sum_{n=1,2} P(\omega_n) e^{-i\omega_n t} = \chi^{(2)}[\mathbf{E}_1^2 e^{-2i\omega_1 t} + \mathbf{E}_2^2 e^{-2i\omega_2 t} + 2\mathbf{E}_1\mathbf{E}_2 e^{-i(\omega_1+\omega_2)t} + 2\mathbf{E}_1\mathbf{E}_2^* e^{-i(\omega_1-\omega_2)t} + c.c.] + 2\chi^{(2)}[\mathbf{E}_1\mathbf{E}_1^* + \mathbf{E}_2\mathbf{E}_2^*] \tag{2.8}$$

The first two terms on the right hand side of Equation (2.8) represent the physical process described as second-harmonic-generation (SHG), third and fourth terms represent the physical processes called sum-frequency-generation (SFG) and difference-frequency-generation (DFG) respectively, and the last term is known as optical rectification (OR). We do not consider the complex conjugates (c.c.) of the above Equation (2.8), as they do not lead to any extra processes other than the above mentioned processes.

Figure 2.1 illustrates the physical meaning of the different types of frequency conversion processes. In all of the optical processes, the energies of the photons taking part in the frequency mixing have to be conserved. In the SFG and DFG processes, two input photons (ω_1 and ω_2)traveling through the nonlinear medium, as shown in Fig. 2.1 (a), their respective energies are added or subtracted adiabatically resulting in one photon of higher energy (lower wavelength) or lower energy (higher wavelength): $\omega_3 = \omega_1 \pm \omega_2$. In case of SHG, two photons of same the frequency ($\omega_1 = \omega_2 = \omega$) are added adiabatically to generate a new photon of energy twice that of the incident photon energy: $\omega_3 = 2\omega$. In the case of $\omega_1 = \omega_2 = \omega$, and $\omega_3 = 0$, a constant electric polarization of the medium is produced and the effect is known as optical rectification. Another special case that has found important applications is when $\omega_1 = 0$ and $\omega_3 = \omega_2 = \omega$. Then, one of the input fields is static, and the refractive index of the medium is affected through the linear electro-optic effect. This is also known as the Pockels effect.

Figure 2.1 (b) shows another type of process, down-conversion or optical parametric generation (OPG), which starts with one input photon (ω_3) and results in two photons of lower energies (ω_1 and ω_2). The two generated wavelengths are referred to as the *signal* and the *idler*, of which the signal is, generally, the one with the shorter wavelength.

When an optical cavity is used to enhance the efficiency by resonating one or both of the generated fields (Fig. 2.1 (c)), the resulting device is called an *optical parametric oscillator* (OPO). The OPO is the main topic of the work described in this thesis and will be treated more thoroughly in Section 2.5.

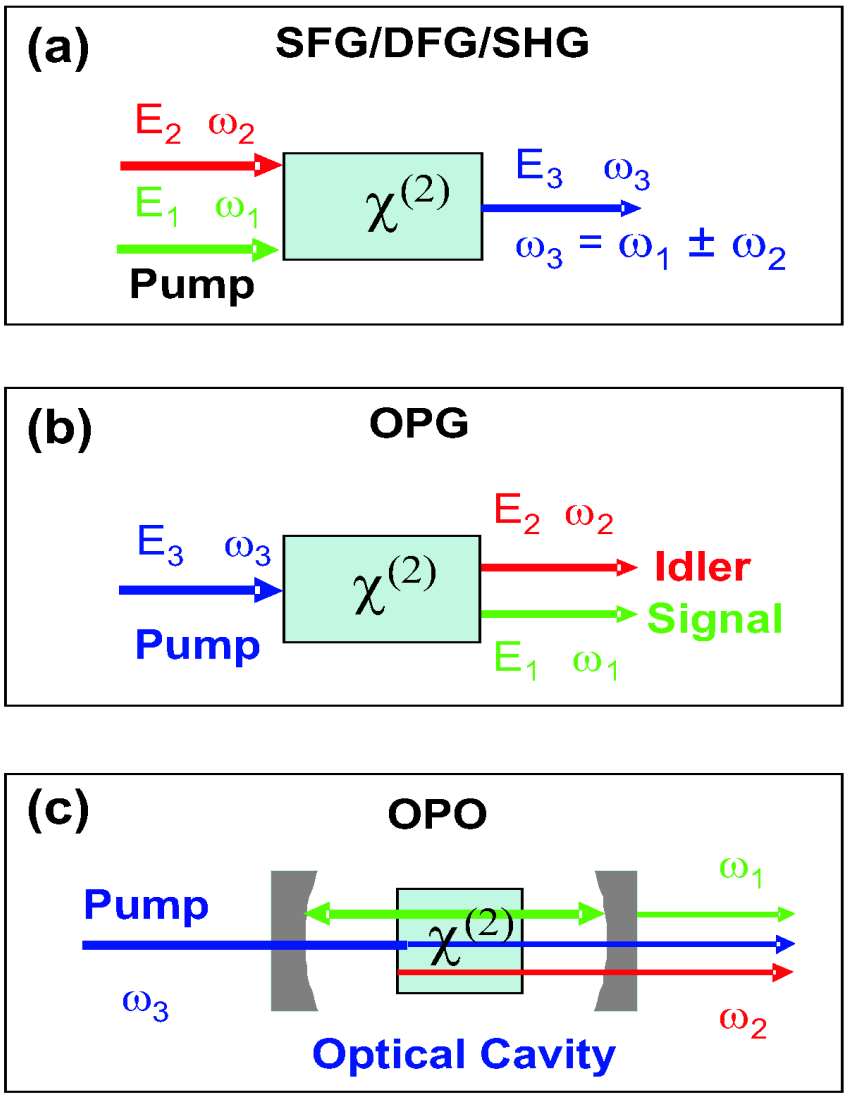

Figure 2.1: Schematic diagram of the second-order nonlinear processes.

2.3 Coupled-wave equations for the second-order nonlinear processes

The above discussion has shown how the electromagnetic waves of given frequencies can induce a response at other frequencies in a nonlinear medium. To understand further the generation of the new frequencies and the energy transfer among the interactive waves, we have to solve the Maxwell's electromagnetic equations in the medium.

In a nonlinear, nonmagnetic dielectric medium with no currents, no free charges, and the Maxwells equations can be reduced to the wave equation with a nonlinear driving term [19]:

$$\nabla^2\mathbf{E} = \mu_0\epsilon_0\frac{\partial^2\mathbf{E}}{\partial t^2} + \mu_0\frac{\partial^2\mathbf{P}^{NL}}{\partial t^2} \tag{2.9}$$

where μ_0 is the permeability of the vacuum. This equation can, in general, not be solved analytically, but by using some assumptions, a formulation much more suited for our calculations can be found. The electric filed, $\mathbf{E}$, and polarization, $\mathbf{P}$, propagating along x-axis may be described as follows:

$$\mathbf{E}(x,t) = \frac{1}{2}[\mathbf{E}(x,\omega)e^{-i(kx-\omega t)}] + c.c. \tag{2.10}$$

and

$$\mathbf{P}(x,t) = \frac{1}{2}[\mathbf{P}(x,\omega)e^{-i(kx-\omega t)}] + c.c. \tag{2.11}$$

where ω is the frequency of the waves, and k is the wavenumber given by the expression

$$k = \frac{n(\omega)\omega}{c} \tag{2.12}$$

The refractive index, $n(\omega)$, at frequency ω is represented as:

$$n = n(\omega) = \sqrt{\frac{\epsilon(\omega)}{\epsilon_0}} \tag{2.13}$$

where $\epsilon(\omega)$ is the permittivity of the medium at frequency ω, ϵ_0 is the permittivity of the free space, and c is the speed of light in vacuum.

For interactions (linear and nonlinear), where the amplitudes of the fields change slowly on the scale of the wavelength in space and the optical period in time, one can invoke the Slowly Varying Envelope Approximation (SVEA) [18; 19], which simplifies our wave Equation (2.9) from a second-order to a first-order derivative in the propagation direction as

$$\frac{\partial \mathbf{E}(\omega)}{\partial x} = \frac{i\mu_0 c\sigma}{2n}\mathbf{P}^{NL}(\omega) \tag{2.14}$$

For second-order nonlinear processes, all of the three fields mix with each other, and, using Equations (2.4), (2.10), (2.11) and (2.14) we end up with three coupled wave equations:

$$\frac{\partial E_1}{\partial x} = \frac{i\omega_1^2}{k_1 c^2} K d_{eff} E_3 E_2^* exp(i\triangle kx) \tag{2.15}$$

$$\frac{\partial E_2}{\partial x} = \frac{i\omega_2^2}{k_2 c^2} K d_{eff} E_3 E_1^* exp(i\triangle kx) \tag{2.16}$$

$$\frac{\partial E_3}{\partial x} = \frac{i\omega_3^2}{k_3 c^2} K d_{eff} E_1 E_2 exp(-i\triangle kx) \tag{2.17}$$

where K, (Equation (2.6)), is the degeneracy factor and d_{eff} is the effective nonlinearity, which in addition to the material properties, depends on the propagation direction, the optical frequencies, and the planes of polarization of the interacting waves [18; 19]. The interacting waves obey the frequency relation $\omega_3 = \omega_1 + \omega_2$. The phase-mismatch or the momentum mismatch is given by $\triangle k = k_3 - k_2 - k_1$.

The interaction is efficient when $\triangle k = 0$, which can be achieved by different means as explained in Section 2.4.

For a SHG process, (see Fig. 2.1 (a), $\omega_1 = \omega_2 = \omega$ and $\omega_3 = 2\omega$), there are only two interacting waves, ω and 2ω. The coupled-wave equations for SHG can then be represented as

$$\frac{\partial E_{2\omega}}{\partial x} = iK\frac{2\omega}{n_{2\omega}c}d_{eff}E_{\omega}^{2}exp(i\triangle kx) \tag{2.18}$$

$$\frac{\partial E_{\omega}}{\partial x} = iK\frac{2\omega}{n_{\omega}c}d_{eff}E_{\omega}^{*}E_{2\omega}exp(-i\triangle kx) \tag{2.19}$$

where $\triangle k = k_{2\omega} - 2k_{\omega}$ is the phase mismatch among the interacting waves. k_{ω} and $k_{2\omega}$ are the wave vectors of the interacting waves ω and 2ω respectively. n_{ω} and $n_{2\omega}$ are the refractive indices of the medium at ω and 2ω respectively. At low conversion efficiency, where the intensity of the driving field (pump beam) can be assumed to be constant (i.e. no pump depletion), the above two equations can be reduced to one linear first-order equation that can be solved analytically in plane wave approximation. For this simplified case, the second harmonic intensity is given by [18; 19]:

$$I_{2\omega}(L) = \frac{\epsilon_0 n_{2\omega}c}{2}\left|E_{2\omega}^{2}\right| = \frac{2\omega^2 d_{eff}^2 L^2 I_{\omega}^2}{\epsilon_0 n_{\omega}^2 n_{2\omega}c^3}sinc^2[\frac{\triangle kL}{2}] \tag{2.20}$$

where L is the length of the nonlinear material, I_{ω} is the pump intensity, and n_{ω}, and $n_{2\omega}$ are the refractive indices of the material at the pump and second harmonic wavelengths, respectively.

If pump depletion is taken into account, then the SHG efficiency can be expressed as [20]

$$\eta_{SHG} = tanh^2(\eta_{o,SHG})^{\frac{1}{2}} \tag{2.21}$$

where $\eta_{o,SHG}$ is the SHG efficiency for nondepleted pump approximation and can be

represented from Equation (2.20) as:

$$\eta_{o,SHG} = \frac{I_{2\omega}(L)}{I_\omega} = \frac{2\omega^2 d_{eff}^2 L^2 I_\omega}{\epsilon_0 n_\omega^2 n_{2\omega} c^3} sinc^2[\frac{\triangle kL}{2}] \tag{2.22}$$

2.4 Phase-matching

It can be seen from Equation (2.20) that the SHG intensity, ($I_{2\omega}$, reaches its maximum value when $\triangle k = 0$, that is, when the interacting waves are perfectly phase-matched. As an illustration, Fig. 2.2 shows the dependence of the gain in the SHG process on the total phase mismatch, ($\triangle kL/2$). The $sinc^2$ shape represents how close to perfect phase-matching ($\triangle k = 0$) it is required for efficient SHG to occur.

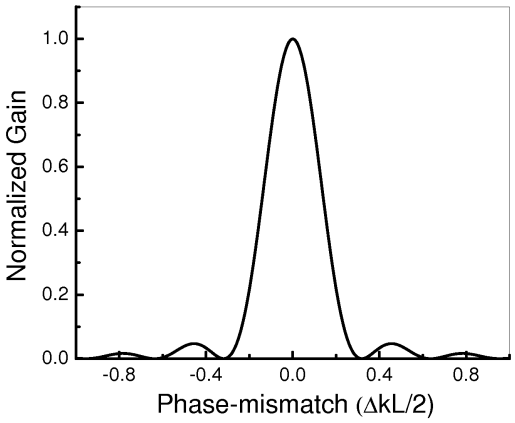

Figure 2.2: Variation of the SHG gain as a function of the total phase mismatch, $\triangle kL/2$. It illustrates the $sinc^2$ dependence of the second-harmonic power as shown in Equation (2.20).

Now, what is the origin of the phase-mismatch effect? As the wave vector, k, is proportional to the refractive index (Equation (2.12)), and the refractive index of a material depends upon the wavelength (anomalous dispersion), therefore, waves of different wavelengths propagate with different phase velocities in the nonlinear medium, leading to a phase-mismatch among the interacting waves. If phase-

matching is not achieved, the SHG efficiency will oscillate along the length of the nonlinear crystal. This results from the oscillation of the relative phase between the driving nonlinear polarization and the generated wave, which will cause the direction of the power flow to change periodically. This oscillatory behavior is illustrated as the phase-mismatched curve in Fig. 2.3. A critical length, the *coherence length* $L_c = \pi/\triangle k$, is the length over which the driving nonlinear polarization and the generated radiation stay in phase and the power flows from the driving nonlinear polarization to the generated waves. During the next coherence length, the driving nonlinear polarization and the generated waves are out of phase with each other and the power flows back from the generated waves to the driving wave.

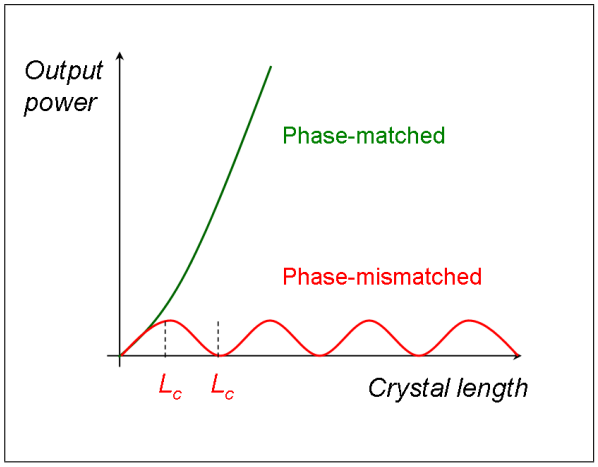

Figure 2.3: Output power as a function of crystal length for: perfectly phase-matched ($\triangle k = 0$), and non-phase-matched ($\triangle k \neq 0$) conditions of the second-order processes, e.g., SHG

If, on the other hand, the driving wave propagates with the same phase velocity as the second harmonic (SH) waves, the newly generated SH radiation will be in phase with the radiation that was generated in an earlier part of the crystal and the amplitudes will add up constructively. As a result, efficient generation of the SH frequency will take place along the whole length of the nonlinear material, as illustrated by the phase-matched curve in Fig. 2.3. Now, the question is how to achieve perfect

phase-matching? There are two important techniques to achieve phase-matching: Birefringent phase-matching (BPM) [21; 22] and quasi-phase-matching (QPM) [17]. This will be the subject of the following two sections.

2.4.1 Birefringent phase-matching (BPM)

Birefringent phase-matching is a most common technique for achieving phase-matching of a nonlinear process by exploiting the birefringence (the refractive index depends on the polarization of the electric field) of an anisotropic, nonlinear crystal. The basic idea of BPM is that the interacting waves of different frequencies are polarized differently, so that their corresponding phase velocities can be adjusted using the proper propagation direction in the crystal while their wave vectors satisfy the phase-matching conditions. Depending upon the number of the axis of anisotropy or the optical axis, the nonlinear crystals can generally be divided into uniaxial (only one optical axis) and biaxial (two optical axes) crystals. All electromagnetic waves, polarized transversally to the optical axis and propagating along the optical axis, will sense the same index of refraction. For simplicity, here we are considering the uniaxial crystal only to understand BPM. In an uniaxial crystal, the birefringence can be formalized by assigning two different refractive indices: the ordinary index of refraction (n_o) and extra-ordinary index of refraction (n_e). The electric field polarized perpendicular to the optical axis will always sense the ordinary index of refraction (n_o), irrespective of the propagation direction and is called the ordinary beam. The beam polarized orthogonally to the ordinary beam, and which lies in the plane spanned by the optical axis, called the extraordinary beam, has a non-zero projection on the optical axis and senses an index of refraction, $n_e(\theta)$, which depends

on the propagation angle according to:

$$\frac{1}{|n_e(\theta)|^2} = \frac{cos^2(\theta)}{n_o^2} + \frac{sin^2(\theta)}{n_e^2} \tag{2.23}$$

where θ is the angle between the optical axis and the propagation direction.

Two refractive index indicatrix for positive and negative uniaxial crystals are shown in Fig. 2.4. Figure 2.4 (a) shows the negative birefringence ($n_o > n_e$) for positive uniaxial crystals and Fig. 2.4 (b) shows positive birefringence ($n_o < n_e$) for negative uniaxial crystals. In a positive (negative) uniaxial crystal, the extraordinary index is increasing (decreasing) with the angle θ from n_o for propagation along the optic axes to n_e for propagation perpendicular to the optical axis.

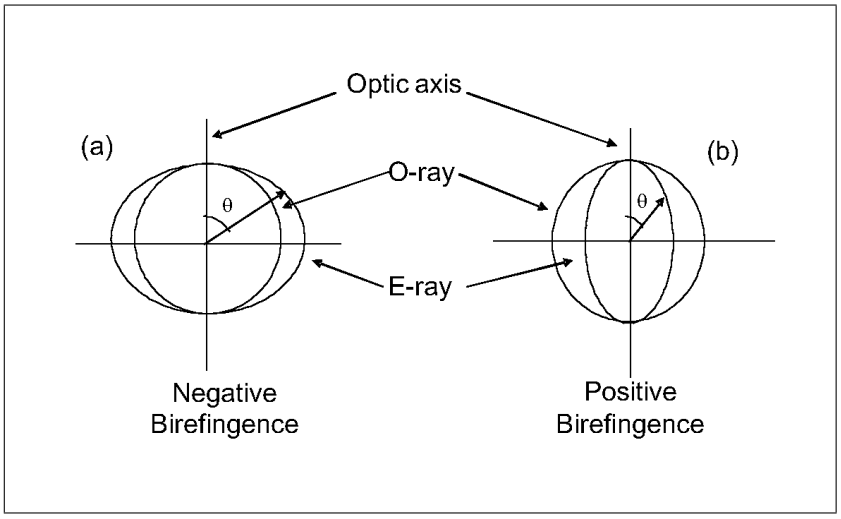

Figure 2.4: Index ellipsoids for (a) positive uniaxial crystals and (b) negative uniaxial crystals.

Figure 2.5 shows a propagation direction at an angle θ of a positive uniaxial crystal, where the extraordinary index for the fundamental wave of frequency ω is equal to the ordinary index for the second-harmonic wave of frequency 2ω, thus compensating for the chromatic dispersion and resulting in perfect phase-matching. Similarly, it is possible to explain phase-matching in negative uniaxial crystals. BPM

are of two types: type-I, where the driving fields have the same polarization and the generated field is polarized orthogonal compared to the driving fields, or type-II, where the driving fields are orthogonally polarized.

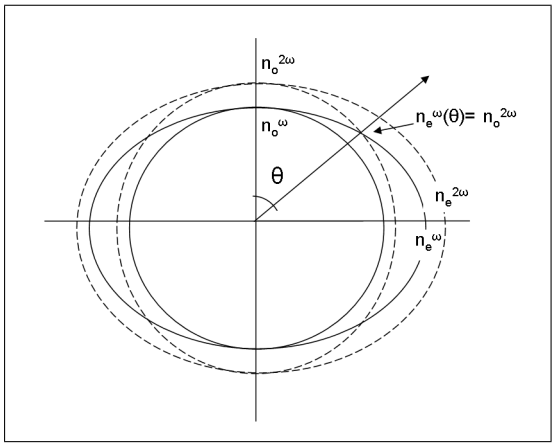

Figure 2.5: The picture shows how ,at an angle of θ, the extraordinary index of refraction for the fundamental wave is equal to the ordinary index of the second-harmonic wave in a positive, uniaxial crystal.

Phase-matching, for the situation where the beam propagation is at an angle $\theta = 90°$ relative to the axis of the dielectric tensor, is referred to as noncritical phase-matching, whereas phase-matching for $\theta \neq 90°$ is called critical phase-matching. The word critical can be attributed to the fact that this technique is relatively sensitive to misalignment of the two beams. There is only a very small finite range of beam angles (known as the angular phase-matching bandwidth), where critical phase-matching works. In the anisotropic medium, when the extraordinary polarized beam is propagating at some angle θ with the optical axes, the refractive index, n_e, and the phase velocity becomes dependent on that angle, leading to spatial walk-off. This phenomenon is also known as birefringent walk-off or Poynting vector walk-off. The spatial walk-off reduces the spatial overlap between the interacting ordinary and extraordinary waves in the nonlinear crystal and, thus, limiting the interaction length of the nonlinear material, and, hence, has a detrimental impact

on the nonlinear conversion efficiency using BPM technique.

The spatial walk-off angle, ρ, can be represented as

$$tan(\rho) = -\frac{1}{n_e(\theta)}\frac{dn_e(\theta)}{d\theta} \tag{2.24}$$

For a uniaxial crystal, the spatial walk-off angle can be expressed as follows:

$$tan(\rho) = -\frac{1}{2}\left|n_e(\theta)\right|^2 (\frac{1}{n_e^2} - \frac{1}{n_o^2})sin(2\theta) \tag{2.25}$$

Spatial walk-off also depends upon the beam radii and becomes more important for smaller beam radii. So, spatial walk-off can be reduced to some extent in order to increase the effective nonlinear interaction length by increasing the beam radii, but unfortunately the nonlinear optical processes necessitate high-power density and, hence, small beam radii. Therefore, a good balance between the crystal length and beam radii must be maintained for efficient nonlinear optical processes. It is, however, possible to achieve a kind of "partial walk-off compensation [23; 24] by using two subsequent nonlinear crystals, which are oriented such that the walk-off directions are opposite to each other, as shown in Fig. 2.6. There is still a small walk-off within each of these crystals, but its overall effect can be strongly reduced.

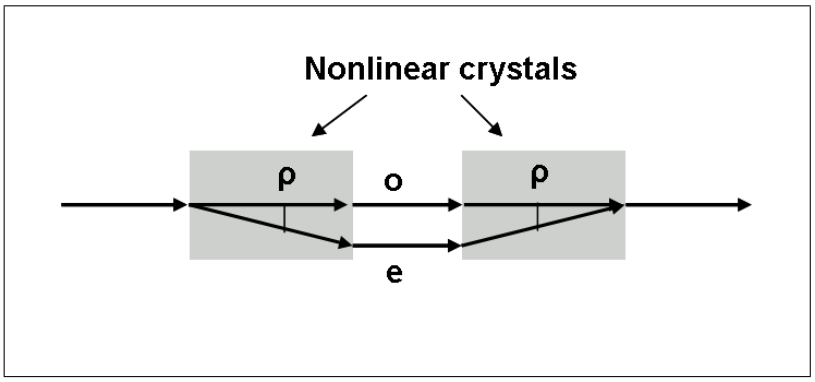

Figure 2.6: Walk-off compensation scheme using two identical nonlinear birefringent crystals oriented such that the walk-off directions are opposite to each other.

Noncritical phase-matching is advantageous for two reasons: first, it is less sensitive to a beam divergence, which tends to lower the conversion efficiency and second, the walk-off angle for this case is zero, which places less constraints on the beam size and the crystal length.

In addition to the walk-off problem, low effective nonlinear coefficient, and inconvenient phase-matching temperatures and angles [25] in birefringent phase-matching, the range of wavelengths over which a particular crystal can be used is determined by the indices of refraction for light polarized along the principal axes and by the second-order nonlinear susceptibility tensor. Efficient nonlinear conversion requires not only the phase-matching condition to be satisfied for the wavelengths of interest in a particular direction, but also a significant nonlinear optical coefficient along the phase-matching direction.

2.4.2 Quasi-phase-matching (QPM)

An alternative technique to BPM for compensating the phase mismatch caused by the chromatic dispersion of the nonlinear crystal is quasi-phase-matching (QPM), first introduced by Armstrong et al. in 1962 [17]. Unlike BPM, QPM is not perfect phase-matching, as it allows some phase slip between the interacting waves. However, as the phase difference between the interacting waves reaches π (and, hence, will start to reverse the power flow) through the propagation of one coherence length (L_c) in the medium, an additional phase difference of π is introduced to the acquired phase so as to make the interactive waves coming in phase again to retain monotonic power flow from the driving nonlinear polarization to the generated polarization. The introduction of the additional phase, π, is realized by modulating the nonlinear coefficient of the medium with a period twice the coherence length, in other words, changing the sign of the nonlinear coefficient after each coherence length. This can

be understood from Fig. 2.7 (a) which shows how the phasor of the generated field is evolving while propagating through the nonlinear medium. Fig. 2.7 (b) shows the periodic reversal of the nonlinear coefficient after each coherence length (L_c) along the length of the medium. The periodic phase correction inherent in QPM

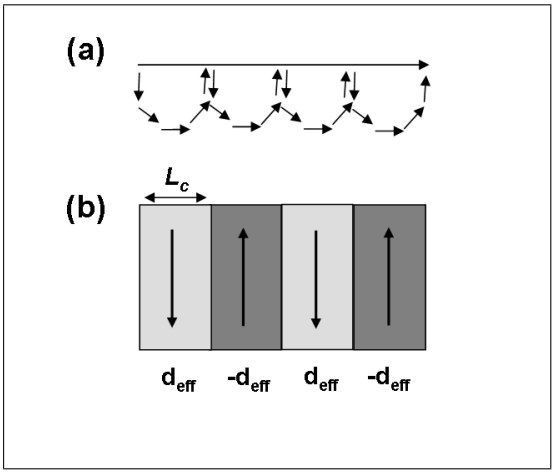

Figure 2.7: Diagram for (a) phasor representation and (b) periodic reversal of nonlinear coefficient for QPM technique.

causes the generated output power to build-up in a stepwise fashion, as shown in Fig. 2.8. As evident in Fig. 2.8, the build-up of the output power is less rapid than the corresponding output with birefringent phase-matching, generally leading to a lower conversion efficiency if the nonlinear coefficient is the same as the effective nonlinearity, d_{eff}, reduced by a factor of $2/\pi$. Despite this, the great advantage of QPM is that it permits to use the same polarization direction for all interacting waves, and this often corresponds to accessing the highest diagonal coefficients of the nonlinear tensor. As a result, in practice, the conversion efficiency in case of QPM technique can be significantly higher than that of BPM technique. In addition to accessing higher nonlinear coefficients, the great advantage of QPM is that it can be employed when BPM is impossible in materials with low birefringence and can provide noncritical phase-matching for any nonlinear interaction permitted by the

transparency range of the material. Since in QPM, the nonlinear coefficient of the

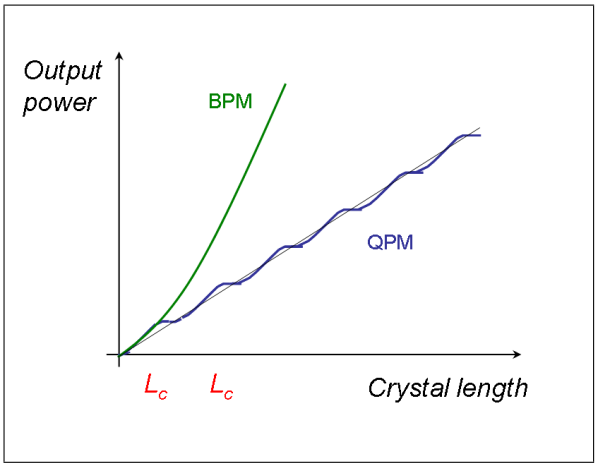

Figure 2.8: Output power as a function of length for SHG using BPM and QPM.

material is spatially modulated with the period $\Lambda = 2L_c$, the nonlinear modulation can be described by a function, $g(x)$, which is a rectangular function with the period of Λ and magnitude of ± 1. The function $g(x)$ can be expressed by a Fourier expansion [26] as:

$$g(x) = \sum_{m=-\infty}^{\infty} G_m e^{(iK_m x)} \tag{2.26}$$

where G_m is the magnitude and K_m is the m^{th}-harmonic grating wave vector and is represented as:

$$K_m = \frac{2\pi m}{\Lambda} \tag{2.27}$$

The direction of the grating period is along the direction of propagation, x, of the electromagnetic waves. The effective nonlinear coefficient can now be written as:

$$d(x) = d_{ijk} g(x) \tag{2.28}$$

and, the phase-mismatch can be written as $\triangle k_{tot} = \triangle k + K_m$. Nonlinear processes will be efficient if $\triangle k_{tot} \approx 0$. This condition is fulfilled for two conjugate terms in the series of $g(x)$. Thus, the effective nonlinear coefficient for QPM is reduced to $d_{eff} = G_m d_{ijk}$, where G_m can be represented as [26]:

$$G_m = \frac{2}{\pi m} sin(m\pi D) \tag{2.29}$$

D is the duty factor of the grating and can be represented as the ratio of the grating length and the grating period. For optimum grating duty factor, i.e., $D = 50\%$, the optimum effective nonlinearity factor can be represented as:

$$d_{eff} = \frac{2}{\pi m} d_{ijk} \tag{2.30}$$

Although the theory of QPM was formulated in 1962 [17], the development of QPM materials was held back due to the lack of suitable fabrication techniques. Therefore, BPM was the only technique to realize efficient nonlinear processes. However, during last few decades, the advancement of periodic-poling techniques has enabled to develop excellent QPM crystals for optical frequency conversion processes.

The most popular technique to fabricate quasi-phase-matched crystals is periodic reversal of the domains of ferroelectric materials such as, lithium niobate ($LiNbO_3$), potassium titanyl phosphate ($KTiOPO_4$), and lithium tantalate ($LiTaO_3$). Ferroelectric materials have spontaneous electronic polarization. Applying a strong periodic electric field, this spontaneous electronic polarization can be inverted by the movement of the ions between two subsequent positions in the crystal lattice. Due to the lack of inversion symmetry, this polarization inversion results in the sign change of the components of the nonlinear susceptibility tensor, hence the sign of

the effective nonlinear coefficient d_{eff}. The periodicity of the domain reversal is twice the coherence length ($2L_c$) of the particular second-order nonlinear process that needs to be quasi-phase-matched. By depositing a periodic pattern of micro-structured electrodes using lithographic techniques on one of the faces along the wave propagation direction of the crystal, and applying a high voltage, a permanent periodic domain reversal (know as the grating) can be produced for quasi-phase-matching. Typical poling periods are between 5 and 50 μm. Domain reversal occurs for a field strength above the so-called coercive field strength of the ferroelectric material, which is typically in the multi kilo-volts range. For example, in order to pole the congruently grown $LiNbO_3$, the typical required field strength is ∼21 kV/mm. Great care is required to avoid discharges in air and destruction of the crystal. The poling process becomes particularly even more challenging when trying to pole thick samples (more than 0.5 mm), where the poling quality is sometimes good only near the electrodes. Another challenge is to achieve a high poling quality for small poling periods (well below 10 μm), as required, for example, for frequency doubling into the visible and UV spectral range. Stoichiometric lithium niobate (SLN) has a much lower coercive field strength of roughly ∼2 kV/mm, which greatly facilitates periodic poling, even for thicker samples (5 mm).

However, the main drawbacks of the QPM technique include the limited number of available materials and the range of wavelengths that can be phase-matched in those materials.

2.5 Optical parametric oscillator

As shown in Fig. 2.1 (b), when a nonlinear crystal is pumped by a strong laser beam, through the process of parametric fluorescence, signal and idler waves are generated.

Due to the low gain (of the order of 0.1 to 1000 percent for typical nonlinear materials and pumping intensities) of the process, the realization of parametric devices necessitate positive feedback to the generated waves for macroscopic amplification . Therefore, in most cases, parametric devices are operated in an oscillator configuration, as in a conventional laser, by enclosing the nonlinear gain medium within an optical cavity as shown in Fig. 2.1 (c). In this configuration, the device is known as an optical parametric oscillator (OPO) [2; 27]. OPOs are light sources similar to a laser, but the main difference between OPOs and laser is that the optical gain in OPOs comes from parametric amplification in a nonlinear crystal rather than from stimulated emission as in the laser. The optical gain in the OPO is instantaneous, so that gain is available only in the presence of pump. Today, OPOs are a mature technology, particularly in pulsed operation, and several reviews of their physics and applications have been presented [28–30].

The main attraction of OPOs is that the signal and the idler wavelengths can be varied over wide ranges. Thus, it is possible to access wavelengths (e.g., in the mid-infrared, far-infrared or terahertz spectral region) which are otherwise difficult or impossible to obtain from any laser due to the unavailability of the laser gain medium. All time-scale from continuous-wave to femtosecond, and wide wavelength tunability, are also possible. The main limitation of the OPOs is that they require a pump laser source with high optical intensity and relatively high spatial coherence.

When the parametric process is phase-matched, parametric noise is amplified during the propagation through the nonlinear material. The single-pass parametric gain in the nonlinear crystal is represented as [31]:

$$G = \Gamma^2 L^2 \frac{sinh^2(\sqrt{\Gamma^2 - \frac{\triangle k^2}{4}} L)}{(\Gamma^2 - \frac{\triangle k^2}{4}) L^2} \tag{2.31}$$

Here, the parametric gain factor, Γ, is given by

$$\Gamma^2 = \frac{2\omega_s\omega_i d_{eff}^2 I_p}{\epsilon_o n_p n_s n_i c^3} \tag{2.32}$$

where ω_s and ω_i are the signal and the idler frequencies. n_p, n_s, and n_i are the refractive indices of the material for the pump, signal and idler wavelengths, respectively. The factor, $d_{eff}/(\sqrt{n_p n_s n_i})$, contains the physical parameters those are completely dependent upon the material, hence, known as the figure-of-merit for the material. It is often useful to represent the gain factor (Equation (2.32)) in the form [30]:

$$\Gamma^2 = \frac{2\omega_s\omega_i d_{eff}^2}{\epsilon_o n_p n_s n_i c^3}(1-\delta^2) I_p \tag{2.33}$$

where δ is the degeneracy factor defined through:

$$1+\delta = \frac{\lambda_0}{\lambda_s}; 1-\delta = \frac{\lambda_0}{\lambda_i}; (0 \leq \delta \leq 1) \tag{2.34}$$

$\lambda_0 = 2\lambda_p$ is the degenerate wavelength. λ_p, λ_s, and λ_i are the wavelengths of the pump, signal and idler radiations respectively. It is clear from Equation (2.33) that the gain in a parametric amplification process has a maximum value at degeneracy, where $\delta \sim 0$, and the gain decreases for operation away from degeneracy as $\delta \rightarrow 1$.

As in a laser, the OPO reaches operation threshold when the parametric gain equals the cavity losses. The losses in an OPO cavity originate from the scattering, parasitic reflections, and the absorption in the crystal, but, primarily from the finite reflections of the cavity mirrors. In fact, for an OPO to produce any output, at least either the signal or idler must have some fraction transmitted out of the cavity in order to generate the desired beam. Depending on the number of waves resonating in the optical cavity, it is named as singly-resonant oscillator (SRO) (see Fig. 2.9

(a)), when only one wave (signal or idler) is resonating in the cavity; doubly-resonant oscillator (DRO) (Fig. 2.9 (b)), when both the signal and idler are resonating; triply resonant oscillator (TRO) (Fig. 2.9 (c)), when the pump is also resonating along with the signal and the idler in the cavity; and finally ,the pump-resonant or pump-enhanced (PE-) SRO (Fig. 2.9 (d)), when the pump as well as one of the generated waves (signal or idler) are resonated.

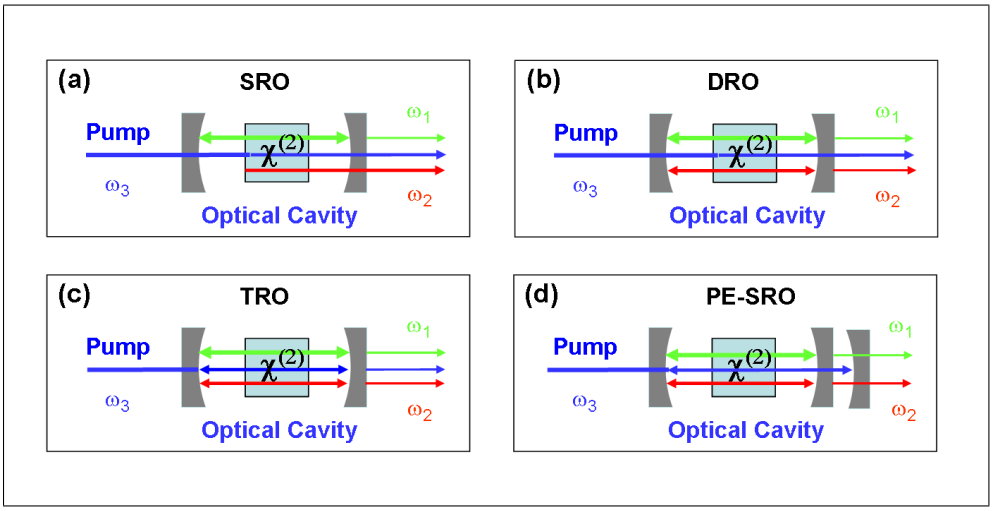

Figure 2.9: Cavity configurations for OPOs: (a) singly resonant (SRO), (b) doubly resonant (DRO), (c) triply resonant (TRO) and (d) pump enhanced (PE-SRO). Blue, green, and red colors indicate pump, signal, and idler waves, respectively. Nonlinear media has χ^2 nonlinearity.

The advantage of DROs and TROs is that the threshold pump power can be much lower (in the mW range) as compared to other configurations. This is particularly interesting for cw operation, where the threshold pump power is typically high due to the low parametric gain of the nonlinear materials. However, the tuning behavior and stable operation of DROs and TROs is complicated, since each resonant wave of the OPO has to fulfill the cavity conditions for longitudinal modes, energy conservation, and phase-matching. Despite of the highest operation threshold over the other OPO configurations, cw SROs offers the most viable solution for parametric generation of high-power, cw, single-frequency radiation over extended

spectral regions.

Here, we discuss mainly the cw SRO, as it is relevant to the present work. Treatment for other time scales (pulse regime) and other oscillation configurations can be found elsewhere [28–30].

2.6 Steady-state CW SRO threshold

Assuming the pump depletion and losses of the signal wave from the cavity are small, we may consider the signal wave (the electric field) to be constant throughout the nonlinear medium. Hence, the change of the idler field with the propagation through the nonlinear crystal, as represented by the coupled-wave Equation (2.16), can be written as [30]:

$$\frac{dE_i}{dx} = [\frac{id_{eff}\omega_i}{cn_i}]E_pE_s^* = Constant \tag{2.35}$$

Hence, the electric field of the idler wave grows linearly from zero at the input face of the crystal with distance (x-axis) through the nonlinear crystal, according to

$$E_i = i\kappa_2 E_p E_s^* x \tag{2.36}$$

where, $\kappa_2 = d_{eff}\omega_i/(cn_i)$. Now, using Equations (2.15) and (2.36), the change in the electric field of the signal can be represented as:

$$\frac{\delta E_s}{E_s} = \frac{\kappa_1\kappa_2 E_p E_p^* L^2}{2} \tag{2.37}$$

where $\kappa_1 = d_{eff}\omega_s/(cn_s)$. L is the length of the nonlinear medium. Using the relationship between the increment of the electric field and the intensity, e.g, $\delta I/I =$

$2\delta E/E$, the change of the signal intensity can now be represented as:

$$\begin{aligned}\frac{\delta I_s}{I_s} &= \kappa_1\kappa_2(E_pE_p^*)L^2 \\ &= \frac{2Z_o\kappa_1\kappa_2 I_pL^2}{n_p}\end{aligned} \tag{2.38}$$

where the pump intensity I_p is given by the expression [30]:

$$I_p = \frac{n_pE_pE_p^*}{2Z_o} \tag{2.39}$$

and $Z_o = (\mu_0/\epsilon_0)^{1/2}$ is the permitivity of free space.

If α_2 is defined as the fractional round-trip loss of the signal in the cavity, then at threshold, the net loss of signal, $\alpha_2 I_2$, is equal to the increment of the signal, and can be written as:

$$\frac{2Z_o\kappa_1\kappa_2 I_pL^2}{n_p} = \alpha_2 \tag{2.40}$$

Substituting the values of κ_1, κ_2 and Z_o in Equation (2.40), we can finally obtain the threshold pump intensity required to reach SRO oscillation as:

$$I_{th} = \frac{\alpha_2 c\epsilon_0 n_p n_s n_i \lambda_s \lambda_i}{8\pi^2 L^2 d_{eff}^2} \tag{2.41}$$

where λ_1 and λ_2 are the idler and the signal wavelengths, respectively.

In a similar treatment, threshold pump intensity for DRO can be found as:

$$I_{th} = \frac{\alpha_2 c\epsilon_0 n_p n_s n_i \lambda_2 \lambda_1}{8\pi^2 L^2 d_{eff}^2}\frac{\alpha_1}{4} \tag{2.42}$$

where α_1 is the round trip loss of the idler in the DRO cavity.

Equations (2.41) and (2.42) show that the threshold of the DRO is reduced by a factor of $(\alpha_1/4)$ as compared to the SRO, implying a substantial reduction in threshold of the DRO compared to the SRO.

2.7 Tuning of the SRO

In an OPO, the wavelengths of the generated radiations are determined by two empirical relations, the energy conservation and the momentum conservation (phase-matching), as discussed in Section 2.3. Unlike lasers, one of the main advantages of an OPO is that the phase matching conditions can be changed. So, for instance, by changing the phase-matching relation, by any means, converts the OPO into a tunable source of coherent radiation. Any physical parameter that influences the index of refraction of the nonlinear medium can be used for tuning. The most common parameters to use are the crystal angle (*angle tuning*), the QPM domain grating period, or the crystal temperature (*temperature tuning*). In addition, it is also possible to vary the signal and the idler wavelengths by keeping the crystal parameters constant and changing the wavelength of the pump (*pump tuning*). For example, Fig. 2.10 shows a typical wavelength tuning of a PPLN-based SRO by changing the crystal temperature and the domain grating period. The small differences between theoretical data (solid line) and the experimental data (*) can be attributed to many factors including temperature measurement errors, grating period offsets in fabrication, and inaccuracy in the refractive index model. Other, less common, tuning methods include electro-optic or pressure tuning by applying an external electric field or a mechanical stress to the nonlinear material respectively. These methods are particularly useful for fine-tuning of the OPO output [30].

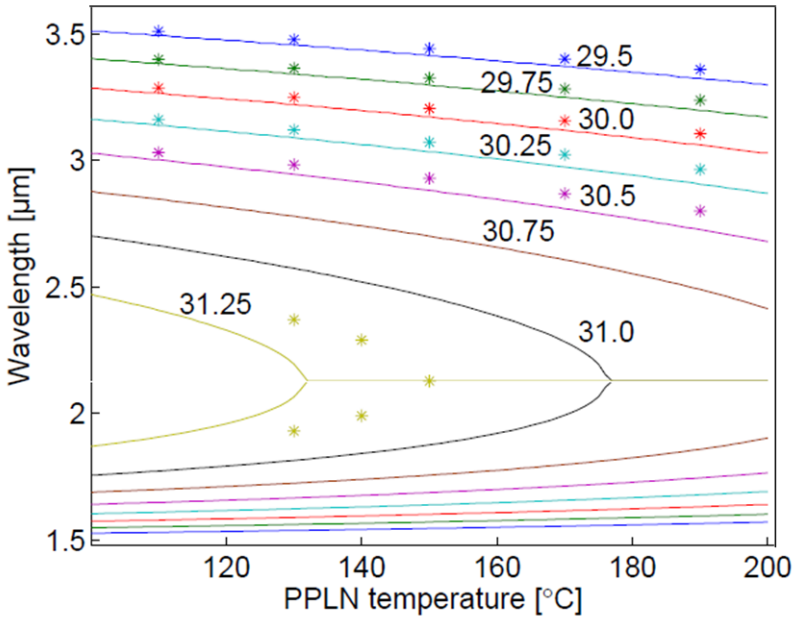

Figure 2.10: Signal and idler wavelengths for a PPLN SRO depending on temperature. The solid curves represent the theoretical tuning and are labeled by the domain grating periods in μm. The stars show experimental data.[32]

Chapter 3

Design issues for cw SROs

The principal criteria for the design of an optimum OPO device, are:

(a) Selection of suitable nonlinear material,

(b) use of laser a suitable pump source, and

(c) an optimum cavity design using perfect focusing parameters for the pump and the resonant signal wave.

3.1 Nonlinear material

There are several important parameters that have to be taken into consideration when selecting the nonlinear crystal for an OPO. This includes a broad transparency range, a high optical damage threshold, good thermal conductivity, phase-matching possibility in the wavelength range of interest, mechanical hardness, a high nonlinear figure-of-merit, availability in high quality and in large size, chemical stability, and at a low cost.

As described by Equation (2.32) in Chapter 2, the parametric gain (customarily called the nonlinear figure-of-merit, $FOM \equiv d_{eff}/\sqrt{n_p n_s n_i}$, of the nonlinear crystal) is proportional to the effective nonlinearity and inversely proportional to the

square-root of the refractive indices of the material. Since infrared materials, in general, have higher refractive indices, hence one would expect a lower FOM in such materials. However, Millers rule implies that $d_{eff} \propto n^6$, so that the $FOM \propto n^{9/2}$. Hence, the infrared materials with larger indices may actually exhibit higher FOM. Since the parametric gain factor, Γ, (Equation (2.32)), is proportional to the inverse square-root wavelengths $[(\propto \lambda_s\lambda_i)^{-1}]$, this results in a lower nonlinear gain for longer signal and idler wavelengths. However, the overall contributions of the refractive indices and the wavelength factors, mean that infrared materials, generally, exhibit significantly higher FOM values than those of the visible and ultraviolet materials.

It is also desirable for the material to display large tolerances to possible finite deviations in the spectral and spatial quality of practical pump lasers. The parametric gain bandwidth of the nonlinear medium of length L, may be defined by the expression $|\triangle kL| \sim 2\pi$. Using Taylor-series expansion of $\triangle k$ [33; 34] for the wavelength and the angular spread of the pump, one can calculate the wavelength acceptance bandwidth, $\triangle \lambda L$, and angular acceptance bandwidth, $\triangle \theta L$, respectively, for given experimental boundary conditions. In a similar manner, one can calculate the temperature acceptance bandwidth, $\triangle TL$, for the noncritical phase-matching scenario, which measures the sensitivity of the phase-matching, and, thus the parametric gain, to changes in the crystal temperature. Detailed calculations of the acceptance bandwidths depend on the type of phase-matching and the dispersion properties of the specific nonlinear material and can be found elsewhere [18; 34]. Thus, for a given crystal length, L, there is an upper limit to the maximum allowable pump linewidth and angular divergence for efficient parametric generation. On the other hand, for a given pump linewidth and angular divergence, there is also an upper limit of the useful crystal length for maximum nonlinear gain. The inverse re-

lationship between the crystal length and the acceptance bandwidths signifies that shorter crystal lengths can, in fact, tolerate larger deviations in the pump beam quality and vice versa. As a general rule, for the attainment of maximum nonlinear gain and a minimum OPO threshold, it is advantageous to use materials with large spectral, angular, and temperature acceptance bandwidths [30].

Another important parameter to consider in selecting the nonlinear material is the double-refraction of the birefringent material, which leads to a spatial walk-off effect. Spatial walk-off in the material results in major reductions in the energy exchange among the interacting fields along the direction of propagation, hence, again, sets an upper limit to the useful length the crystal for maximum gain. The effective length of the crystal in the presence of birefringence can be represented as $L_a = w_p\sqrt{\frac{\pi}{\rho}}$, where w_p is the radius of the pump beam and ρ is the double-refraction angle [35]. It is clear that for longer effective lengths, it is desirable to use nonlinear crystals with small double-refraction. In practice, the effective length (L_a) should be greater than the physical length of the crystal. Hence, we need to select a material with low double-refraction. But the double-refraction phenomenon is also, at the same time, exploited for the birefringent phase-matching, so it is necessary to find a compromise. On the other hand, for a given ρ, the effective length of the crystal can be increased by increasing the pump beam waist radius. But, in practice, this is not always possible for low- to medium-power pump lasers as the operation threshold of the parametric processes increase with the increase of the pump beam diameter.

Noncritical phase-matching can effectively be used, by propagation along a principal dielectric axis, where $\rho = 0$ and the effective length $L_a \to \infty$. There are a few potential techniques for partial walk-off compensation, including elliptical focusing [36], noncollinear phase-matching [37; 38], and two-crystal configuration [23; 24]. So, in conclusion, in the presence of double-refraction, in addition to the acceptance

bandwidth considerations, the spatial walk-off places an additional restriction on the maximum crystal length.

3.1.1 Limitations of nonlinear materials

In addition to the requirements discussed above, all nonlinear materials suffer from several limitations for further improvement of the device performance. Many of these limitations are related to the intrinsic properties of the material such as, damage threshold, group velocity mismatch, group velocity dispersion, two-photon absorption, and intrinsic linear absorption, and these are, in some ways, unavoidable. Although cw operation eliminates the limitation of the group velocity mismatch and the group velocity dispersion, instead the major limitation in this regime comes due to the optical damage. Because of the high operation threshold of the cw SROs, the nonlinear material should withstand high pump intensities. Optical damage may be caused by several different mechanisms including thermal heating, induced absorption, self-focusing, stimulated Brillouin scattering, dielectric breakdown, and can be of various types like reversible and irreversible damages.

Photorefraction:

In 1966, Ashkin et al [39] observed optically-induced refractive index inhomogeneities in the ferroelectric materials $LiNbO_3$ and $LiTaO_3$ while illuminated by visible radiation. Since then, many studies have been performed to understand this light-induced index change, commonly known as photorefraction, with the corresponding damage known as photorefractive damage. Photorefractive damage leads to beam distortions and non-uniformities in birefringence and phase-matching. It is a reversible damage mechanism, and can be alleviated by illuminating the crystal with ultraviolet radiation or by elevating its temperature. Although these index changes are undesirable in the field of nonlinear optics, they can be used for optical

data storage and a multitude of other applications. In particular, magnesium doping [40] and stoichiometry control [41] have been shown to be effective for increasing the photoconductivity of both $LiNbO_3$ and $LiTaO_3$, thus reducing the susceptibility to photorefractive damage.

Laser-induced damage:

Laser-induced damage is of great importance for the design and successful operation of parametric devices. It has also been argued to be a probabilistic effect based on an avalanche optical AC breakdown similar to DC dielectric breakdown [42]. Laser-induced damage, under various conditions, is very much dependent on crystal growth, impurities level and preparation conditions. The subject has been extensively studied and reported in the literature. Yet, the exact evaluation of damage thresholds and identification of the mechanisms responsible for optical damage in different materials remains a difficult task [30].

Absorption:

Both the linear and nonlinear material absorption are perhaps the ultimate limitation of the parametric processes. These absorptions can lead to many possible effects that may limit the performance of nonlinear devices. The most common result of absorption is the thermal effects including (a) thermal dephasing; which degrades the perfect phase-matching, and hence the maximum efficiency of the devices, (b) thermal lensing; which degrade mode matching between the pump and the generating waves and can also lead to laser-induced material damage, (c) thermal stress; causing mechanical damage to the crystals. Besides these, absorption of the newly generated radiation reduces the overall efficiency of the nonlinear devices. The absorption is related to the concentrations of impurities and native defects. Hence, proper care and improvement in the growth techniques are important in reducing the intrinsic absorption of nonlinear materials to some extent.

3.2 Laser pump source

The selection of laser source to pump cw SROs is determined mainly by the phase-matching requirements to access the desire wavelength region of interest. The pump wavelength should obviously be within the transparency range of the nonlinear material. As the operation threshold of the cw SROs is quite high, therefore, the pump source should be sufficiently intense to achieve sufficient nonlinear gain to reach operation threshold. As the power stability of the cw SROs is dependent on the power fluctuation and the pointing stability of the pump, hence the pump power should be highly stable with very high pointing stability and low beam divergence. Considerations of phase-mismatch place further demands on the spectral and spatial coherence of the pump beam. The parametric gain is strongly dependent on the phase-mismatch parameter, $\triangle k$, and the deviation of $\triangle k$ from $\triangle k = 0$ result in severe reductions in nonlinear gain. The highest gain is available at $\triangle k = 0$. As the practical laser sources have finite spectral bandwidth and spatial divergence, despite the use of phase-matching techniques, all the spectral and spatial components of the beam can not be brought into perfect phase unison simultaneously to realize perfect phase-matching ($\triangle k = 0$). Hence, the pump laser should have high spectral and spatial coherence. The maximum allowable pump bandwidth and divergence can be calculated from considerations of phase-mismatch [43], which show that efficient operation of cw SROs necessitates laser pump sources of narrow linewidth and low beam divergence.

3.3 SRO cavity configuration

The typical cavity configurations for cw SROs cavities are shown in Fig. 3.1, among which the linear cavity is the simplest one, consisting of the nonlinear crystal en-

closed between two mirrors. The pump beam is focused inside the nonlinear crystal. The in-coupling mirror transmits the pump and reflects the signal, and the out-coupling mirror is partially reflecting for the signal and transmits pump and idler. The mirrors are generally curved to match the resonant mode to the pump mode. The V-shaped and X-shaped cavities have the possibility of introducing additional components, for example etalons, for narrowing linewidth, or additional nonlinear crystals for other second-order nonlinear processes, in the cavity without exposing them to the high pump intensity. They also can offer the possibility to double-pass the pump radiation along with the signal to reduce the SRO threshold. The ring SRO cavity is the most difficult configuration among the other designs shown in Fig. 3.1, but it has lot of advantages over other configurations, like, no pump radiation is reflected back into the laser; it removes the need of an optical isolator. It also offers the possibility of introducing etalons for frequency selection and control at the second beam waist of the cavity without changing the cavity stability. Single-pass of the resonating wave through the crystal in the ring cavity for every round-trip reduces the losses due to material absorption and crystal coating, hence reduces the SRO threshold, and also minimizes the thermal effects within the nonlinear crystal. All these basic configurations come in a large number of variants, including the use of walk-off compensating schemes to use longer crystal.

Here, we describe the optimum cavity design for a cw SRO in ring cavity configuration using ABCD matrix analysis [44]. For the best performance of the SRO, one need optimum overlap of the pump beam and the resonating signal beam [45]; the confocal parameter of the pump beam needs to be equal to that of the signal beam. To achieve this, the focal point of the pump laser needs to be at the same position (at the center of the nonlinear crystal) as the focal point of the signal beam inside the stable ring resonator. Using Gaussian beam transformation matrices, the

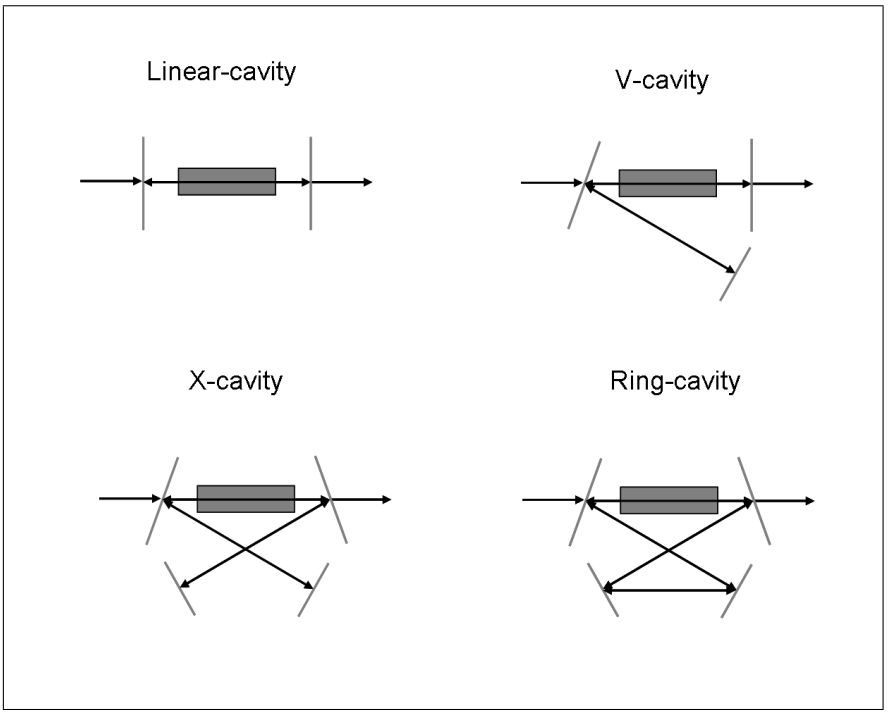

Figure 3.1: Examples of different SRO cavity configurations.

signal beam waist can be calculated along the cavity dimensions [46].

3.3.1 Gaussian beam transformation matrices

Let us assume that an unaltered Gaussian beam propagating in a straight line along z-direction with a minimum beam waist, w_0 at $z = 0$ i.e, $w(0) = w_0$. If the beam waist, $w(z)$, and radius of curvature, $R(z)$, of the wavefront is known at a specific location of the Gaussian beam, then the beam waist and radius of curvature of the beam at any position can be estimated using the following equations:

$$R(z) = z\left(1 + \frac{z_0^2}{z^2}\right) \tag{3.1}$$

$$w(z) = w_0^2\left(1 + \frac{z^2}{z_0^2}\right) \tag{3.2}$$

where $z_0 = \pi n w_0^2/\lambda$ is known as the *Rayleigh range*, $b = 2z_0$ is called as *Confocal parameter*, n is the refractive index, and λ is the wavelength of the Gaussian beam.

The Gaussian beam at a distance z can be written in simple way using the complex beam parameter $q(z)$ as:

$$q(z) = z - iz_0 \tag{3.3}$$

The relationship of complex beam parameter $q(z)$ with $R(z)$ and $w(z)$ is given by:

$$\begin{aligned} \frac{1}{q(z)} = \frac{1}{z - iz_0} &= \frac{z + iz_0}{z^2 + z_0^2} \\ &= \frac{1}{z\left(1 + \frac{z_0^2}{z^2}\right)} + i\frac{1}{z_0\left(1 + \frac{z_0^2}{z^2}\right)} \\ &= \frac{1}{R(z)} - i\frac{\lambda}{\pi n w^2(z)} \end{aligned} \tag{3.4}$$

By taking the real and imaginary parts of Equation (3.4), we can obtain $R(z)$ and $w(z)$ as:

$$\frac{1}{R(z)} = Re\left(\frac{1}{q(z)}\right) \tag{3.5}$$

and

$$\frac{1}{w^2(z)} = -\frac{\pi n}{\lambda} Im\left(\frac{1}{q(z)}\right) \tag{3.6}$$

The ray matrices, also known as ABCD matrices, relate the complex beam parameter q_1 at a plane 2 to the value q_0 at plane 1 as:

$$q_2 = \frac{Aq_0 + B}{Cq_0 + D} \tag{3.7}$$

The general form of the ray matrix or $ABCD$ matrix is: $M = \begin{pmatrix} A & B \\ C & D \end{pmatrix}$ where, A, B, C and D are the ray matrix elements. The ray matrix analysis is a convenient way to describe the ray propagation through different media as a sequence of events that can be combined by matrix multiplication to yield a final result. For an example, the ray propagation from an object to a lens, refraction though the lens and then propagated to the image location can be represented using a single matrix, which will be obtained by multiplying the matrices for each event (when ray path changes, it is counted as an event) in reserve direction of ray propagation direction. In this case, to obtain the final matrix, one needs to multiply the matrix for propagation from lens to image location with the lens matrix and finally the matrix for the propagation from object to lens.

The useful ray matrix operators are shown in the Table 3.1

Table 3.1: Ray matrices

$\begin{pmatrix} 1 & d \\ 0 & 1 \end{pmatrix}$	Propagation over a distance d
$\begin{pmatrix} 1 & 0 \\ 0 & \frac{n_1}{n_2} \end{pmatrix}$	Refraction at a flat surface seperating two media of index n_1 and n_2
$\begin{pmatrix} 1 & 0 \\ -\frac{1}{f} & 0 \end{pmatrix}$	Thin lens of focal length f

3.3.2 Calculation of beam waist along the cavity

We calculate the beam waist of the propagating beam at different positions of the ring cavity as shown in Fig. 3.2. For easy understanding, the entire cavity is divided

and marked by capital alphabets. The propagation in the cavity is starting from the plane marked by H (middle of the nonlinear medium) and finishing at the same plane H after a round-trip in the sequence of the planes as $HIJKLMNH$. The

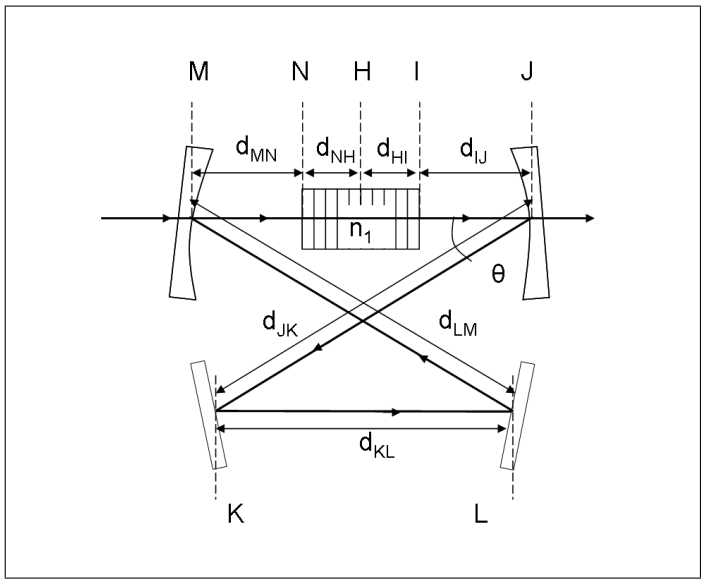

Figure 3.2: Segmentation of the ring cavity to calculate the beam waist of the propagating beam along the cavity.

distance between two planes is represented as d_{XY} where X stands for the initial plane and Y stands for final plane. The refractive index of the nonlinear medium is n_1 and the refractive index of the free space of the cavity is 1. The nonlinear medium is divided into two parts of equal length $d_{HI} = d_{NH}$. At the starting position, the beam will be in its focal point at the center of the nonlinear medium. This means that the wavefront radius of curvature $R(0) = \infty$ and the beam waist $w(0) = w_0$. The complex beam parameter q_0 at the starting point can be represented as:

$$q_0 = i\frac{\pi n_1 w_0^2}{\lambda_s} = iz_0 \tag{3.8}$$

The beam waist at any point of the cavity can be calculated from the following Equation [44]:

$$w(z) = \sqrt{\frac{\lambda_s}{n\pi}\left(\frac{A^2 z_0^2 + B^2}{(AD - BC)z_0}\right)} \tag{3.9}$$

and the corresponding radius of curvature of the propagating can be represented as:

$$R(z) = \left(\frac{A^2 z_0^2 + B^2}{z_0^2 C + B(z_0^2 C^2 + 1)}\right) \tag{3.10}$$

where n is the refractive index of the medium where the beam waist is calculated, A, B, C and D are the elements of the final $ABCD$ matrix at the calculated point, and λ_s is the wavelength of the propagating beam (here it is signal).

Beam waist at the plane H

Using Equation (3.9), the beam waist at the plane H can be represented as:

$$w_H = \sqrt{\frac{\lambda_s}{n_1\pi} z_0} \tag{3.11}$$

where $A = 1$, $B = 0$, $C = 0$, $D = 1$, $AD - BC = 1$, and $n = n_1$. The $ABCD$ matrix is an identity matrix.

Beam waist at the plane I

The beam waist at the plane I can be found from the final matrix (M_I), which is obtained by multiplying the translation matrix M_{HI} for propagation through the crystal length d_{HI} and the refraction matrix M_{ca}, where c represents the crystal and a represents air medium. The final matrix can be represented as:

$$M_I = M_{ca} M_{HI} = \begin{pmatrix} 1 & 0 \\ 0 & n_1 \end{pmatrix} \begin{pmatrix} 1 & d_{HI} \\ 0 & 1 \end{pmatrix} = \begin{pmatrix} 1 & d_{HI} \\ 0 & n_1 \end{pmatrix} \tag{3.12}$$

Using Equations (3.9) and (3.12), the beam waist at the plane I can be represented as:

$$w_I = \sqrt{\frac{\lambda_s}{\pi}\left(\frac{z_0^2 + d_{HI}^2}{n_1 z_0}\right)} \tag{3.13}$$

Beam waist at the plane J

The beam waist at the plane J can be obtained from the final matrix (M_J), which is the multiplication of the matrix M_I and the translation matrix M_{IJ} for propagation of distance d_{IJ} from plane I to the plane J, and can be represented as:

$$M_J = M_{IJ}M_I = \begin{pmatrix} 1 & d_{IJ} \\ 0 & 1 \end{pmatrix}\begin{pmatrix} 1 & d_{HI} \\ 0 & n_1 \end{pmatrix} = \begin{pmatrix} 1 & d_{HI} + n_1 d_{IJ} \\ 0 & n_1 \end{pmatrix} \tag{3.14}$$

Using Equations (3.9) and (3.14), the beam waist at the plane J can be represented as:

$$w_J = \sqrt{\frac{\lambda_s}{\pi}\left(\frac{z_0^2 + (d_{HI} + n_1 d_{IJ})^2}{n_1 z_0}\right)} \tag{3.15}$$

Beam waist at the plane K

The beam waist at the plane K can be found from the final matrix M_K which is multiplication of the translation matrix M_{JK}, for propagation of the distance d_{JK} from the plane J to the plane K and the matrix M_R due to the curve mirror of radius of curvature (R), and the final matrix M_J at the plane J can be represented as:

$$M_K = M_{JK}M_R M_J = \begin{pmatrix} 1 & d_{JK} \\ 0 & 1 \end{pmatrix}\begin{pmatrix} 1 & 0 \\ -\frac{2}{\frac{R}{cos(\theta)}} & 1 \end{pmatrix}\begin{pmatrix} 1 & d_{HI} + n_1 d_{IJ} \\ 0 & n_1 \end{pmatrix} = \begin{pmatrix} \alpha & \beta \\ \gamma & \delta \end{pmatrix} \tag{3.16}$$

where

$$\begin{aligned} \alpha &= 1 - \frac{2d_{JK}cos(\theta)}{R}; \\ \beta &= d_{HI} + n_1(d_{IJ} + d_{JK}) - \frac{2d_{JK}(d_{HI} + d_{IJ}n_1)cos(\theta)}{R}; \\ \gamma &= -\frac{2cos(\theta)}{R}; \\ \delta &= n_1 - \frac{2(d_{HI} + d_{IJ}n_1)cos(\theta)}{R} \end{aligned} \tag{3.17}$$

The term $-2/(R/cos(\theta))$ in the matrix of the curve mirror accounts for sagittal plane of incidence. For tangential plane of incidence, it will be $-2/(Rcos(\theta))$.

Using Equations (3.9), (3.16) and (3.17), the beam waist at the plane K can be represented as:

$$w_K = \sqrt{\frac{\lambda_s}{\pi}\left(\frac{\alpha^2 z_0^2 + \beta^2}{(\alpha\delta - \beta\gamma)z_0}\right)} \tag{3.18}$$

Beam waist at the plane L

The final matrix M_L at the plane L is the product of the translation matrix M_{KL} for propagation of the distance d_{KL} from the plane K to the plane L, and the final matrix M_K at the plane J, and can be represented as:

$$M_L = M_{KL}M_K = \begin{pmatrix} 1 & d_{KL} \\ 0 & 1 \end{pmatrix} \begin{pmatrix} \alpha & \beta \\ \gamma & \delta \end{pmatrix} = \begin{pmatrix} a & b \\ c & d \end{pmatrix} \tag{3.19}$$

where

$$\begin{aligned} a &= \alpha + \gamma d_{KL}; \\ b &= \beta + \delta d_{KL}; \\ c &= \gamma; \\ d &= \delta \end{aligned} \tag{3.20}$$

Using Equations (3.9), (3.19) and (3.20), the beam waist at the plane L, and can be represented as:

$$w_L = \sqrt{\frac{\lambda_s}{\pi}\left(\frac{a^2 z_0^2 + b^2}{(ad - bc)z_0}\right)} \tag{3.21}$$

Beam waist at the plane M

The final matrix M_M at the plane M is the product of the matrix M_R for the curve mirror and the translation matrix M_{LM} for propagation of the distance d_{LM} from the plane L to the plane M, and the final matrix M_L at the plane L can be represented as:

$$\begin{aligned} M_M = M_R M_{LM} M_L &= \begin{pmatrix} 1 & 0 \\ -\frac{2}{\frac{R}{cos(\theta)}} & 1 \end{pmatrix} \begin{pmatrix} 1 & d_{LM} \\ 0 & 1 \end{pmatrix} \begin{pmatrix} a & b \\ c & d \end{pmatrix} \\ &= \begin{pmatrix} e & f \\ f & g \end{pmatrix} \end{aligned} \tag{3.22}$$

where

$$\begin{aligned} e &= a + cd_{LM}; \\ f &= b + d_{LM}d; \\ g &= c - \frac{2}{\frac{R}{cos(\theta)}}(a + cd_{LM}); \\ h &= d - \frac{2}{\frac{R}{cos(\theta)}}(b + d_{LM}d) \end{aligned} \tag{3.23}$$

Using Equations (3.9), (3.22) and (3.23), the beam waist at the plane M can be represented as:

$$w_M = \sqrt{\frac{\lambda_s}{\pi}\left(\frac{e^2 z_0^2 + f^2}{(eh - gf)z_0}\right)} \tag{3.24}$$

Beam waist at the plane N

The final matrix M_N at the plane N is the product of the refraction matrix M_{ac} at the crystal face and the translation matrix M_{MN} for propagation of the distance d_{MN} from the plane M to the plane N, and the final matrix, M_M at the plane M can be represented as:

$$\begin{aligned} M_N = M_{ac}M_{MN}M_M &= \begin{pmatrix} 1 & 0 \\ 0 & \frac{1}{n_1} \end{pmatrix} \begin{pmatrix} 1 & d_{MN} \\ 0 & 1 \end{pmatrix} \begin{pmatrix} e & f \\ g & h \end{pmatrix} \\ &= \begin{pmatrix} q & r \\ s & t \end{pmatrix} \end{aligned} \tag{3.25}$$

where

$$\begin{aligned} q &= e + g d_{MN}; \\ r &= f + h d_{MN}; \\ s &= \frac{g}{n_1}; \\ t &= \frac{h}{n_1} \end{aligned} \tag{3.26}$$

Using Equations (3.9), (3.25) and (3.26), the beam waist at the plane N can be represented as:

$$w_N = \sqrt{\frac{\lambda_s}{n_1 \pi}\left(\frac{q^2 z_0^2 + r^2}{(qt - sr) z_0}\right)} \tag{3.27}$$

Beam waist at the plane H

The final matrix M_H at the plane H after one round-trip is the product of the translation matrix M_{NH} for propagation of the distance d_{NH} from the plane N to the plane H (starting point) and the final matrix M_N at the plane N, and can be represented as:

$$\begin{aligned} M_H = M_{NH} M_N &= \begin{pmatrix} 1 & d_{NH} \\ 0 & 1 \end{pmatrix} \begin{pmatrix} q & r \\ s & t \end{pmatrix} \\ &= \begin{pmatrix} q + s d_{NH} & r + t d_{NH} \\ s & t \end{pmatrix} \end{aligned} \tag{3.28}$$

Using Equations (3.9), and (3.28), the beam waist at the plane H can be represented as:

$$w_H = \sqrt{\frac{\lambda_s}{n_1 \pi}\left(\frac{(q + sd_{NH})^2 z_0^2 + (r + td_{NH})^2}{(tq - sr)z_0}\right)} \tag{3.29}$$

Using the final matrices at subsequent planes, we can calculate the radius of curvature of the propagating beam using the Equation (3.10). The general condition for the stability of the cavity is $-1 \leq (A + D)/2 \leq 1$. Therefore, while doing the cavity design, we need to check that the stability of the designed cavity is well within the stability limits. Sometime, it can be seen that although the stability of the cavity is well within the stability limit, the beam waist after one round trip is different from the starting beam waist. As a result after few round trips the cavity becomes unstable. Therefore, along with stability, we need to be careful whether the difference between the final and the initial beam waists is negligibly small or not.

Another important issue that often comes into play in cw SROs is the thermal lensing effects in the crystal at high pump and signal powers, causing the instability of the SRO cavity. Therefore, thermal lensing effect needs special consideration while designing the SRO cavity. Although it is very difficult to estimate the actual power of the thermal lens, for simplicity, we have considered eight ideal and identical thermal lenses of power $p = 1/8f$ distributed evenly over the entire crystal length. The propagation matrix through half the length of the crystal ($d_{HI} = d_{NH}$) can be represented as:

$$M_{halfcrystal} = \left[\begin{pmatrix} 1 & d_{NH}/8 \\ 0 & 1 \end{pmatrix}\begin{pmatrix} 1 & 0 \\ -\frac{1}{8f} & 1 \end{pmatrix}\begin{pmatrix} 1 & d_{NH}/8 \\ 0 & 1 \end{pmatrix}\right]^4 \tag{3.30}$$

A set of parameters fulfilling the conditions outlined above was found: $d_{HI} =$

$d_{NH} = 15$ mm, $d_{IJ} = d_{MN} = 55$ mm, $d_{JK} + d_{KL} + d_{LM} = 163.5$ mm, $\theta = 12°$, $R = 100$ cm, $f = 20$ mm. The beam radius along the resonator is shown in Fig. 3.3.

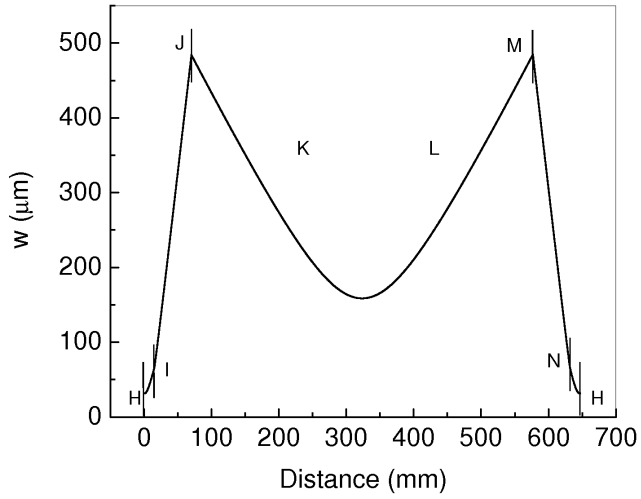

Figure 3.3: Beam radius along the resonator as shown in Fig. 3.2. The position of the subsequent planes are marked.

The pump and signal beam waist at the center of the nonlinear crystal, periodically-poled $LaTiO_3$ are $w_p = 24\mu$m, and $w_s = 31\mu$m, respectively, corresponding to an optimum focusing parameter $\xi = 2$. The pump and signal wavelengths are $\lambda_p = 532$ nm and $\lambda_s = 900$ nm, respectively. The refractive index of the crystal is calculated for pump and signal wavelengths at a crystal temperature $T = 139°$ C. The photograph of such a ring SRO cavity is shown in Fig. 3.4.

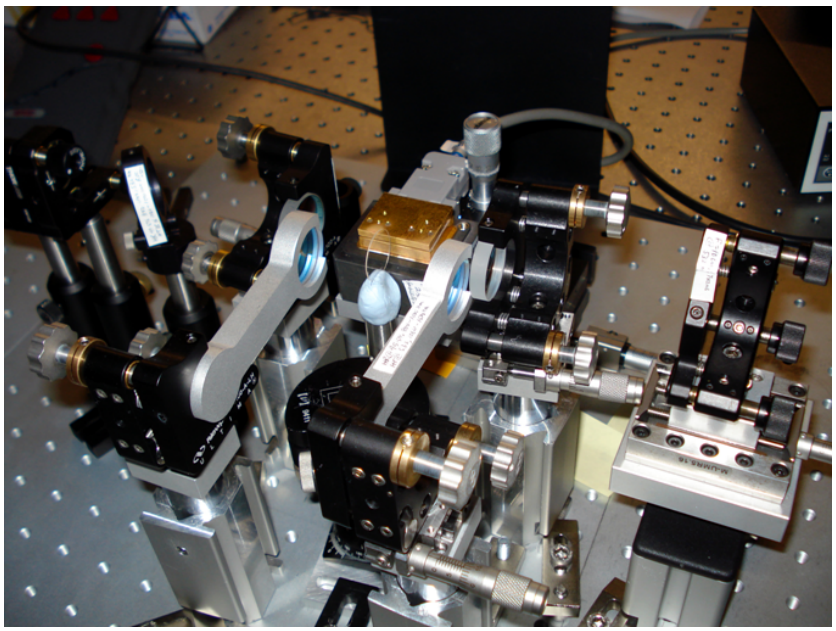

Figure 3.4: Typical experimental setup for cw SRO in ring cavity design.

Chapter 4

Continuous-wave SRO based on MgO:sPPLT

This Chapter constitutes the following journal publications:

1. *High-power, continuous-wave, singly resonant optical parametric oscillator based on MgO:sPPLT*
   G. K. Samanta, G. R. Fayaz, Z. Sun, and M. Ebrahim-Zadeh
   Optics Letters 32, 400–402 (2007).

2. *1.59W, single-frequency, continuous-wave optical parametric oscillator based on MgO:sPPLT*
   G. K. Samanta, G. R. Fayaz, and M. Ebrahim-Zadeh
   Optics Letters 32, 2623–2625 (2007).

4.1 Motivation

Single-frequency, continuous-wave (cw), solid-state light sources with emission covering the visible and near-infrared spectrum are of great interest for a wide range of scientific and technological applications. The development of such sources, is one of the major challenges in laser technology due to the unavailability of suitable laser gain material. Optical parametric oscillators (OPOs) are an especially promising approach toward this goal.

The advent of quasi-phase-matched (QPM) nonlinear materials has had a pro-

found impact on cw OPOs. The vast majority of cw OPOs developed to date have been based on periodically-poled $LiNbO_3$ (PPLN) [47; 48], providing spectral coverage from above $\sim$1 μm to the absorption edge of the material near $\sim$5 μm. For wavelength generation below $\sim$1 μm, the use of PPLN is precluded by photorefractive damage induced by the visible pump or signal radiation. As such, the development of practical cw OPOs for the visible to near infrared, particularly in high-power singly resonant oscillator (SRO) configurations, necessitates the search for alternative QPM materials.

Periodically-poled $LiTaO_3$ (PPLT) [11; 12; 49–51] is one such promising candidate, due to its transparency down to $\sim$ 280 nm, high optical nonlinearity (d_{eff} >10 pm/V), and increased resistance to photorefractive damage. In stoichiometric growth, the coercive field for poling is reduced by 1 order of magnitude from congruent form, and the optical damage threshold is increased by up to 3 orders of magnitude. Doping with MgO also results in further reductions in photorefractive susceptibility to visible radiation. With the ongoing advances in poling technology, the fabrication of bulk MgO-doped stoichiometric PPLT (MgO:sPPLT) with shorter grating periods over long interaction lengths has also become possible, paving the way for the development of practical cw OPOs for the visible and near-infrared based on MgO:sPPLT by using powerful laser pump sources in the visible.

Earlier demonstrations of OPO devices using PPLT and its related derivatives include a pulsed nanosecond SRO based on sPPLT and pumped by a Q-switched Nd:YAG laser at 1064 nm, providing an average power up to 300 mW at 1 kHz and tuning in the near to mid-infrared [49]. Subsequently, a nanosecond SRO based on sPPLT and pumped by a frequency-doubled Nd:YAG laser at 532 nm was demonstrated, delivering a total average power of 490 mW at 3.5 kHz in the visible and near-infrared [50]. More recently, a quasi-cw SRO based on MgO:sPPLT is reported.

Pumped by pulses of width 170 μs from a frequency-doubled Nd:YAG laser at 532 nm, the quasi-cw SRO produces signal pulses of width 70 μs at 635 and 640 nm at 40 Hz, with a peak pulse power of 1.2 W and an average power of $\sim$60 mW [11]. In an earlier report, a PPLT cw SRO pumped at 925 nm by an InGaAs diode laser was demonstrated, generating 244 mW of idler power with tuning over 1.55$-$2.3 μm in the mid-infrared [51]. Soon after, a pump-enhanced PPLT cw OPO using a frequency-doubled Nd:YAG laser at 532 nm was reported, providing 60 mW of output power and tuning in the near to mid-infrared [12].

In a cw SRO configuration, as described in this Chapter, we demonstrate a high-power OPO based on MgO:sPPLT pumped at 532 nm. Using a two-mirror cavity design and double-pass pumping, we generated 1.51 W of cw idler power and tuning across 848$-$1430 nm in the near-IR. A similar device was also reported, providing 100 mW of single-frequency red radiation tunable over 619$-$640 nm [13]. We also demonstrate simultaneous single-frequency operation and high-power performance of a cw SRO based on MgO:sPPLT pumped in the green. Using a compact ring resonator, tight focusing, and intracavity frequency selection, we have achieved a single-mode idler output of up to 1.59W across 1140$-$1417 nm at pump depletions of up to 67% using single-pass pumping.

This Chapter consists with two main sections; high-power, cw SRO; and single-frequency, cw SRO. Section 4.2 presents the first experimental demonstration of a high-power, cw SRO, and Section 4.3 demonstrates simultaneous single-frequency operation and high-power performance of a cw SRO based on MgO:sPPLT pumped in the green.

4.2 High-power, cw SRO

4.2.1 Experimental configuration

Schematic of the experimental setup is shown in Fig. 4.1. The SRO is pumped by a frequency-doubled cw diode pumped Nd:YVO_4 laser at 532 nm (Coherent, Verdi V-10), delivering up to 10 W of single-frequency output in a linearly polarized beam with a diameter of 2.25 mm and an M^2-factor of ∼1.1. Using a confocal interferometer (FSR=1 GHz, Finesse ∼400), we measured the instantaneous linewidth of the laser to be ∼25 MHz. The pump beam was directed to the SRO through an optical isolator and a power attenuator comprising a half-wave-plate and a polarizing beam-splitter cube. A second half-wave-plate was used to yield the correct pump polarization for phase-matching relative to the crystal orientation. The crystal is a 1 mol % bulk MgO:sPPLT sample, 30.14 mm long, 1 mm thick, and 2.14 mm wide (HC Photonics). The sample contains a single grating with a period of Λ =7.97 μm and is housed in an oven with a temperature stability of ± 0.1 °C. The crystal faces are antireflection coated (R<1%) over 800−1100 nm, with 98% transmission at 532 nm. The residual reflectivity at the idler wavelength is 1% to 15% over 1100−1400 nm.

The SRO is configured in a linear standing-wave cavity comprising two concave mirrors, M_1 and M_2, of radius of curvature, r = 50 mm. The cavity mirrors are >99% reflecting for signal wavelengths over 840−1000 nm and >85% transmitting for the idler over 1100−1500 nm, thus ensuring singly resonant oscillation. The input mirror (M_1) has 94% transmission for the pump, while the output mirror (M_2) is >99% reflecting at 532 nm to allow double-pass pumping. A plane mirror, M_3, with reflectivity characteristics identical to M_2, is used as a cutoff filter for the

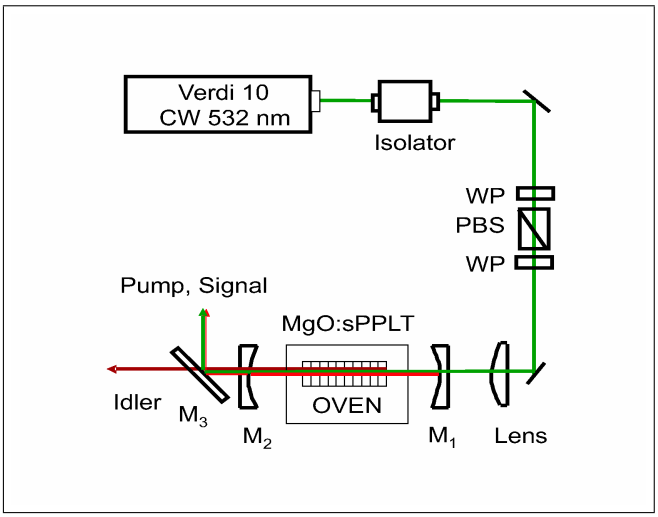

Figure 4.1: Schematic of the experimental design for the MgO:sPPLT cw SRO. HWP, half-wave-plate; PBS, polarizing beam-splitter; M, mirror.

signal and any residual pump, to enable measurements of the idler output.

4.2.2 Design and optimization of the cavity

To optimize SRO operation, we used several focusing conditions, corresponding to different values of the focusing parameter [45]:

$$\xi = \frac{l}{b_p} \tag{4.1}$$

Here l is the length of the crystal and b_p is the confocal parameter of the pump defined as:

$$b_p = k w_{op}^2 \tag{4.2}$$

with the pump wave vector:

$$k = \frac{2\pi n_p}{\lambda_p} \tag{4.3}$$

where n_p is the refractive index of the crystal at the pump wavelength, λ_p, and w_{op} is the waist radius of the pump beam inside the crystal. We used four different focusing

conditions corresponding to ξ = 0.3, 0.8, 1.5, and 2. The optimum SRO operation with maximum idler output power was obtained with ξ =2. The corresponding pump beam waist at the center of the SRO cavity was determined from direct measurements to be $w_{op} \sim 24$ μm. The signal spot size was adjusted by translation of the SRO cavity mirrors, M_1 and M_2, to yield a confocal parameter $b_p = b_s$ (b_s is the confocal parameter at signal wavelength), resulting in a waist radius of $w_{os} \sim$ 32 μm.

4.2.3 Results and discussions

4.2.3.1 Temperature tuning

Figure 4.2 shows the wavelength tuning range of the SRO as a function of the crystal temperature. The solid curve is the tuning range predicted from the Sellmeier relations for stoichimetric $LiTaO_3$ [52], confirming a reasonable agreement between the experimental and the theoretical data. The SRO could be continuously tuned over 1026−848 nm in the signal and 1104−1430 nm in the idler by varying the crystal temperature from 52 °C to 248 °C. Thus, the tuning was continuous over 848−1430 nm, except a small gap near degeneracy (1026−1104 nm) due to the reflectivity falloff of SRO mirrors to prevent doubly-resonant oscillation. The limit to SRO tuning at the extremes of the signal and idler range was set by the maximum operating temperature of the oven at 248 °C. Although theoretically the SRO operation starts at a temperature of 54 °C, experimentally the SRO starts working at 52 °C. The discrepancy between the theoretical and experimental temperature can be attributed to the optically induced temperature rise in the crystal due to the absorption of the pump, therefore necessitating the lower externally-applied phase-matching temperatures.

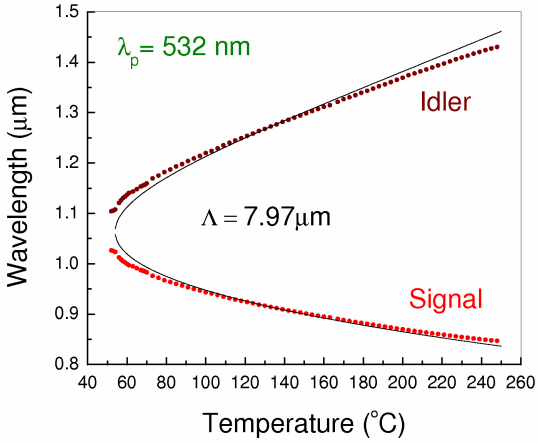

Figure 4.2: Wavelength tuning range of the green-pumped MgO:sPPLT cw SRO as a function of crystal temperature for a grating period of 7.97 μm. Dots represent experimental data where as the line represents theoretical results.

4.2.3.2 Power scaling

The idler output power and photon conversion efficiency as functions of the pump power at the input to the crystal are shown in Fig. 4.3. The data were obtained at 139 °C, corresponding to an idler wavelength of 1282 nm (signal at 910 nm), and represent the idler output only in the forward direction. They do not account for the idler power generated in the backward direction due to the double-pass of the pump through the crystal, but they have been corrected for ∼25% idler loss due to residual reflectivity of mirror M_2 and cutoff mirror, M_3. Because of the relatively high (∼25%) reflection losses of the uncoated transmission optics between the pump laser and SRO, we could deliver a maximum pump power of 7.6 W, as evident in Fig. 4.3. The SRO operation threshold is reached at 2.88 W of pump power. Interestingly, the onset of oscillation is accompanied by the generation of 550 mW of idler power, while below threshold no output power is present. We believe this abrupt behavior may be due to thermal lensing effects. Above threshold, we observe a steady increase in the idler output with a slope efficiency of 26.5%, reaching a maximum single-pass

power of 1.2 W at 5.47 W of pump power. This represents a maximum forward-pass idler power extraction efficiency of 21.9% and a corresponding external photon conversion efficiency of 52.8% from the pump to the idler. At pump powers above 5.47 W, there is a clear roll-off in the idler power and efficiency. The behavior is broadly consistent with the prediction of the theoretical model for a double-pass-pumped SRO, attributed to the effects of pump back-generation. However, the roll-off occurs at a photon conversion efficiency of 52.8%, well below the 100% level predicted by the theory [53].

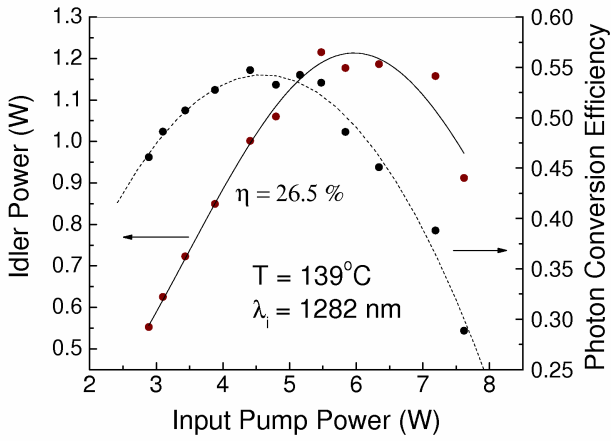

Figure 4.3: Forward-pass idler power and photon conversion efficiency at 1282 nm as functions of input pump power. The crystal temperature is 139 °C.

4.2.3.3 Thermal effects

To identify possible sources of thermal lensing and efficiency roll-off, we performed independent measurements of single-pass crystal transmission at 532 nm. In these experiments, we could deliver up to 9 W at the input to the crystal. The pump was focused to the same waist radius of w_{op}= 24 μm in the crystal, and the transmission loss was recorded as a function of input power. A plot of the transmitted power against input power, as shown in Fig. 4.4, resulted in a straight line, confirming

the absence of two-photon absorption up the maximum available input power of 9 W, corresponding to a focused green intensity of 0.49 MW/cm^2. Hence, the role of two-photon absorption as a possible source of thermal lensing and efficiency roll-off could be discounted. From the slope of the graph, and after correcting for the residual reflectivity of the crystal faces from direct measurements, we determined the linear absorption of the crystal to be 10.14% for the 30.14 mm sample, representing a loss coefficient of 3.23% cm^{-1}. The absence of two-photon absorption, but the presence of significant linear absorption at 532 nm is consistent with earlier reports [50; 54], confirming that single-photon absorption may in fact play a major role in thermal lensing and roll-off effects here. With proper thermal management [55], we expect to be able to control the detrimental effects of thermal lensing in the present device. Another significant factor may be pump-induced infrared absorption of the intracavity signal or the idler, but this has been reported to be reduced to nearly zero in MgO:sPPLT [56]. Experimental determination of this parameter was, however, not possible with our present setup due to the lack of a suitable infrared source. Whereas in later stage with a suitable infrared laser (Fiber laser) we have verified the absence of green-induced infrared absorption in MgO:sPPLT crystal as discussed in Section 7.4.2.2. The measurement techniques for different absorption losses of the nonlinear crystals are described in Appendix A.

4.2.3.4 Power across tuning range

We also recorded the forward-pass idler power obtained across the tuning range of 1104−1430 nm, with the results shown in Fig. 4.5. The data were obtained near the peak of idler power (Fig. 4.3) at an input pump power of 6 W. The SRO could provide as much as 1.51 W of idler output near 1170 nm for 6 W of pump power at a conversion efficiency of 25.2%, and a corresponding photon conversion efficiency

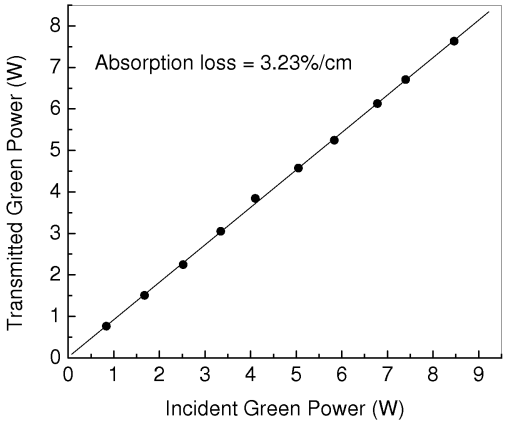

Figure 4.4: Transmission of the MgO:sPPLT crystal at 532 nm.

of 56.7%. Across ∼55% of the total tuning range (1120−1295 nm), the idler power could be maintained above 1 W, with more than 700 mW available over ∼80% of the total tuning range. At the extremes of the tuning range, the SRO could still deliver 500 mW of idler power. We also observed SRO operation at temperatures as low as 52 °C without the onset of spatial instabilities due to photorefractive effects. We did not observe any distortions in the idler and pump beam spatial profiles when operating the SRO well above threshold at the highest input pump powers. These observations are consistent with previously measured photorefractive damage threshold of 2 MW/cm^2 in sPPLT when subjected to green radiation at 514.5 nm [57]. In our SRO, the maximum power of 7.6 W at 532 nm in a beam waist radius of w_{op} ∼24 μm results in a local intensity of 0.84 MW/cm^2 in double-pass pumping, well below the reported photorefractive damage threshold.

We verified the spectral quality of the signal and idler output using a confocal interferometer (FSR=1 GHz, Finesse ∼400). Insofar as the free spectral range of the OPO cavity was 1.03 GHz (optical length 145.5 mm), we could just resolve the signal and idler mode structure by using the interferometer. In the absence of any frequency selection elements within the SRO cavity, we observed signal oscillation

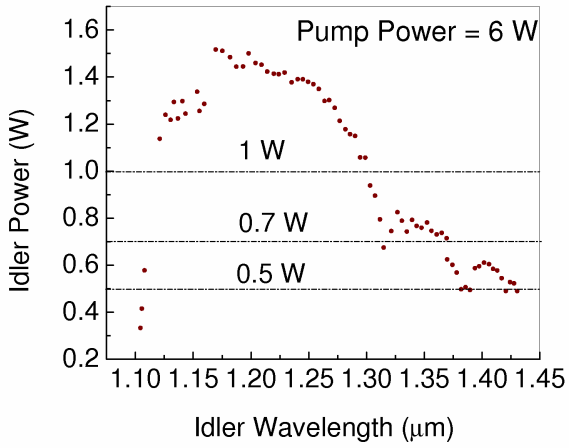

Figure 4.5: Forward-pass idler power across the tuning range for 6 W of pump power at 532 nm.

over more than one longitudinal mode, with frequent hops between two modes. The idler followed similar behavior, oscillating on more than one longitudinal mode, with regular hops between the modes.

4.3 Single-frequency, cw SRO

Given the high-power performance of the cw SRO, the most important feature of the cw SRO, from the spectroscopic application point of view, is its stable single-frequency performance with narrow-linewidth cw radiation over wide range of wavelength. As discussed above, cw SRO in linear two mirror cavity configuration generates multimode radiation, hence we need a strategy to achieve single-frequency operation.

The use of a three-mirror or ring resonator with the inclusion of an intracavity etalon should readily allow the generation of single-frequency signal and idler radiation, making the SRO a promising source of high-power, narrow-linewidth cw radiation with wide and continuous tuning in the visible and near infrared.

4.3.1 Experimental configuration

A schematic of the cw SRO is shown in Fig. 4.6. The SRO is configured in a compact ring cavity comprising two concave mirrors, M_1 and M_2, of radius of curvature r=50 mm, and two plane reflectors, M_3 and M_4. All the mirrors have >99.5% reflectivity over the signal wavelength range of 840−1100 nm and 85%−90% transmission for idler wavelengths over 1100−1500 nm, thus ensuring singly-resonant oscillation.

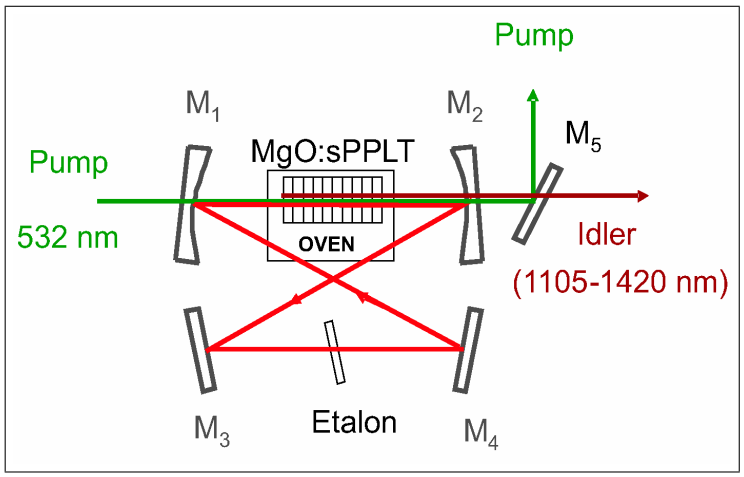

Figure 4.6: Schematic of the high-power, cw, single-frequency SRO based on MgO:sPPLT. The ring cavity consists with four mirrors, $M_{1..4}$, highly reflecting for signal and highly transmitting for pump and idler. M_5 has the same coating as M_2 and also have high reflectivity at pump wavelength to extract idler from residual pump and leaked signal.

The angle of incidence on the concave mirrors, M_1 and M_2, is limited to <5°to minimize astigmatism. The nonlinear crystal is a 1 mol.% bulk MgO:sPPLT sample, 1 mm thick, 2.14 mm wide, and 30.14 mm long, with a single grating period of Λ =7.97 μm. The crystal temperature is controlled using an oven with a stability of ±0.1 °C and maximum operating temperature of 250 °C. The crystal faces are antireflection coated (R<1%) over 800−1100 nm, with high transmission (T>98%) at 532 nm. The residual reflectivity of the coating over the idler range of 1100−1400 nm is 1%−15%. For frequency selection, a 500-μm-thick uncoated fused silica etalon

(free-spectral-range, FSR=206 GHz, Finesse ∼0.6) is used at the second cavity waist between M_3 and M_4. The total optical length of the cavity including the crystal and etalon is 295 mm, corresponding to a FSR ∼1.02 GHz. The pump source is a frequency-doubled cw diode-pumped Nd:YVO_4 laser at 532 nm, as described in Section 4.2.1.

The optimum SRO operation was obtained with a relatively strong focusing parameter ξ=2, corresponding to a pump beam radius of w_{op}= 24 μm inside the crystal [45]. The signal beam waist was w_{os}= 31 μm, resulting in optimum mode-matching to the pump (b_s=b_p). To enable measurements of the idler beam, a mirror (M_5) with characteristics identical to the other cavity mirrors, but >99% reflecting at 532 nm, was used to filter out any residual pump and signal. In addition, unlike our earlier experiment with standing-wave cavities described in Section 4.2 and reported in [58], here we employed single-pass pumping, with mirrors M_1 and M_2 both ∼94% transmitting at 532 nm. Despite this, the combination of the compact ring resonator and tight focusing resulted in excellent overall SRO performance in terms of threshold, single-frequency operation at high output power and efficiency, and strong pump depletion, as we described below.

4.3.2 Results and discussions

4.3.2.1 Power scaling

In Fig. 4.7, typical behavior of cw single-frequency idler power and corresponding pump depletion as functions of pump power at the input to the crystal are shown. The data were obtained at a temperature of 82 °C, equivalent to an idler wavelength of 1187 nm (signal at 964 nm), and have been corrected for ∼20% loss due to residual reflectivity of mirrors M_2 and M_5 at the idler. Due to a transmission loss of ∼15% between the pump and the OPO, a maximum power of 8.46 W was available at

the input to the crystal. As evident from the plot, the cw SRO reaches oscillation threshold at 2.84 W of input pump power. This value is close to, and in fact lower than, the previous result for a linear cavity with double-pass pumping, as presented in Section 4.2.3.2. Moreover, the present device does not exhibit the abrupt behavior of idler power and efficiency at threshold, observed with the standing-wave cavity under double-pass pumping, attributed to the effects of thermal lensing. Here, the idler power rises smoothly from threshold and increases steadily to the maximum value of 1.55 W at 8.46 W of pump, confirming the superior performance of the ring cavity with single-pass pumping. The absence of significant thermal lensing at threshold may be attributed to the ∼50% reduction in pump intensity within the crystal under single-pass pumping compared with double-pass pumping in a linear cavity [58]. At increased pump powers, there is evidence of saturation in the idler power and pump depletion, which is broadly consistent with the theoretical predictions for a single-pass-pumped SRO, where a maximum pump depletion of 71% is predicted for a Gaussian pump beam before the onset of back-conversion [59]. However, the roll-off occurs at a pump power of ∼7.8 W, which is ∼2.75 times threshold compared with the value of 6.5 times predicted by theory.

4.3.2.2 Power across tuning range

In Fig. 4.8, the extracted single-frequency idler power and corresponding pump depletion are shown across the idler tuning range of 1140−1417 nm. The data were obtained near the peak of the idler power and the pump depletion at an input pump power of 7.8 W (Fig. 4.7). Across the entire tuning range, single-frequency operation could be maintained at the maximum power levels shown Fig. 4.8. The idler output power varied from 1.59 W at 1159 nm (70 °C) to ∼400 mW at the extreme of the tuning range near 1417 nm. However, across 52% of the total tuning

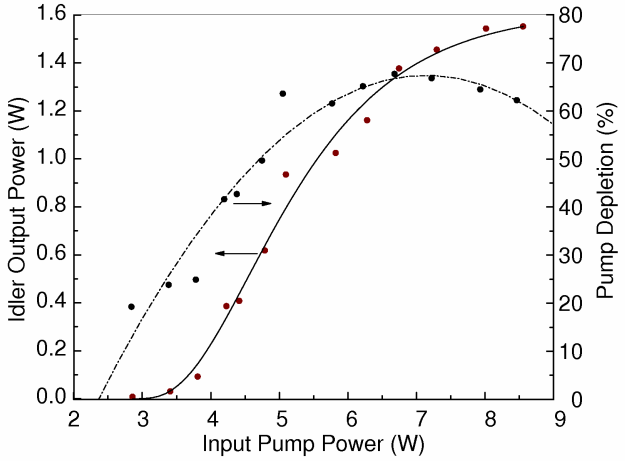

Figure 4.7: Single-frequency, cw, idler power and corresponding pump depletion as functions of pump power. The crystal temperature was fixed at 82 °C generating signal and idler of wavelengths, $\lambda_s = 0.964$ μm and $\lambda_i = 1.187$ μm respectively.

range, between 1140 and 1285 nm, single-frequency idler powers of >1 W could be obtained, with more than 400 mW available over the remainder of the tuning range. The pump depletion varied from 40% to 67% across the tuning range. The total signal and idler tuning range was 852−1417 nm, obtained by varying the crystal temperature between 61 and 236 °C. The tuning was continuous, except for a small gap over 1026−1104 nm due to the reflectivity fall-off of SRO mirrors to avoid double resonance near degeneracy.

4.3.2.3 Thermal analysis

The fall in the idler power and pump depletion towards the longer wavelengths is attributed to the increase in crystal coating losses and reduction in parametric gain further away from degeneracy. The crystal coating loss increases from 3% at the peak of idler power (1159 nm) to 16% at the 1417 nm, while the degeneracy factor accounts for a ∼5% gain reduction between the two wavelengths. Another important contribution could be thermal lensing in the MgO:sPPLT crystal, as

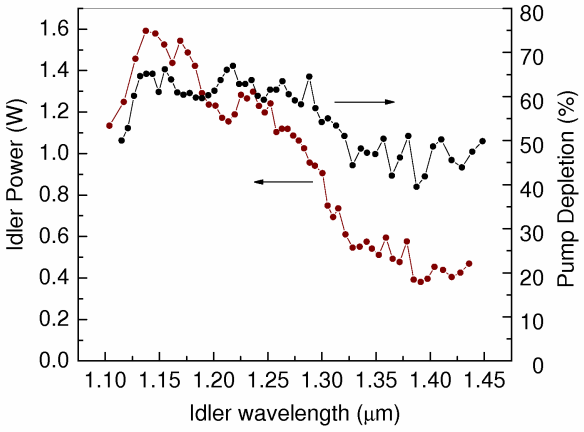

Figure 4.8: Variation of cw, single-frequency idler power and pump depletion across the idler tuning range. Input pump power was fixed at 7.8 W.

observed in our previous studies [58]. To ascertain the role of thermal lensing, we performed independent measurements of idler power with increasing pump power at different wavelengths and correspondingly different crystal temperatures. Figure 4.9 shows a comparison of cw idler power at 1254 nm (121 °C) with that at 1187 nm (82 °C) as a function of input pump power. Interestingly, the plots reveal that the cw idler power undergoes stronger saturation at the longer than at the shorter idler wavelength up to the maximum available pump power of 8.46 W. This implies that at pump powers above ∼6 W, the SRO operation is substantially more efficient at lower crystal temperatures, confirming the drop in idler output power at longer wavelengths seen in Fig. 4.8.

To further verify thermal effects as the origin of the observed behavior, we repeated the same measurements using a chopped pump beam, with the results shown in Fig. 4.10. The pump was chopped at a duty cycle of 25%. As clearly evident form the plot, there is no saturation in idler power in this case, confirming thermal effects as origin of the saturation behavior in Fig. 4.9. The remaining difference in the idler output power in Fig. 4.10 at the two different temperatures can be attributed

to the difference in crystal coating loss (∼5%) and parametric gain (1.2%) at the two idler wavelengths.

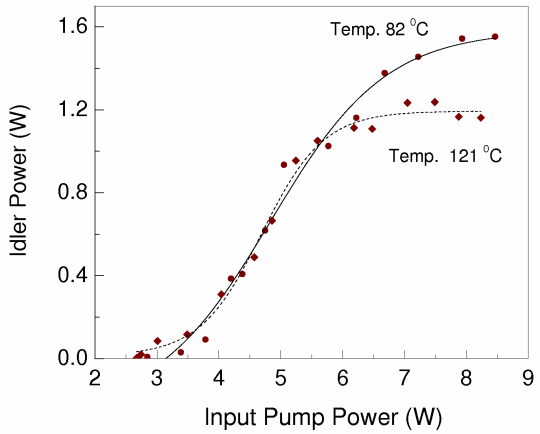

Figure 4.9: Idler output power as a function of cw pump power at two different crystal temperatures of 82 °C and 121 °C corresponding to idler wavelengths of 1187 nm and 1254 nm, respectively.

Based on a preliminary thermal lens model, we also calculated the magnitude of the thermal lens formed by the MgO:sPPLT crystal for different pump powers and temperatures. Using a measured linear absorption coefficient of 3.23% cm^{-1} for the crystal at 532 nm (Fig. 4.4), we calculated the focal length of the thermal lens at 5 W of pump power as 15.6 cm at 82 °C and 13.6 cm at 121 °C, implying stronger lensing at higher temperatures. We also find that the focal length of the thermal lens decreases with increasing pump power, again implying stronger lensing at higher powers, as expected. At 8 W of pump power, for example, the focal length of the thermal lens reduces to ∼9.4 cm at 82 °C and ∼8.5 cm at 121 °C. The formation of the thermal lens can clearly lead to degradation in mode matching between the signal and pump from the optimum conditions, resulting in the reduction in output power and efficiency. These calculations thus also confirm the role of thermal lensing in the reduction of idler power at longer wavelengths (higher temperatures), as evident

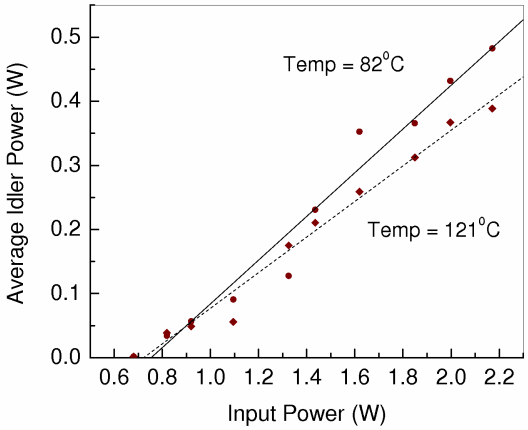

Figure 4.10: Idler output power as functions of quasi-cw pump power at two different crystal temperatures 82 °C and 121 °C corresponding to idler wavelengths of 1187 nm and 1254 nm respectively. The pump beam was chopped with a duty cycle of 25%

in Fig. 4.8, as well as the stronger saturation of the idler power in Fig. 4.9. Another contribution to thermal lensing may be the circulating signal intensity which, at the highest pump power of 8.46 W, can be >10 W. This can be verified using different levels of signal output coupling and is currently under investigation.

4.3.2.4 Single-frequency operation

We analyzed the idler output spectrum using a scanning confocal Fabry-Perot interferometer. The interferometer has a free-spectral-range of 1 GHz and Finesse of 400, corresponding to a resolution of 2.5 MHz. The crystal temperature was 82 °C, generating idler of wavelength 1187 nm. A typical fringe pattern at maximum idler power of 1.59 W is shown in Fig. 4.11, verifying single-frequency operation. The instantaneous linewidth, measured directly without accounting for the interferometer resolution, is ∼7 MHz. Similar behavior was observed at all idler wavelength and temperatures.

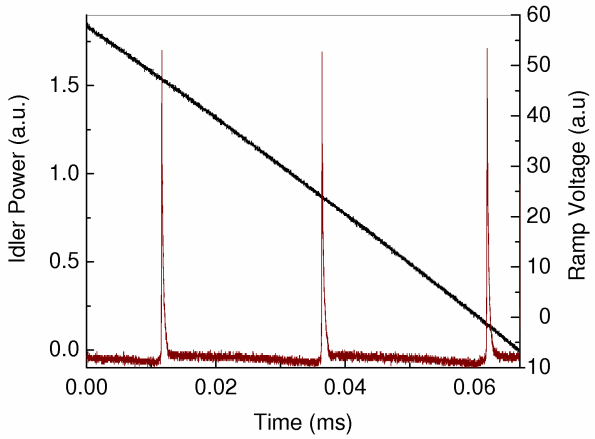

Figure 4.11: Single-frequency spectrum of the idler output recorded by a scanning Fabry-Perot interferometer. Crystal temperature is 82 °C, generating idler power of 1.59 W at 1187 nm.

4.3.2.5 Idler power stability

The SRO power stability near the maximum of the idler power at 1.59 W is shown in Fig. 4.12. Under free-running conditions and in the absence of thermal isolation,

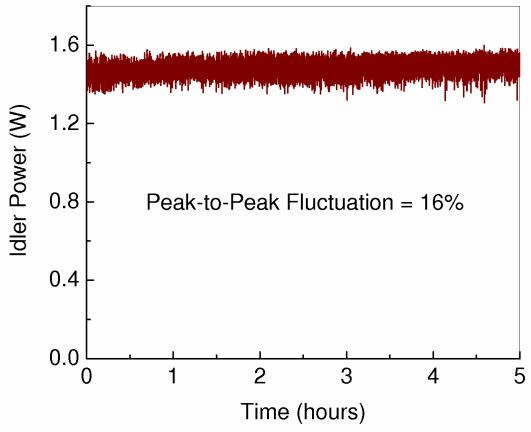

Figure 4.12: Output power stability of idler at 1187 nm near 1.59 W over 5 hours.

the idler power exhibits a peak-to-peak stability of 16% over 5 hours. This power fluctuation is attributed mainly to the change in the laboratory environment. With

improved thermal isolation and active control, further improvements in the SRO output stability are expected.

4.4 Conclusions

In this Chapter, a high-power, widely tunable, cw source in the near-IR has been demonstrated. Pumping in the green, the SRO based on MgO:sPPLT nonlinear crystal in a linear cavity configuration can provide continuously tunable output across 848−1430 nm. Using a 30-mm-long crystal and double-pass pumping, an oscillation threshold of 2.88 W has been obtained, and single-pass idler powers in excess of 1.51 W have been generated over 1104−1430 nm for 6 W of pump power at an extraction efficiency of 25.2% and photon conversion efficiency of 56.7%.

For single-frequency operation of the cw SRO across 848−1430 nm, we have used a compact ring cavity configuration. Using the same MgO:sPPLT crystal, the SRO oscillation threshold of 2.84 W has been obtained, and a single-pass idler powers in excess of 1.59 W have been generated over 1104−1430 with a maximum extraction efficiency of the SRO of 25.2% and pump depletions of as much as 67%. The single-frequency idler output has a linewidth of ∼7 MHz. Under free-running conditions and in the absence of thermal isolation, the idler power exhibits a peak-to-peak stability of 16% over 5 hours. The idler power fluctuation is attributed mainly to the changes in the laboratory environment and the thermal instability of the oven. With thermal isolation of the system from laboratory environment along with improved temperature controlled oven, further improvements in SRO output stability are expected. With the active frequency stabilization we can perform fine frequency tuning of the SRO, making the SRO an useful source for different applications including spectroscopy and trace gas sensing.

Although the the SRO can be tuned across the wavelength range 848−1430 nm, the practical output power is available over the wavelength range of 1104−1430 nm due to the high reflectivity of the cavity mirrors for the signal radiation in the wavelength range 848−1030 nm. With the use of proper output coupling in the signal, we could extract substantial power throughout the entire tuning range of the SRO. Besides, the thermal effects due to the absorption of the high signal power resonating inside the cavity can be overcome by reducing the resonating signal using output coupling, with little sacrifice of oscillation threshold.

Chapter 5

Resonant wave coupling in cw SRO

This Chapter constitutes the following journal publication:

1. *Continuous-wave singly-resonant optical parametric oscillator with resonant wave coupling*
   G. K. Samanta, and M. Ebrahim-Zadeh
   Optics Express 16, 6883–6888 (2008).

5.1 Motivation

Continuous-wave (cw), optical parametric oscillators (OPOs) represent versatile sources of tunable, single-frequency radiation in the spectral regions inaccessible to the lasers. Before the development of quasi-phase-matched (QPM) nonlinear materials, operation of cw OPOs in the singly-resonant oscillator (SRO) configuration was difficult due to the high oscillation thresholds (typically several watts) in birefringent crystals [6]. The advent of periodically-poled materials, in particular PPLN, heralded major breakthroughs in the cw OPO technology, bringing the operation threshold of SROs within the reach of moderate to high-power laser pump sources [7]. Due to their high-power (watt-level), single-frequency performance, and simplified fine tuning capability, such cw SROs have since been successfully deployed in

applications such as photoacoustic spectroscopy [8].

At the same time, due to the persistently high pump thresholds (still several watts in QPM materials), the common approach to the development of cw SROs has been to deploy an optical cavity with the lowest loss at the resonant signal wave to minimize threshold, while providing maximum output coupling for the non-resonant idler wave in order to achieve the highest power extraction. In PPLN, with a large effective nonlinearity (d_{eff} ~17 pm/V) and long interaction lengths (50-80 mm), this condition can be somewhat relaxed and finite signal output coupling can be tolerated [7; 9; 60]. However, in other QPM materials any small increase in resonant wave coupling is expected to lead to an unacceptable rise in threshold, rendering SRO operation inefficient or beyond the reach of commonly available cw laser sources.

In this Chapter, we present the operation of a green-pumped cw SRO based on MgO:sPPLT under finite out-coupling of the resonating signal. We have characterized two experimental configurations; SRO and out-coupled SRO (OC-SRO). Finite signal output coupling shows that major enhancements in the overall performance of the SRO with regard to output power, extraction efficiency, and useful tuning range can be brought about at little or no cost to threshold, internal conversion efficiency (pump depletion), idler output power, and idler extraction efficiency. We also present the spectral characterization of the signal and idler output and observe thermal effects in the MgO:sPPLT crystal induced by the absorption of the pump as well as the resonant signal wave.

5.2 Experimental configuration

The experimental configuration of the OC-SRO is identical to that described in Chapter 4, except for the replacement of mirror M_4 (high reflector at the signal) with an output coupler, as shown in Fig. 5.1. The OPO is formed in a ring cavity using two concave mirrors, M_1, and M_2 (radius of curvature, r=50 mm) and two plane mirrors M_3 and M_4. In SRO arrangement (see Fig. 5.2), all the mirrors have high reflectivity (R>99.5%) for the resonant signal over 840−1000 nm.

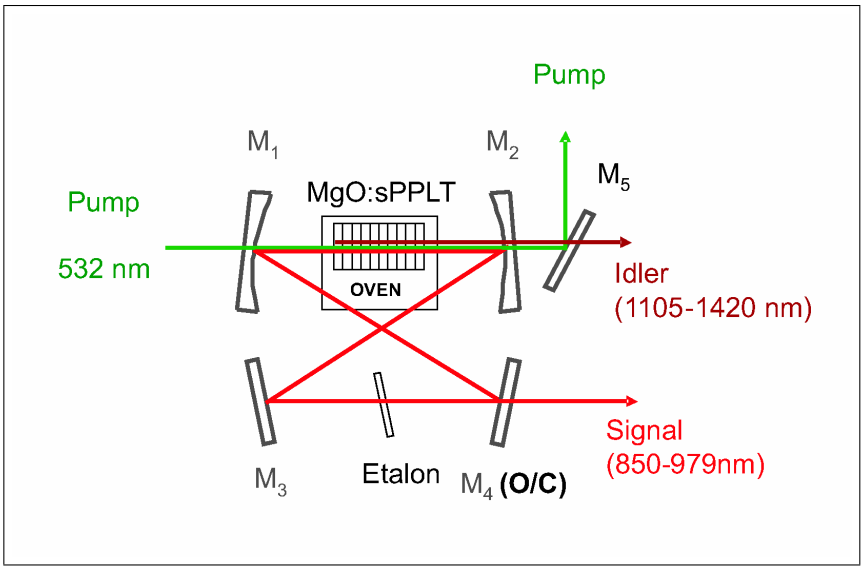

Figure 5.1: Schematic of the experimental design for the MgO:sPPLT cw OC-SRO in a compact ring cavity. Mirrors $M_{1,2,3}$ are high reflecting (> 99.9%) at signal wavelength and mirror M_4 has finite coupling 0.71%-1.1% at signal wavelength.

In the OC-SRO configuration, one of the plane high reflectors is replaced by an output coupler with varying transmission (T=0.71%-1.1%) across the signal wavelength range. All the mirrors have high transmission (T=85−90%) for the idler over 1100−1400 nm, thus ensuring SRO operation in both configurations. The nonlinear crystal is MgO:sPPLT (d_{eff} ∼10 pm/V). It is 30-mm-long, contains a single grating period of Λ=7.97 μm, and is housed in an oven with a temperature stability of ± 0.1 °C. The crystal faces have antireflection (AR) coating (R<0.5%) for the

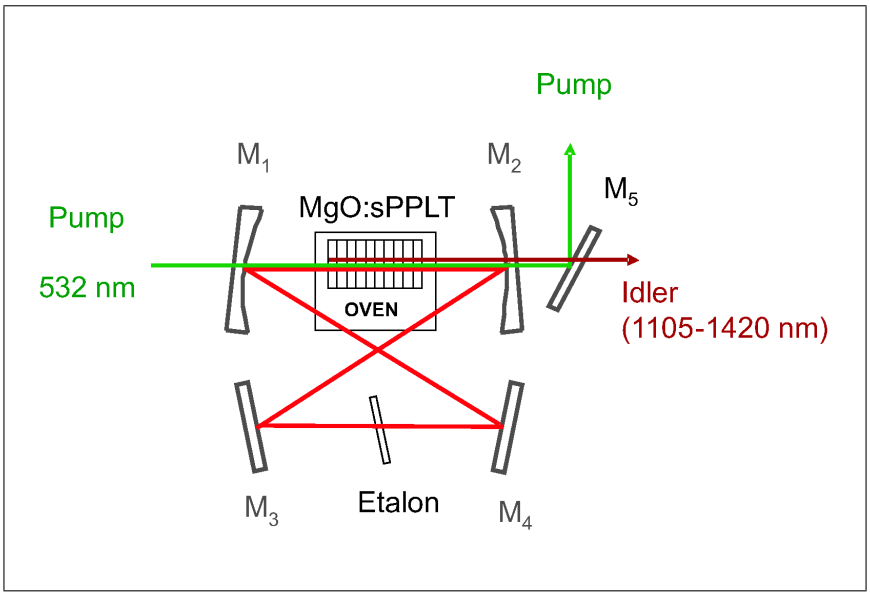

Figure 5.2: Schematic of the experimental design for the MgO:sPPLT cw SRO. The compact ring cavity of the SRO is same as Fig. 5.1 except mirror M_4 is replaced with a high reflector at signal wavelength.

signal (800−1100 nm), with high transmission (T>98%) at 532 nm. The residual reflectivity of the coating is 0.6% to 4% per face for the idler (1100−1400 nm). A 500-μm-thick uncoated fused silica etalon (FSR=206 GHz, finesse$\sim$0.6) is used at the second cavity waist for frequency selection. The pump source is a frequency-doubled, single-frequency cw Nd:YVO_4 laser at 532 nm, as described in Section 4.2.1. In order to directly compare the performance of the cw OPO in SRO and OC-SRO configurations, we used identical operating conditions in both cases using the same focusing and mode-matching parameters for the pump and the resonant signal. We used a fairly strong focusing parameter of ξ=2, corresponding to a pump beam radius of $w_{op} \sim 24$ μm inside the crystal. The signal beam waist was $w_{os} \sim 31$ μm, resulting in optimum mode-matching to pump ($b_p = b_s$, Equation (4.2)). We performed measurements of the idler and the signal output power, extraction efficiency, pump depletion, photon conversion efficiency, oscillation threshold, and

spectral characteristics in both the configurations.

5.3 Results and discussions

5.3.1 Power scaling of SRO and OC-SRO

Figure 5.3 shows the idler and signal output power and the corresponding pump depletion for the SRO with minimal signal coupling versus pump power at the input to the crystal. The idler powers correspond to the output through the second concave mirror, M_2, after filtering the pump, whereas the signal powers correspond to the usable output through one of the plane high reflectors. The measurements were preformed at a crystal temperature of 80 °C (signal=966 nm, idler=1184 nm) near the maximum of the idler output power, where the effects of thermal lensing, crystal coating loss, and gain reduction due to degeneracy factor are minimized, as explained in Chapter 4.

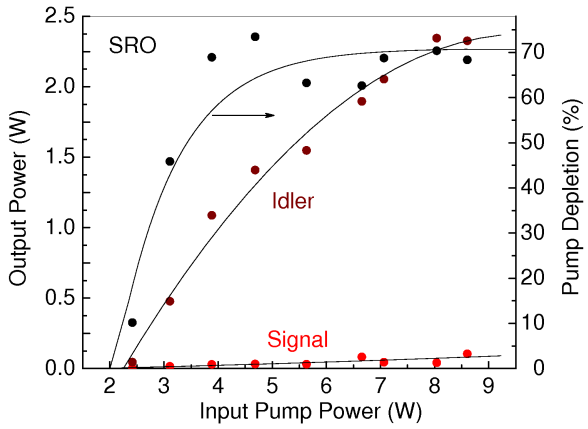

Figure 5.3: Extracted signal power, idler output power, and pump depletion as functions of pump power in SRO. The solid curves are guide for the eye. Crystal temperature is 80 °C corresponding to a signal and idler wavelength 966 nm and 1186 nm, respectively.

The idler power reaches a maximum power of 2.33 W at 8.6 W of pump, cor-

responding to an extraction efficiency of 27.1%. The usable signal power, however, remains limited for all pump powers, as expected for a SRO with minimum signal coupling. It reaches to a maximum value of 104 mW at 8.6 W of pump, resulting in a useful extraction efficiency of 1.2%. The maximum total extraction efficiency of the SRO is thus 28.3% and threshold is reached at 2.41 W of pump power. The SRO pump depletion rises rapidly reaches a maximum of 73% at 4.68 W of pump before the onset of saturation. This effect, which has also been observed in our previous studies presented in Chapter 4, is attributed to the onset of back-conversion and is qualitatively consistent with theory [59].

Figure 5.4 represents the same plots as in Fig. 5.3, but for the OC-SRO with finite signal coupling, where one of the plane high reflectors, M_4 is replaced by an output coupler. The signal powers correspond to the usable output through the output coupler, which has a transmission of 0.98% at 966 nm. The idler power in this case reaches a maximum of 2.53 W at 8.83 W of pump, corresponding to an extraction efficiency of 28.6%, which is comparable to the 28.3% for the SRO in Fig. 5.3. However, the usable signal power simultaneously generated now reaches 945 mW at 8.83 W of pump, representing an extraction efficiency of 10.7%. The maximum total output power is now 3.48 W and the total extraction efficiency is thus 39.3%, representing an overall enhancement in the extraction efficiency of 11% from the SRO. The pump depletion now reaches a maximum of $\sim$70% at 6.6 W of pump before saturation takes effect. The pump power threshold for the OC-SRO is now $\sim$2.99 W, representing an increase of only 24% (580 mW) over the SRO. It is thus clear that while the OC-SRO exhibits an insignificant increase in pump power threshold, it provides substantial enhancements in usable signal and idler power and total extraction efficiency. At the same time, the OC-SRO maintains similar idler power, idler extraction efficiency, and pump depletion as the SRO.

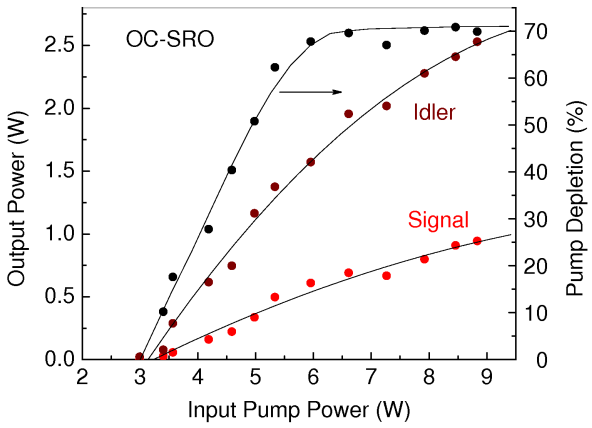

Figure 5.4: Extracted signal power, idler output power, and pump depletion as functions of the pump power in OC-SRO. The solid curves are guide for the eye. Crystal temperature is 80 °C corresponding to a signal and idler wavelength of 966 nm and 1186 nm, respectively.

5.3.2 Power across tuning range of SRO and OC-SRO

We also recorded the extracted signal and idler output power and the corresponding pump depletions across the tuning range for both the SRO and OC-SRO. The results for the SRO are shown in Fig. 5.5. The data were obtained for a change in crystal temperature from 71 °C to 245 °C and were recorded near the peak of the signal and idler powers in Figs. 5.3 and Fig. 5.4. In the SRO, the idler power varies from 2.46 W at 1167 nm (T=71 °C) to 487 mW at 1427 nm (T=245 °C). The signal power leakage through one of the plane high reflectors (M_4), however, remains below 56 mW across most of the signal tuning range from 978 nm to 866 nm, before rising to 195 mW at 848 nm due to increase in signal transmission of the plane high reflector. The pump depletion remains close to ∼70% over much of the tuning range, decreasing to ∼40% towards the extremes of the tuning range at 1427 nm (idler) and 848 nm (signal). The maximum combined power and total extraction efficiency across the tuning range are 2.52 W and 30%, respectively, at 1190 nm (idler) and 962 nm (signal) at 83 °C. The decline in idler power and pump depletion towards the extreme of the

tuning range is consistent with the SRO behavior described in Chapter 4, attributed to the increased effects of thermal lensing at higher temperatures (longer idler, shorter signal wavelengths), crystal coating losses, and parametric gain reduction away from degeneracy.

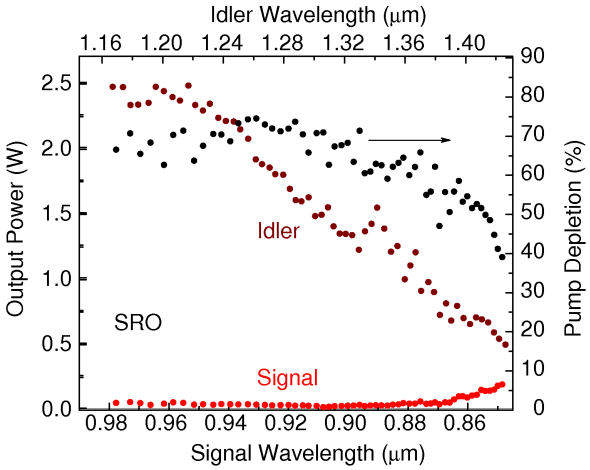

Figure 5.5: Extracted signal power, idler output power, and pump depletion across the tuning range for SRO.

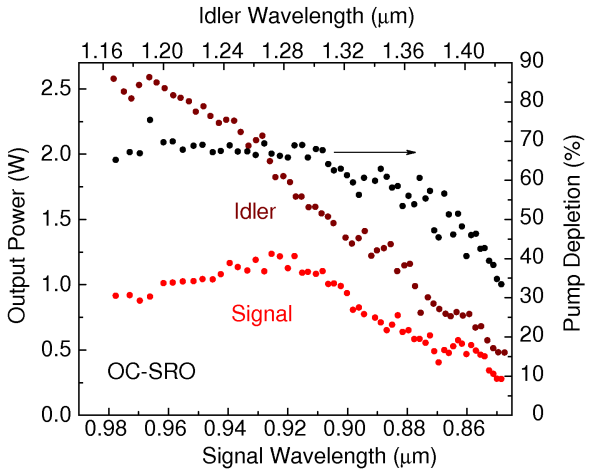

Figure 5.6: Extracted signal power, idler output power, and pump depletion across the tuning range for OC-SRO.

The same plots as in Fig. 5.5, but for the OC-SRO with finite signal coupling is shown in Fig. 5.6. In this case, the idler power varies from 2.57 W at 1167 nm

to 2.59 W at 1190 nm, to 480 mW at 1427 nm, with the pump depletion again remaining close to ∼70% over most of the tuning range before declining to ∼35% at the extreme of the tuning range. Thus, despite the increased signal coupling, the idler power and pump depletion in OC-SRO remain similar to the SRO in Fig. 5.5. Importantly, however, the OC-SRO can now provide substantial signal powers of up to 1.23 W across the tuning range. The signal output varies from 915 mW at 978 nm to 1.23 W at 925 nm, to 278 mW at 848 nm. The maximum total output power and extraction efficiency across the tuning range are now 3.6 W and 40%, respectively, at 1190 nm (idler) and 962 nm (signal) at 83 °C, representing a 1.08 W increase in the output power and 10% in the extraction efficiency. Notwithstanding the expected decline in the signal power towards shorter wavelengths, as seen in Chapter 4, the variation in the extracted signal power closely follows the output coupler transmission across the tuning range, as shown in Fig. 5.7. An improved coating for the output coupler with an optimum and constant coupling across the tuning range can, therefore, provide a signal power >1 W over the entire signal wavelength range. From the curve, the optimum value of output coupling in the present device is 1.04% at 925 nm.

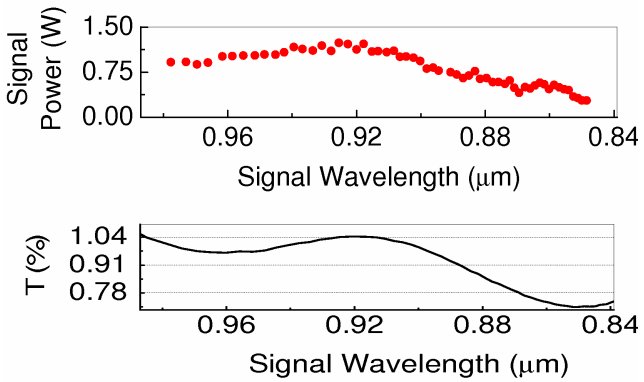

Figure 5.7: Signal power and the corresponding output coupler transmission over the signal tuning range.

It is, therefore, clear that the OC-SRO can provide substantial enhancements in the usable signal power by as much as 1.23 W, in total output power by as much as 1.08 W, and in total extraction efficiency by as much as 10% compared to the SRO. The scheme also effectively expands the useful tuning range of the device by 130 nm into the 848−978 nm signal region. Moreover, the improvement in performance is obtained at little or no expense to idler power or pump depletion across the tuning range.

5.3.3 Spectral characteristics of cw OC-SRO

We performed spectral characterization of the cw OC-SRO signal and idler output using a confocal Fabry-Perot interferometer [61; 62] (FSR=1 GHz, finesse=400 at both wavelengths). The measurements were performed near the maximum of the signal and idler power as shown in Fig. 5.3 and Fig. 5.4 at 966 nm and 1184 nm, respectively. We observed reliable single-frequency operation at both the signal and idler, but we found that the signal exhibited a substantially narrower linewidth than the idler. For measurements of linewidth, we recorded the fringe pattern for the signal and idler at different instants of time, and deduced the corresponding FWHM linewidths.

Typical transmission fringes are shown in Fig. 5.8 for the signal and in Fig. 5.9 for the idler. The calculated linewidths over three measurements are also shown in Table 5.1, where a linewidth of ∼3 MHz can be deduced for the resonant signal. The corresponding idler exhibits a linewidth ∼7 MHz, consistent with our previous observations, confirming a substantially narrower linewidth for the resonant signal than the non-resonant idler. This result is not unexpected, since the resonance of the signal wave leads to spectral confinement by the high finesse of the optical cavity. On the other hand, the non-resonant idler spectrum can more freely adjust to

satisfy the energy conservation condition, thus resulting in broader bandwidth. This property can have useful implications for the utility of OC-SROs in spectroscopic applications. It suggests that by choosing the spectroscopic wavelength of interest as the resonant wave rather than the non-resonant wave, it would be possible to enhance the measurement resolution, while still providing substantial output powers.

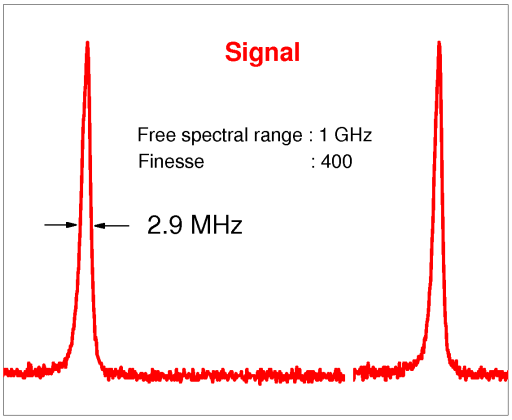

Figure 5.8: Fabry-Perot transmission fringes for signal at a crystal temperature 80 °C.

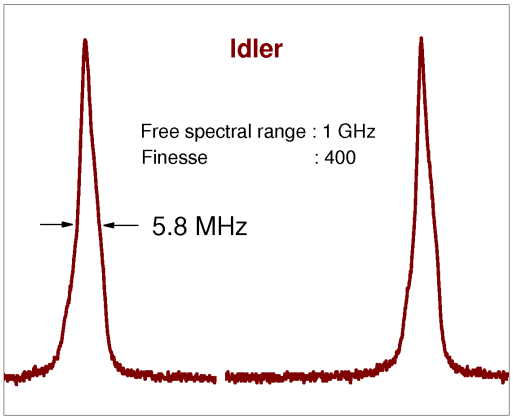

Figure 5.9: Fabry-Perot transmission fringes for idler at a crystal temperature 80 °C.

Table 5.1: Measured linewidth (FWHM) of signal and idler.

Measurement No.	Signal Wave (MHz)	Idler Wave (MHz)
1.	3.1	7.0
2.	3.3	6.4
3.	2.9	5.8

5.3.4 Thermal effect in cw OC-SRO

Investigation of the cw OC-SRO output also revealed significant shift in output wavelength as a function of pump power. This effect, which arises from the heating of the crystal, has been previously observed in PPLN under strong pumping [60] and attributed to the intracavity signal absorption. Here we find that, unlike in PPLN, absorption of pump in the MgO:sPPLT sample also plays an important role in the crystal heating, and thus the output wavelength shift. At a nominal (oven) temperature of 80 °C, we measured the signal wavelength using a wavemeter (Burleigh, WA-1000, resolution 0.001 nm) as a function of pump power. At the maximum pump power of 9.1 W, we recorded a signal wavelength of 966.4 nm, while at a pump power of 4.8 W, a wavelength of 972.9 nm was measured. Using the data, calculations of phase-matching based on Sellmeier equations for stoichiometric $LiTaO_3$ [52] resulted in a crystal temperature of 84.7 °C at 9.1 W of pump and 80.7 °C at 4.8 W of pump, implying a rise of 4 °C in crystal temperature with increased pump power, as shown in Fig. 5.10.

In order to separate the contributions of the pump and intracavity signal, at the full pump power of 9.1 W, we rotated the pump polarization away from phase-matching until the OC-SRO was just above threshold. Under this condition, we

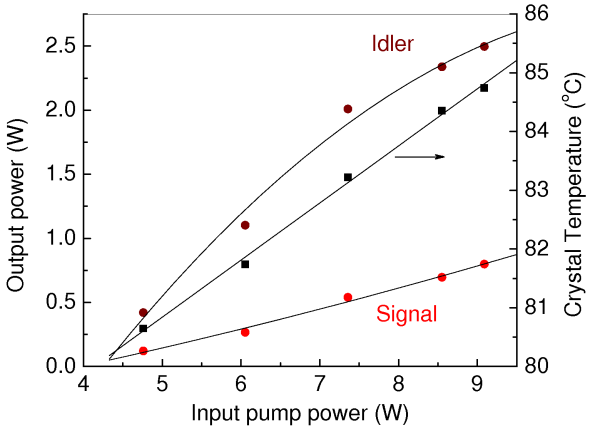

Figure 5.10: Variation of crystal temperature with the increase of pump power and intracavity signal power.

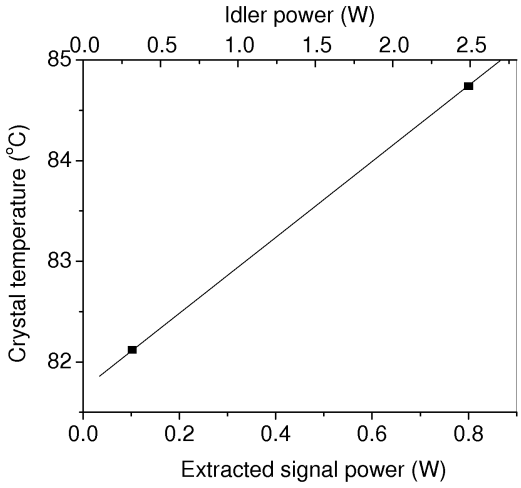

Figure 5.11: Variation of crystal temperature with the increase of intracavity signal power at fixed pump power. Pump power is 9.08 W.

recorded a signal wavelength of 970.5 nm corresponding to a crystal temperature of 82.1 °C as shown in Fig. 5.11, indicating a still significant rise despite negligible circulating signal power, and thus confirming the contribution of the pump to crystal absorption and heating. Other possible contributions to crystal heating may be green-induced infrared or idler absorption. However, the contribution of green-induced infrared absorption is expected to be low in MgO:sPPLT [63], and the contribution due to the absorption of the single-pass idler is also expected to be negligible.

5.4 Conclusions

In this Chapter, we have demonstrated that by deploying finite output coupling of the resonant wave in a cw SRO, it is possible to enhance the overall output power, extraction efficiency, useful tuning range and spectral purity with little or no sacrifice to threshold, idler power, or pump depletion. We have also observed improved spectral purity of the resonant signal compared with the non-resonant idler, implying the advantage of exploiting the resonant out-coupled wave for spectroscopic applications. Measurements of crystal heating effects have also confirmed significant contribution of the pump as well as intracvity signal absorption to output wavelength shift with increasing pump powers. The OC-SRO configuration could also offer additional advantages over the SRO. In near-degenerate operation, for example, it could provide improved output power in a single beam with a finite spectrum, which could be useful for cascaded pumping of mid-infrared OPOs or in applications were high-power and broadband cw sources are simultaneously required.

Chapter 6

Tunable, cw, solid-state source for the blue radiation

This Chapter constitutes the following journal publication:

1. *Continuous-wave, single-frequency, solid-state blue source for the 425−489 nm spectral range*
   G. K. Samanta, and M. Ebrahim-Zadeh
   Optics Letters 33, 1228–1230 (2008).

6.1 Motivation

Continuous-wave (cw), solid-state coherent sources in the blue are of practical interest for applications in optical data storage, laser displays, spectroscopy, medical diagnostics and underwater communication. While cw diode lasers in the blue are available, output power, beam quality, and extended wavelength coverage still remain important limitations. Other well-established techniques, including second harmonic generation (SHG) of near-infrared laser diodes [64] or the short-wavelength transitions in, for example, Nd:YAG [65] and Nd:YVO_4 [66] can provide practical cw powers in the blue, but similarly offer little or no tunability. Frequency doubling of the Ti:sapphire can in principle provide tunable coverage in the 400−500 nm range, but at increased cost and complexity, while similar approaches based on alternative

diode-pumped vibronic gain media such as Cr:LiSAF have achieved limited power in the blue over a confined tuning range (427−443 nm) [67]. At the same time, all the described techniques suffer from the common drawback that the attainable spectral range in the blue is ultimately constrained by the tunability of the fundamental input lasers, making the 400−500 nm range the current practical limit.

In this Chapter, we describe a new approach to the generation of cw radiation in the blue, which offers the advantages of wide tuning range, practical output power, single-frequency performance, and simple, compact, solid-state design. The approach is based on intra-cavity SHG of a green-pumped, cw, singly-resonant optical parametric oscillator (SRO) with MgO:sPPLT as the nonlinear crystal, as described in Chapters 4 and 5. Our group has recently used this technique to produce femtosecond pulses in the ultraviolet [5]. Here, we extend this approach to the cw regime to generate up to 1.27 W of cw, single-frequency blue radiation across 425−489 nm. Our approach also offers an important inherent advantage over alternative methods by permitting flexible wavelength coverage beyond the current limits through suitable choice of grating period in the MgO:sPPLT crystal. In addition to the single-frequency blue output, the SRO generates in excess of ∼100 mW of single-mode signal radiation across 850−978 nm and up to 2.6 W of idler in the wavelength range of 1167−1422 nm.

This Chapter consists with two main sections; Generation of tunable cw blue radiation; and high-power, cw, stable, single-frequency blue generation. Section 6.2 presents the first experimental demonstration of tunable blue cw SRO, and Section 6.3 demonstrates simultaneous single-frequency operation and high-power performance of the blue cw SRO.

6.2 Generation of tunable cw blue radiation

6.2.1 Experimental configuration

The experimental configuration of the cw SRO (Fig. 6.1) is similar to that described in Chapters 4 and 5. The cavity is formed in a ring resonator, comprising two concave reflectors, M_1 and M_2 (radius of curvature, r=50 mm), and two plane mirrors, M_3 and M_4. Limited by physical constraints, the angle of incidence on M_1 and M_2 is kept <7.5° to minimize astigmatism. The mirrors M_1, M_2 and M_3 are all highly reflecting (R>99.9%) for the resonant signal (840−1000 nm). Mirror M_4 also has high reflectivity for the signal (R>99% over 850−920 nm, R>99.9% over 920−1000 nm) and high transmission (T=85−90%) over 425−500 nm. All mirrors are also highly transmitting (T=85−90%) for the idler (1100−1400 nm), thus ensuring SRO operation. The nonlinear crystal is MgO:sPPLT (d_{eff} ∼10 pm/V). It is 30-mm-long, contains a single grating (Λ=7.97 μm), and is housed in an oven with a temperature stability of ± 0.1 °C. The crystal faces have antireflection (AR) coating (R<0.5%) for the signal (840−1000 nm), with high transmission (T>98%) for the pump at 532 nm. The residual reflectivity of the coating is 0.6% to 4% per face for the idler (1100−1400 nm). The pump sources is a frequency-doubled, cw, single-frequency Nd:YVO_4 laser, as described previously in Section 4.3 and Section 5.2.

Photograph of the real time cw blue SRO system working in the laboratory is shown in Fig. 6.2. The resonator mirrors and nonlinear crystals are marked in accordance with the schematic of the experimental configuration as shown in Fig. 6.1.

For internal SHG, we used BiB_3O_6 (BIBO), as the nonlinear crystal due to its high nonlinear coefficient and low spatial walkoff [68; 69]. The crystal is 5 mm in length and 4 mm × 8 mm in aperture. It is cut for type-I phase-matching ($ee \rightarrow$

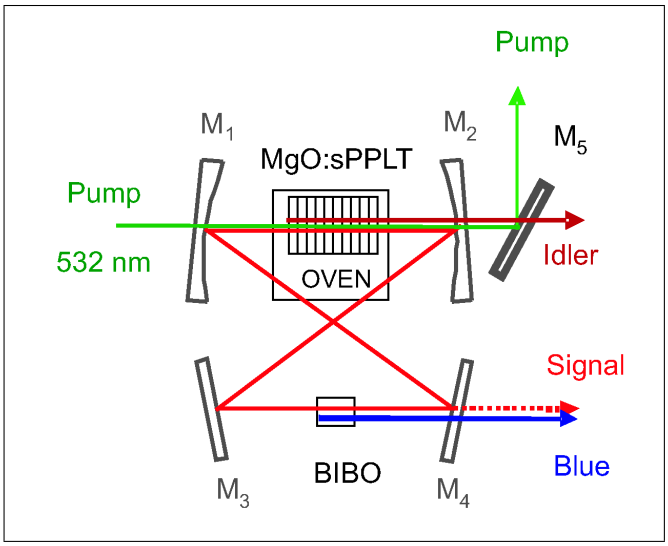

Figure 6.1: Schematic diagram of the intrcavity frequency-doubled MgO:sPPLT cw SRO for blue generation.

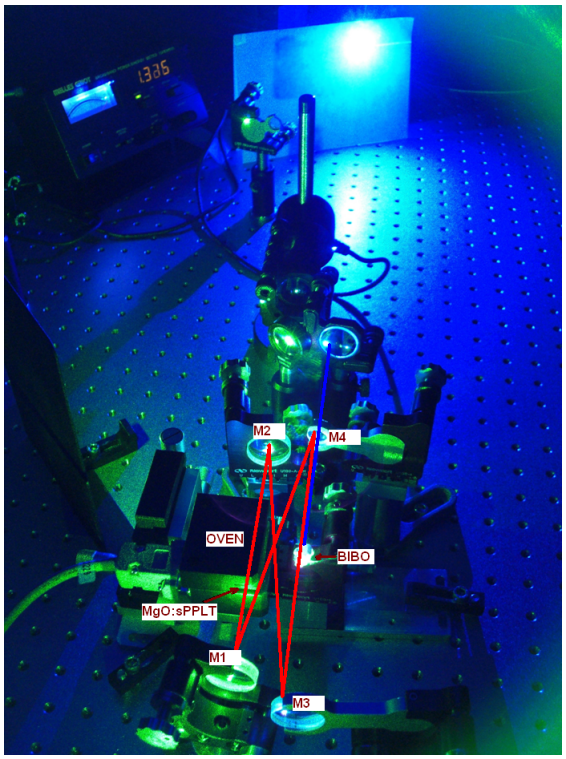

Figure 6.2: Picture of the cw, blue SRO working in our laboratory.

o) in the optical *yz*-plane (ϕ=90°) at an internal angle θ=160° at normal incidence (d_{eff} > 3.4 pm/V), corresponding to a fundamental wavelength of ∼920 nm. The crystal end-faces are AR-coated for the resonant signal (R<0.5% over 850−1000 nm) and the SHG wavelengths (R<0.8% over 425−500 nm). For the SRO, we use a relatively strong pump focusing parameter, ξ_{SRO} = 2, corresponding to a pump beam radius of w_{op}=24 μm inside the MgO:sPPLT crystal. The signal beam waist is w_{os} ∼31 μm, resulting in optimum mode-matching to pump (b_p=b_s). The BIBO crystal is located at the second cavity focus between M_3 and M_4. The signal waist at the centre of the crystal is ∼160 μm, corresponding to a focusing parameter ξ_{SH} ∼0.015. Such loose focusing was used to ensure an effective interaction length in BIBO, limited by spatial walkoff, equal to or longer than the crystal length. The total optical length of the cavity including both crystals is 298 mm, corresponding to *FSR* ∼1.01 GHz. Unlike our previous work in Section 4.3 and Section 5.2, the SRO cavity here does not include an intracavity etalon.

6.2.2 Results and discussions

6.2.2.1 Tuning of the intracavity frequency-doubled cw SRO

Figure 6.3 shows the SRO tuning range in the signal and idler and the generated blue wavelength as a function of crystal temperature. The wavelengths were measured using a wavemeter (Burleigh, WA-1000) with a resolution of 1 pm. The SRO could be continuously tuned over 978−850 nm in the signal and 1167−1422 nm in the idler by varying the crystal temperature from 71 °C to 240 °C. Thus, the tuning was continuous over 850−1422 nm, except for a gap near degeneracy (978−1167 nm) due to the reflectivity fall of the SRO mirrors to prevent doubly-resonant oscillation. The limit to SRO tuning at the extremes of the signal and idler range was set by the maximum operating temperature of the oven at 240 °C. The corresponding SHG

wavelengths from 489 to 425 nm are generated by varying the internal angle of the BIBO crystal from 163.8° to 155.2°.

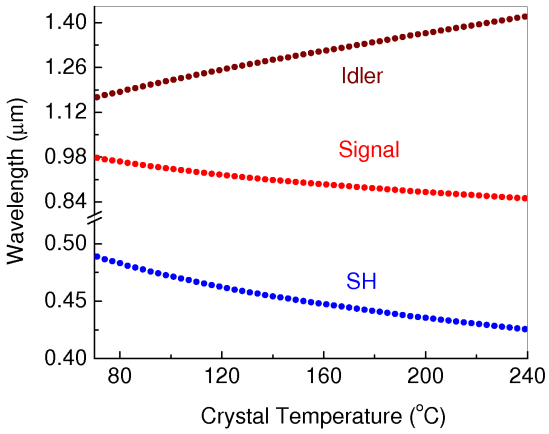

Figure 6.3: Wavelength tuning range of the green-pumped cw SRO and the corresponding frequency-doubled blue output as functions of crystal temperature for a grating period of 7.97 μm.

6.2.2.2 Power across the tuning range

We recorded the blue power near the maximum of idler power for each crystal temperature by optimizing the input pump power before the onset of saturation, as described in Chapter 4. Figure 6.4(a) shows the extracted blue power across the tuning range. The measured power varies from 45 mW at 425 nm to 300 mW at 489 nm, with as much 448 mW available at 459 nm. We extracted >300 mW of blue power over 53% of the tuning range and >100 mW over 90% of the tuning range. The sudden fall in the blue power near 450 nm is due to the rise in signal coupling loss through mirror M_4, Fig. 6.4(b), which results in reduced intracavity signal power and thus lower SHG conversion efficiency, although there was no significant reduction in the idler power, Fig. 6.4(c). As the SRO is operating near saturation, a reduction in intracavity signal power does not have a significant impact on the idler output power.

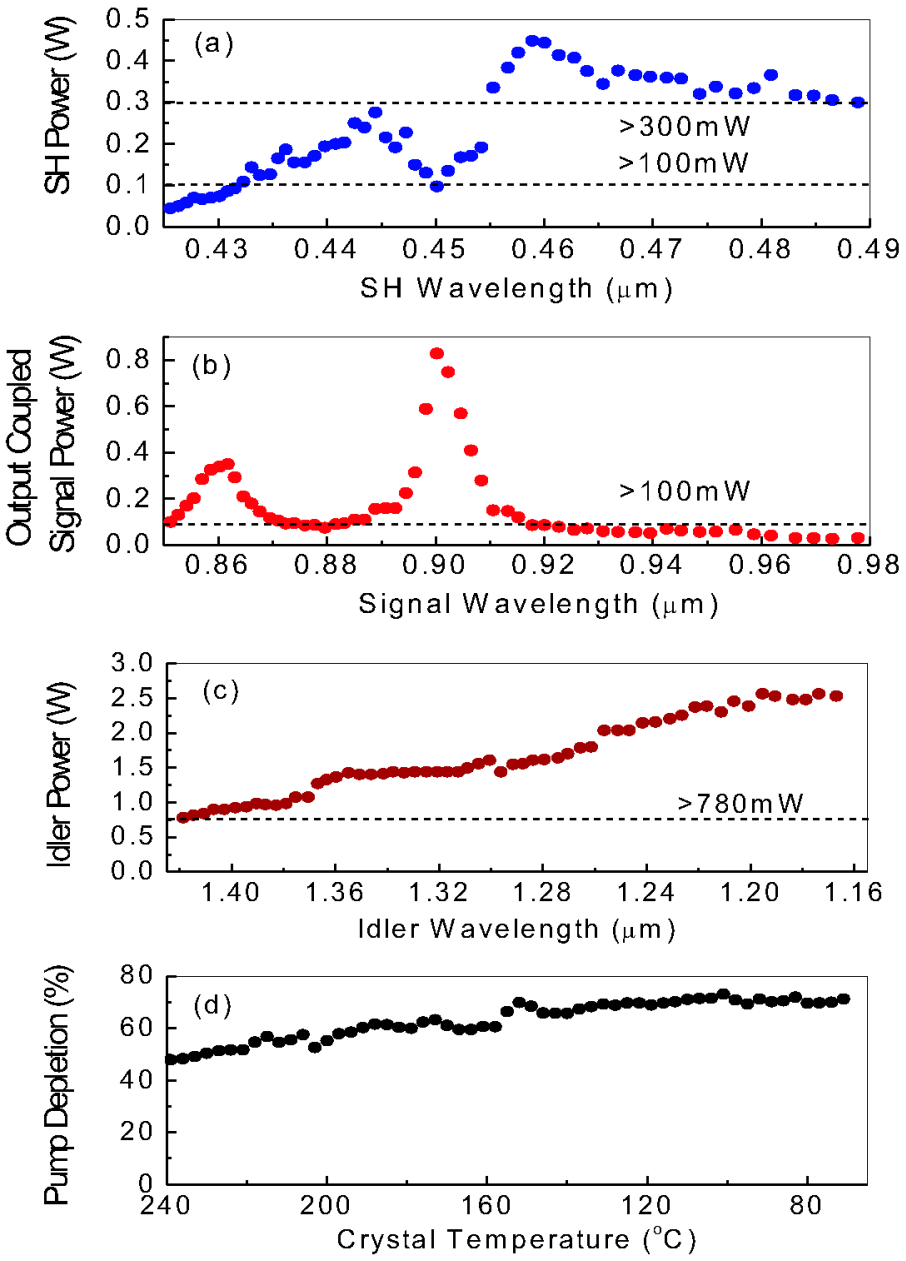

Figure 6.4: (a) Second-harmonic blue power, (b) out-coupled signal power, (c) single-pass idler power, and (d) corresponding pump depletion across the tuning range.

As such, the use of a more optimized coating for M_4 with minimum transmission loss across the signal tuning range will readily overcome the dip in SH power. The overall decline in the blue power towards the shorter wavelengths is, however, attributed to the reduction in intracavity signal power due to the increased effects of thermal lensing near the extremes of the SRO tuning range (higher temperatures), higher MgO:sPPLT crystal coating losses, and parametric gain reduction away from degeneracy, as observed previously in the earlier Chapters 4 and 5. The reduction of the intracavity signal power is also evident from the fall in idler power towards the extreme of the tuning curve, Fig. 6.4(c). From the transmission data of the mirror M_4, and the out-coupled signal power, Fig. 6.4(b), we calculate that intracavity signal power to vary from ∼170 W at 978 nm to ∼35 W at 850 nm, representing a maximum single-pass SHG efficiency of 0.29%. As evident in Fig. 6.4(b), there is also >100 mW of useful signal output available over 850−915 nm (50% of total signal tuning range), with 830 mW extracted at 900 nm. In addition to the blue and signal, the SRO simultaneously generates substantial levels of non-resonant idler power of more than 780 mW, with as much as 2.6 W across the 1167−1422 nm tuning range, as shown in Fig. 6.4(c). Figure 6.4(d) shows the pump depletion across the tuning range. The measured pump depletion remains constant around 70% over 50% of the tuning range and drops to ∼48% towards the extreme of the tuning range, a similar behavior as described in Chapters 4 and 5.

6.2.2.3 Power scaling of the blue radiation

We investigated the operation threshold and power scalability of the SRO near the maximum available SHG power (at 460 nm), with the results shown in Fig. 6.5. At the maximum input pump power of 8.9 W, we obtained 432 mW of blue, 97 mW of out-coupled signal, and ∼1.98 W of idler power, with a corresponding pump

depletion of ∼73%. The SHG power exhibits a nearly linear rise with the input pump power. The pump power threshold for the frequency-doubled SRO is 4 W (2.4 W without the BIBO crystal). The rise in threshold is due to the reflection loss of the BIBO crystal faces at the signal wavelength. To gain further insight into the SHG process, we recorded the blue power as function of the out-coupled signal power by varying the input pump power, with the results shown in Fig. 6.6. As expected, the increase in SHG power with out-coupled signal power is seen to be quadratic, also implying quadratic variation with the intracavity signal power. The inset of the Fig. 6.6 also confirms the linear variation in SHG power with the square of the out-coupled signal power, as expected. Using the linear slope efficiency one can in principle calculate the effective nonlinear coefficient (d_{eff}) of BIBO crystal, but the accuracy depends upon the estimate of the signal power inside the SRO, which in tern depends on the exact value of the coupling coefficient of the mirror M_4.

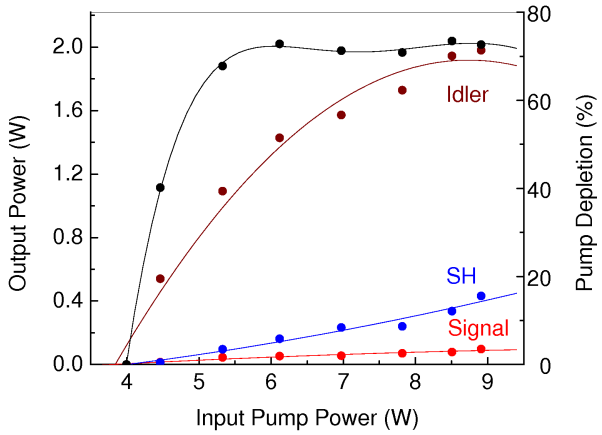

Figure 6.5: Single-frequency blue power, signal power, idler power, and pump depletion as functions of input pump power to the frequency-doubled cw SRO. Solid lines are guides for the eye. Crystal temperature is 125 °C, corresponding to idler, signal and blue wavelengths are 1261 nm, 920 nm and 460 nm, respectively.

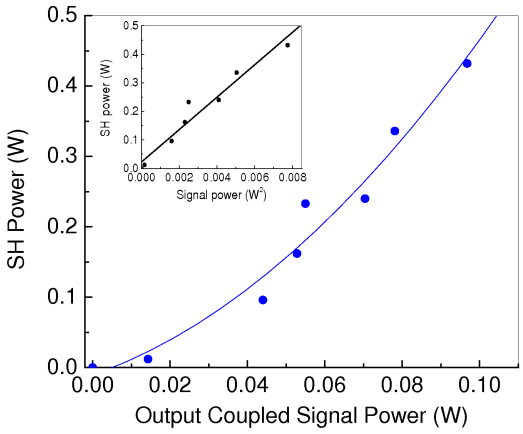

Figure 6.6: Variation of SHG power at a wavelength of 460 nm with out-coupled signal power, showing a quadratic dependence. Inset, linear dependence of SHG power on the square of the out-coupled signal power.

6.3 High-power, cw, stable, single-frequency blue light generation

The maximum available blue output power extracted from the frequency-doubled cw SRO described in Section 6.2.2.2 is limited by the intracavity signal power and its spatial mode quality. As we are operating in the saturation region of SRO operation, we can not achieve further increases in signal power with increased pumping level. We can, however, attempt to improve the spatial mode quality of the resonating signal, as it is solely affected by thermal effects in the MgO:sPPLT nonlinear crystal due to the relatively large pump focusing parameter (ξ_{SRO}=2) as described in Chapters 4 and 5. Therefore, thermal effects, and thus the spatial beam quality of the signal, can be improved by using looser pump focusing along with a longer SRO cavity, in order to enhance the maximum blue output power.

6.3.1 Experimental configuration

Figure 6.7 shows the schematic of the experimental setup, which is similar to the experimental configuration in Fig. 6.1. The ring cavity comprises two concave reflectors, M_6 and M_7, and two plane mirrors, M_3 and M_4. Unlike the previous configuration, however, the mirrors M_6 and M_7 are of radius of curvature r=100 mm. All the mirrors have the same coating specifications as described in Section 6.2.2.2, that is highly reflecting (R>99.9%) for the resonant signal (840−1000 nm) and highly transmitting (T=85−90%) for the idler (1100−1400 nm), thus ensuring SRO operation. M_4 also has high transmission (T=85−90%) over 425−500 nm. The nonlinear crystal is the same MgO:sPPLT (d_{eff} ∼10 pm/V) of length 30 mm with a single grating of period, Λ=7.97 μm. The pump is a frequency-doubled, cw, single-frequency Nd:YVO_4 laser.

For internal SHG, we used BIBO as the nonlinear crystal and a 500-μm-thick uncoated fused silica etalon (FSR =206 GHz, Finesse ∼0.6) is used at the second cavity waist between M_3 and M_4 and adjacent to the BIBO crystal for frequency selection and mode-hop-free operation of the SRO. The BIBO crystal is 5 mm in length and cut for type-I interaction ($ee \rightarrow o$) in the yz-plane (ϕ=90°) at an internal angle θ=160° at normal incidence (d_{eff} ∼3.4 pm/V). The crystal faces are AR-coated for the resonant signal (R<0.5%) and for the SHG wavelengths (R<0.8%).

A lens of focal length 150 mm was used to focus the beam at the center of the crystal to a pump beam waist of ∼33 μm (ξ_{SRO}=1.28), corresponding to a signal beam waist of ∼39.55 μm at 900 nm. The calculated beam waist of the signal at the center of the BIBO crystal is 200 μm. The total optical length of the cavity including the crystals and etalon is 690 mm, corresponding to a FSR ∼ 434 MHz.

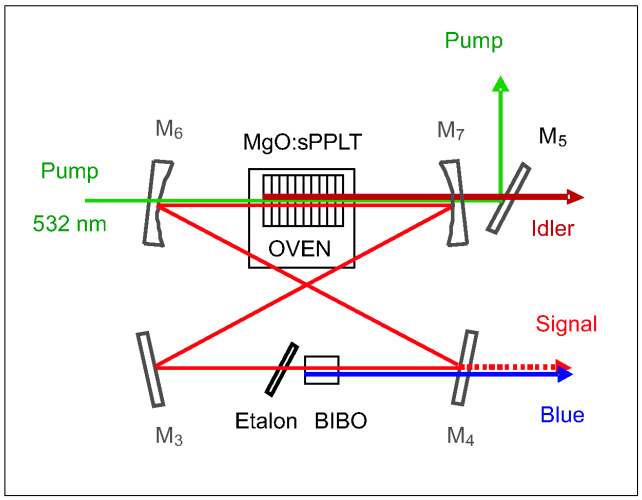

Figure 6.7: Schematic diagram of the intracavity frequency-doubled MgO:sPPLT cw SRO for high blue generation.

6.3.2 Results and discussions

6.3.2.1 Power across the tuning range

By varying the MgO:sPPLT crystal temperature from 71 °C to 240 °C, the signal could be tuned from 978 to 850 nm. The corresponding SHG wavelengths from 489 to 425 nm are generated by varying the BIBO crystal angle from 163.8°to 155.2°. Figure 6.8(a) shows the extracted SH blue power across the tuning range. The measured blue power varies from 145 mW at 425 nm to 360 mW at 489 nm, with as much 1.27 W available at 459 nm with a green to blue conversion efficiency in excess of 14% at a crystal temperature of 128 °C. We extracted >500 mW of blue power over 58% of the tuning range and >250 mW over 84% of the tuning range. The sudden fall in the blue power near 450 nm is due to the rise in the signal coupling loss through mirror M_4, which results in reduced intracavity signal power and thus lower SHG conversion efficiency. As such, the use of a more optimized coating for M_4 with minimum transmission loss across the signal tuning range will readily overcome the dip in SHG power. The overall decline in blue power towards

the shorter wavelengths is, however, attributed to the reduction in intracavity signal power due to the increased effects of thermal lensing near the extremes of the SRO tuning range (higher temperatures), higher MgO:sPPLT crystal coating losses, and parametric gain reduction away from degeneracy, as observed previously in Chapters 4 and 5. As evident in Fig. 6.8(b), there is also >100 mW of useful signal output available over 850−915 nm (50% of total signal tuning range), with 970 mW at 900 nm. In addition to the blue and signal radiations, the SRO simultaneously generates substantial levels of non-resonant idler radiation with powers of more than 780 mW, with as much as 2.6 W across the 1167−1422 nm tuning range.

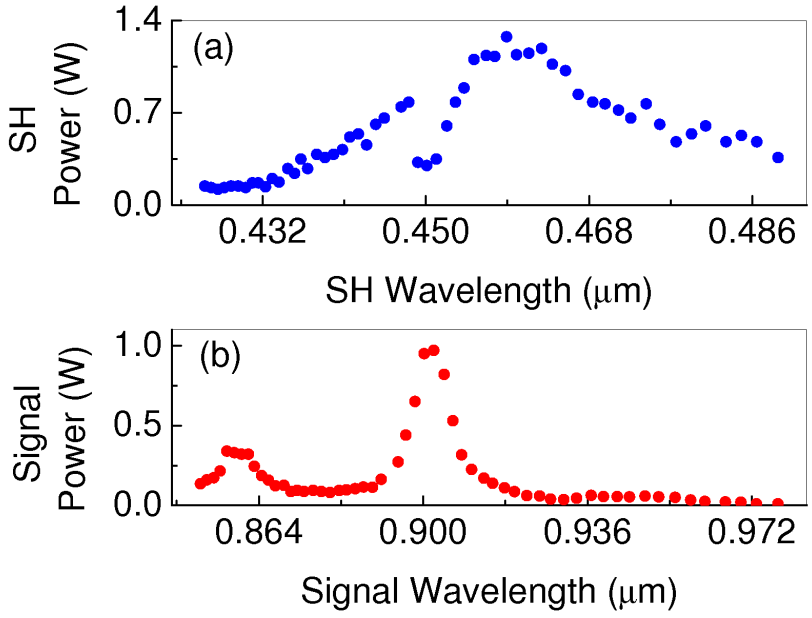

Figure 6.8: (a) Second-harmonic blue power, and (b) out-coupled signal power, across the tuning range.

Figure 6.9 shows the blue power at 459 nm as the function of the out-coupled signal power by varying the input pump power. As expected, the increase in SHG power with out-coupled signal power is seen to be quadratic, also implying quadratic variation with the intracavity signal power. The inset of the Fig. 6.9 also confirms

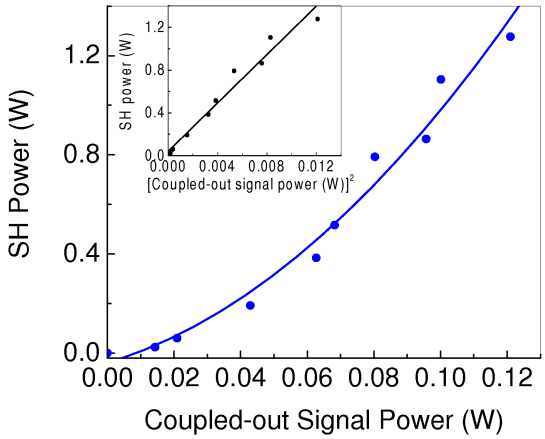

Figure 6.9: Quadratic dependence of SHG power on out-coupled signal power. Inset: linear dependence of SHG power on the square of the out-coupled signal power.

the linear variation in SHG power with the square of the out-coupled signal power, as expected.

6.3.2.2 Single-frequency-stability

We analyzed the spectrum of the generated blue light using a confocal scanning Fabry-Perot interferometer (FSR=1 GHz, Finesse∼400). A typical transmission fringe pattern at maximum blue power at 459 nm is shown in Fig. 6.10, confirming single-frequency operation with an instantaneous linewidth of ∼8.5 MHz. Similar behaviour was observed throughout the tuning range in the blue.

In the absence of active frequency control, we recorded mode-hope-free, single-mode behavior of the blue output using a wavemeter (BRISTOL 612A, resolution 0.2 pm). As evident in Fig. 6.11, passive frequency-stability of the system is better than 280 MHz (limited by the wavemeter resolution) over a time-scale of 340 seconds, implying the possibility of stable single-frequency operation over longer time with active stabilization and improved thermal isolation of the system from the laboratory environment.

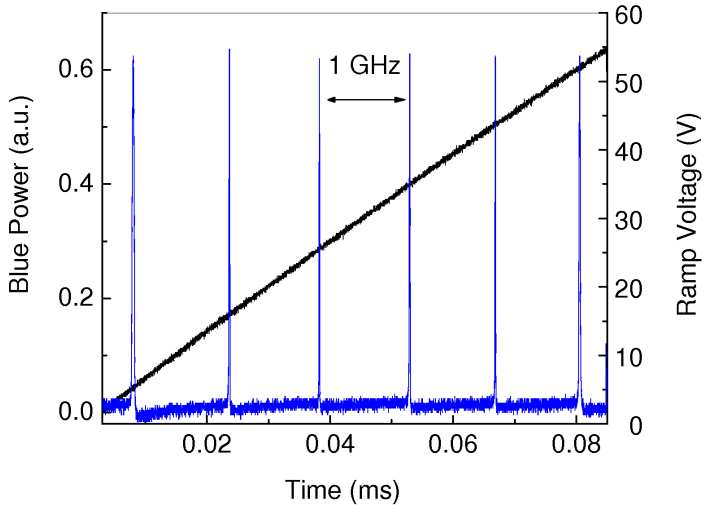

Figure 6.10: Single-frequency spectrum of the generated blue light recorded by a scanning Fabry-Perot interferometer.

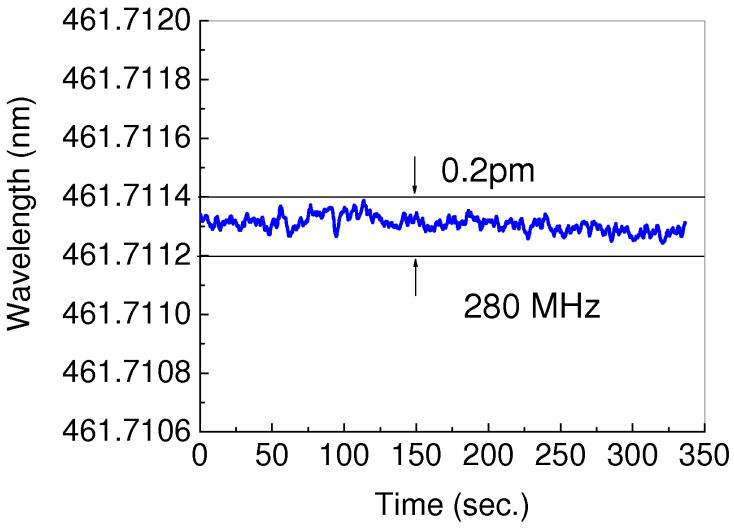

Figure 6.11: Wavelength stability of the single-frequency blue radiation over time. The crystal temperature was fixed at 128 °C, corresponding to a signal wavelength of 923 nm.

6.3.2.3 Beam profile

The far-field energy distribution of the blue beam at 460 nm, together with the intensity profile (pink curves) and the Gaussian fits (yellow curves) along the two orthogonal axes, are shown in Fig. 6.12. The oblique line pattern on the color beam plot is interference fringes caused by attenuation optics used to reduce blue intensity to the beam-profiler. The beam intensity profile along the two orthogonal axes appears to confirm a Gaussian distribution, although full confirmation of TEM_{00} character requires measurements of M^2 values. The ellipticity of the spot is 0.69, attributed to spatial walk-off in the BIBO crystal as well as the astigmatism of the signal beam caused by the relatively large tilt angles (15°) on M_1 and M_2 to extract the blue beam out of the compact ring cavity.

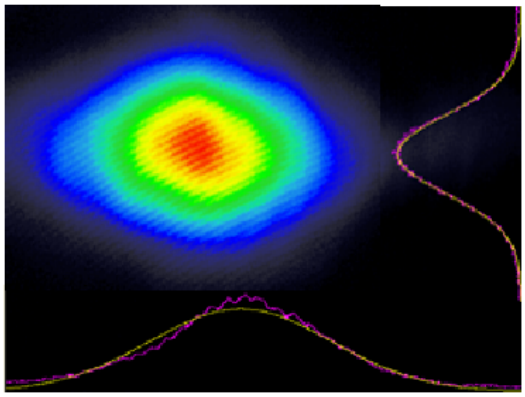

Figure 6.12: TEM_{00} energy distribution, beam profiles (pink curves), and Gaussian fits (yellow curves) of the generated green beam in the far-field.

6.4 Conclusions

In this Chapter, we have demonstrated practical solid-state sources tunable across the 425-489 nm spectral range in the blue. Intracavity frequency doubling of the cw

SRO based on MgO:sPPLT has enabled the generation of up to 1.27 W of single-frequency blue output along with >100 mW of useful signal over 850−915 nm, with 970 mW at 900 nm, and non-resonant idler powers of more than 780 mW, with as much as 2.6 W across 1167−1422 nm. The demonstrated tuning range of the blue is at present limited by the grating period of the MgO:sPPLT crystal, and so can be extended to cover the entire range of 300−530 nm using alternative gratings. The use of other grating periods will also enable blue generation at lower temperatures, reducing the effects of thermal lensing, and thus extending the higher powers to shorter wavelengths. Moreover, by resonating the idler wave in the 1140−1420 nm range, tunable generation across the 570−710 nm will also be possible, making this a promising approach for the generation of high-power, widely tunable, cw radiation across the 300−700 nm spectral range.

Chapter 7

High-power, cw green light sources

This Chapter constitutes with the following journal publications:

1. *High-power, continuous-wave, second-harmonic generation at 532 nm in periodically-poled $KTiOPO_4$*
   G. K. Samanta, S. Chaitanya Kumar, C. Canalias, V. Pasiskevicius, F. Laurell, and M. Ebrahim-Zadeh
   Optics Letters 33, 2955–2957 (2008).

2. *9.6 W, stable, continuous-wave, single-frequency, fiber-based green source at 532 nm*
   G. K. Samanta, S. Chaitanya Kumar, and M. Ebrahim-Zadeh
   Optics Letters 34(10), 1561–1563 (2009).

3. *High-power, single-frequency, continuous-wave, second-harmonic-generation of ytterbium fiber laser using PPKTP and MgO:sPPLT*
   S. Chaitanya Kumar,**G. K. Samanta**, and M. Ebrahim-Zadeh
   Optics Express (Communicated) 2009.

7.1 Motivation

High-power, cw, single-frequency sources in the green are of great interest for a variety of applications, including pumping of Ti:sapphire lasers and cw singly-resonant optical parametric oscillators (SROs) pumped in the visible [13; 58; 70]. To date, practical realization of such sources has relied almost exclusively on internal second-harmonic generation (SHG) of cw Nd-based solid-state lasers. While these tech-

niques have proved highly effective, the attainment of stable, high-power, and single-frequency operation generally requires elaborate system designs involving intricate cavity configurations for internal doubling, careful management of thermal effects, and active stabilization, resulting in relatively high complexity and cost.

It would be desirable to devise alternative approaches for the development of such sources using more simplified and cost-effective techniques. An attractive and straightforward approach to generate cw green radiation is external single-pass second-harmonic generation (SHG) of high-power lasers. As the optical gain for cw single-pass SHG is very low, (keeping in mind the laser induced damages in the nonlinear crystal), for efficient SHG, high effective nonlinearity and long interaction length of the nonlinear crystal are required.

Quasi-phase-matched (QPM) ferroelectric nonlinear materials have had a major impact on optical frequency conversion technology due to their high effective nonlinearity and long interaction length. In particular, the advent of periodically-poled $LiNbO_3$ (PPLN) has enabled the development of new generation of devices with unprecedented performance capabilities. At the same time, the onset of photorefractive damage under exposure to visible radiation has confined the utility of PPLN mainly to the IR. Doping with MgO can partially alleviate this problem, permitting the use of MgO:PPLN at higher powers and lower temperatures [71; 72]. However, residual effects of photorefractive damage continue to restrict operation of devices based on MgO:PPLN mainly to the near- and mid-IR. For frequency conversion in the visible, QPM materials such as MgO-doped periodically-poled stoichiometric $LiTaO_3$ (MgO:sPPLT) [72; 73] and periodically-poled $KTiOPO_4$ (PPKTP) [72; 74–77] are attractive alternatives, offering increased resistance to photorefractive damage, relatively high effective nonlinearities (d_{eff} ~10 pm/V) and a coercive voltage one-order-of magnitude lower than congruent PPLN enabling electric field poling of

thicker materials with short domain periods. Advances in the material growth and the fabrication techniques have also led to the availability of such QPM materials with high optical quality, shorter grating periods, and long interaction lengths (up to 30 mm), enabling the development of frequency-conversion devices for the visible in the cw [72; 74; 75] and low-intensity pulsed regimes [77].

Earlier reports of cw SHG in the visible based on PPKTP include intracavity [74], external enhancement cavity [75], and single-pass configurations [78] at 532 nm. The highest cw SH power achieved so far has been 2.3 W in multimode output [74] at a wavelength of 532 nm. As such, power scaling of SHG and performance of this material at increased powers has not been explored.

This Chapter consists of three sections. In Section 7.2, we present efficient generation of cw, single-frequency green light tunable in the wavelength range from 511.9 nm to 517.3 nm using simple external single-pass SHG in a multi-grating PPKTP crystal with conversion efficiency as high as 15.8%. The maximum output power of cw green radiation obtained is about 1.2 W. The linewidth measured is about 4.5 MHz. In Section 7.3, we demonstrate the generation of 6.2 W of cw, single-frequency radiation at 532 nm with a single-pass conversion efficiency as high as 20.8%. We also investigate the thermal issues relating to the power scaling of the SHG process for the fundamental powers up to 30 W and discuss strategies for increase output power and efficiency at higher pump powers. As the generated power of the green radiation using frequency doubling in PPKTP crystal is limited to 6.2W, for higher green power we explore alternative material. In Section 7.4, we describe external single-pass SHG of a cw, single-frequency, ytterbium (Yb) fiber laser at 1064 nm in MgO:sPPLT. The source can deliver 9.64 W of cw, single-frequency output power at 532 nm at a conversion efficiency as high as 32.7% in a TEM_{00} spatial profile with peak-to-peak power stability of 9% over 13 hours and

frequency-stability <32 MHz over 30 minutes. These characteristics make the device a very attractive, compact, and cost-effective source for many applications, including pumping of Ti:sapphire lasers and cw single-frequency SROs.

7.2 Tunable SHG of the solid-state thin-disk Yb:YAG laser in PPKTP

7.2.1 Experimental configuration

The schematic of the experimental setup is shown in Fig. 7.1. The pump source (Versadisk-1030, ELS, Germany) is a diode-pumped thin-disk Yb:YAG laser, which can generate single-frequency output with a power up to 30 W across the tuning range of 1023−1035 nm. The tuning of the Yb:YAG laser is performed using an intra-cavity Lyot filter. In order to maintain a stable performance of the pump laser, we operated it at it's maximum output power, and used a power attenuator comprising a half-wave-plate and a polarizing beam-splitter to regulate the fundamental power delivered into second-harmonic PPKTP crystal. A second half-wave-plate was used to yield the correct pump polarization for phase-matching. After the half-wave-plates and polarizing beam-splitter, the fundamental beam was focused into the PPKTP crystal with a 300-mm focal length lens in a single-pass configuration. The radius of pump beam waist ($1/e^2$-intensity) at the center of the crystal is $\sim$40 μm, corresponding to a focusing parameter ξ=1.1. An uncoated, 20-mm-long, multi-grating PPKTP crystal was used in our experiment. The crystal has a 1×8 mm^2 aperture and is housed in an oven with a temperature stability of $\pm$0.1 °C. The crystal was fabricated with 11 grating periods ranging from 7.9 μm to 9.47 μm, with increasing steps of $\sim$0.157 μm, to provide phase-matched SHG over fundamen-

tal wavelength range from 1.021 μm to 1.091 μm with the temperature tuning from room-temperature to 200 °C. The width of each grating is about 400 μm.

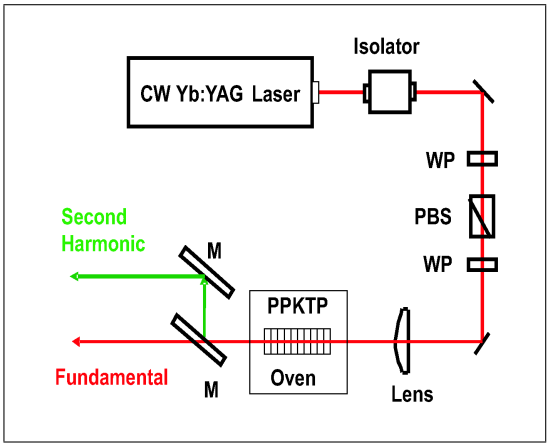

Figure 7.1: Schematic diagram of the single-pass SHG of the diode-pumped, thin-disk Yb:YAG laser using PPKTP.

7.2.2 Results and discussions

7.2.2.1 Wavelength tuning of the SHG process

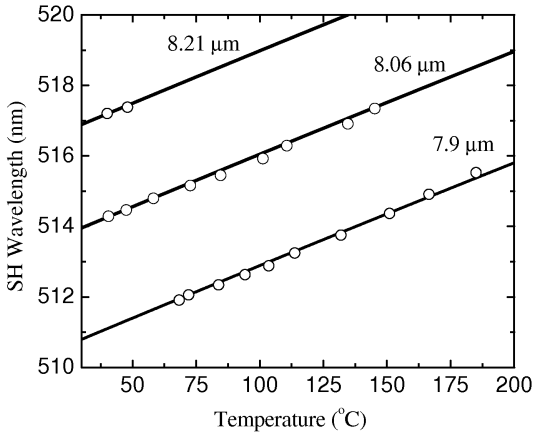

Figure 7.2: Tuning of second-harmonic (SH) wavelength as a function of the crystal temperature for different grating periods. The circles and solid curve are the experimental and theoretical data, respectively.

A SHG tuning range of 511.9−517.3 nm, limited by the available fundamental

wavelength, is obtained with three grating periods of 7.9 μm, 8.06 μm, and 8.21 μm under temperature tuning of the crystal from room-temperature to 200 °C. The experimental second-harmonic (SH) wavelengths and theoretical data using the Sellmeier equations [79] as function of crystal temperature is shown in Fig. 7.2, where a good agreement between the experiment and theory is evident.

7.2.2.2 Temperature acceptance bandwidth of the PPKTP crystal

To characterize the quality of the grating, we measure the temperature acceptance bandwidth of the crystal, as shown in Fig. 7.3. Thermal effects due to the crystal absorption at the fundamental and SH wavelengths were avoided by chopping the fundamental beam with a frequency of 600 Hz and 5% duty cycle. The circles in Fig. 7.3 shows the measured SH output power as a function of crystal temperature for a grating period of 8.06 μm. With the theoretical fit (solid black line) to the experimental data, the temperature acceptance bandwidth (FWHM) of the crystal was determined to be $\triangle \mathrm{T}_{Fit}$ =2.6 °C at the phase-matching temperature T_{Exp}^{PM} =81.4 °C. Using the dispersion equations [79] for PPKTP crystal and wave-vector mismatch formulas [26] under the same experimental conditions, we found a theoretical temperature acceptance bandwidth, $\triangle \mathrm{T}_{Cal}$ =1.9 °C at the phase-matching temperature T_{Cal}^{PM} =75.1 °C. Using the same relations, if we calculate the grating period required for perfect phase-matching at 81.4 °C, we found a theoretical grating period of 8.055 μm. Therefore, the shift in phase-matching temperature can be explained by the change in third decimal place of the grating period. Uning the theoretical and experimental temperature acceptance bandwidths in Equation (7.1), the effective interaction length of the PPKTP crystal can be calculated to be 14.6 mm for a physical length,L=20 mm.

$$L_{eff} = \frac{\triangle T_{Cal}}{\triangle T_{Fit}} L \tag{7.1}$$

The discrepancy between the physical length and measured effective length is attributed to imperfections in the grating structure and non-ideal focusing.

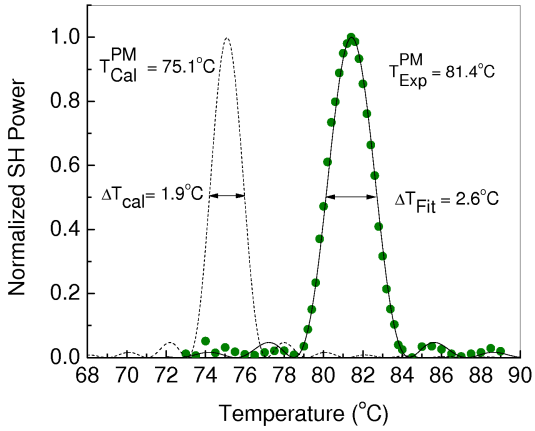

Figure 7.3: Temperature dependence of the second-harmonic power. The circles represent experimental data; the solid line represents fit, and the dotted line represents theoretical data. Temperature acceptance bandwidth is about 2.6 °C.

7.2.2.3 Power scaling

By using a chopper and measuring the average green power at different average fundamental powers, we recorded the internal doubling efficiency at the fundamental wavelength of 1.031 μm. Figure 7.4 shows the measured green peak power as a function of the peak input fundamental power. At the maximum peak fundamental power of 15.3 W, the single-pass conversion efficiency obtained is about 15.8%, generating a peak SH power of 2.43 W. As evident in the Fig. 7.4, the SH output power is still increasing quadratically, and conversion efficiency is increasing linearly with the input fundamental power, without showing saturation. This implies the possibility of further scaling of the SH power and conversion efficiency, subject to

the damage limit of the PPKTP crystal and its thermal effects at higher powers.

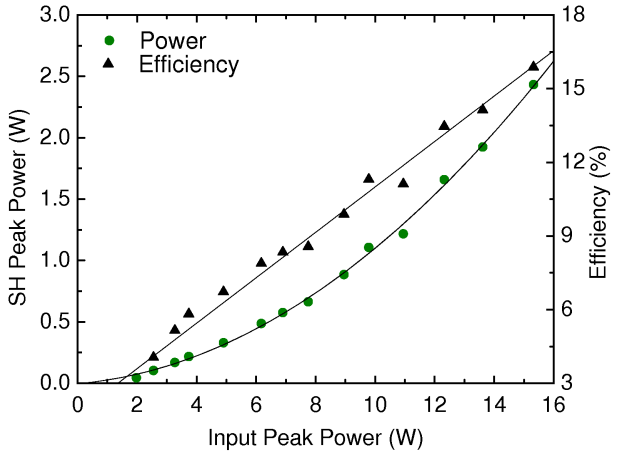

Figure 7.4: The generated SH peak power and conversion efficiency as a function of input peak pump power under chopped condition. The duty cycle of the chopper is 5%.

We also performed cw SHG experiments under high fundamental power without the chopper. With a pump power of 13.6 W, we obtained 1.2 W of cw green radiation at 515.5 nm with a maximum single-pass conversion efficiency of 8.8%, as shown in Fig. 7.5. The discrepancy between the maximum single-pass conversion efficiency at quasi-cw operation and cw operation can be attributed to thermal effects in the PPKTP crystal at high-power levels, although confirmation necessitates a comprehensive study of the behavior of PPKTP crystal at higher pump and SH power levels, as explained in Section 7.3.

From the Fig. 7.5, it is evident that the efficiency of the SHG under cw operation is increasing linearly with the increase in the pump power, but there are two distinct slopes, one in the pump power range from 0 to 2 W (low pump power regime), and another from 2 W to 13 W (high pump power regime). The slope efficiencies of these two regimes can be calculated from Fig. 7.6 to be 1.27% W^{-1} and 0.664% W^{-1}, respectively. Using these slope efficiencies and formulas for effective nonlinerity [45], the effective nonlinear coefficients of the PPKTP crystal for the low power regime

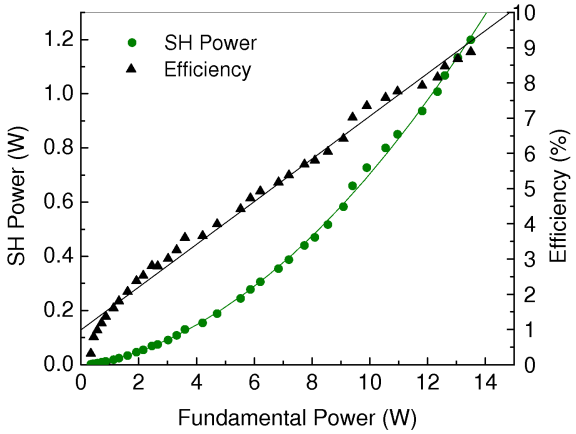

Figure 7.5: The generated SH power and conversion efficiency as a function of the input pump power.

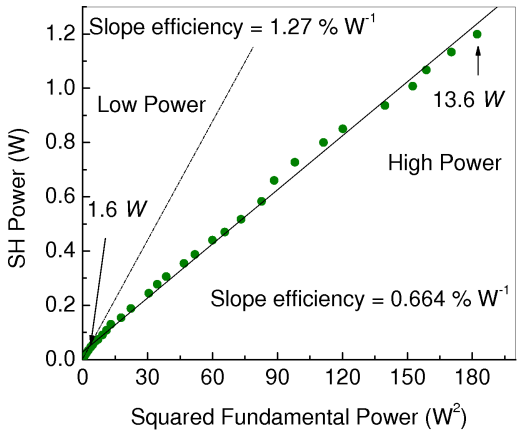

Figure 7.6: Variation of the generated cw SH power as a function of the square of the fundamental power.

and high-power regime are 4.61 pm/V and 6.37 pm/V respectively. The deviation of the effective nonlinear coefficient from the reported value [80] can be attributed to different parameters, including imperfection in the grating periods, as explained in Section 7.3.

With a scanning confocal Fabry-Perot interferometer (FSR = 1 GHz, Finesse ∼400), we measured the linewidth of the single-frequency cw green light at the wavelength of 515.5 nm to be about 4.5 MHz, as shown in Fig. 7.7, which is in reasonable agreement with the linewidth (< 5 MHz) of the fundamental.

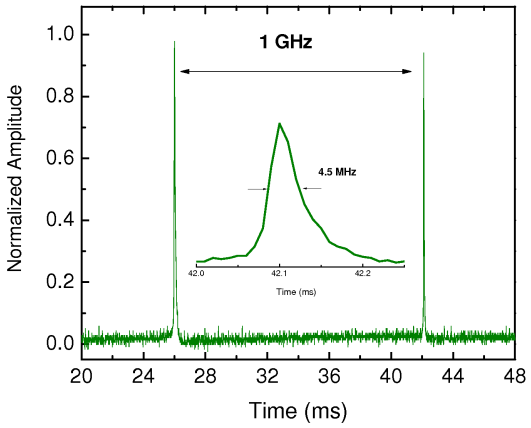

Figure 7.7: The single-frequency spectrum of cw SHG at the wavelength of 515.5 nm. The linewidth is about 4.5 MHz.

7.3 SHG of high-power cw fiber laser in PPKTP crystal

7.3.1 Experimental configuration

A schematic of the experimental setup is shown in Fig. 7.8. The fundamental pump source is a cw Yb fiber laser (IPG Photonics, YLR-30-1064-LP-SF). The laser delivers up to 30 W of single-frequency radiation at 1064 nm in a linearly polarized

beam with a diameter of 3 mm, M^2 factor <1.01, and a measured instantaneous linewidth of 12.5 MHz. In order to maintain stable output characteristics, we operated the pump laser at the maximum power and used an attenuator comprising a half-wave-plate (HWP) and polarizing beam-splitter to vary the input fundamental power to the crystal. A second HWP was used to yield the correct pump polarization for phase-matching. The fundamental beam was focused to a measured beam waist radius of 37 μm ($1/e^2$-intensity) at the center of the crystal, corresponding to a focusing parameter ξ=1.28. The bulk PPKTP crystal is fabricated by our collaborators from Sweden [81] from a c-cut 19-mm-long, 1-mm-thick, and 6-mm-wide flux-grown KTP sample. The c- face of the crystal was patterned with a photo-resist grating of 9.01 μm period and was covered with an Al film over 17 mm length at the center, keeping a 1 mm free zone on each side of the grating. The actual length of the grating is thus 17 mm. The crystal was poled by applying 5-ms-long electric field pulses of 2.5 kV/mm in magnitude [81]. The PPKTP is housed in an oven with a temperature stability of $\pm$0.1 °C. The crystal faces are antireflection coated (R<1%) at 1064 nm and 532 nm. A dichroic mirror, *M*, coated for high reflectivity (R>99%)at 1064 nm and high transmission (T>94%) at 532 nm, extracted the generated green output from the fundamental.

7.3.2 Results and discussions

7.3.2.1 Temperature acceptance bandwidth

To characterize the PPKTP sample, we first determined the dependence of the SHG power on crystal temperature. To avoid unwanted contributions from thermal effects, we performed the measurements at a low fundamental power of 1 W, resulting in 8.3 mW of green output at a phase-matching temperature of 30.8 °C, as shown in Fig. 7.9. The solid curve is a $sinc^2$ fit to the data, confirming the expected

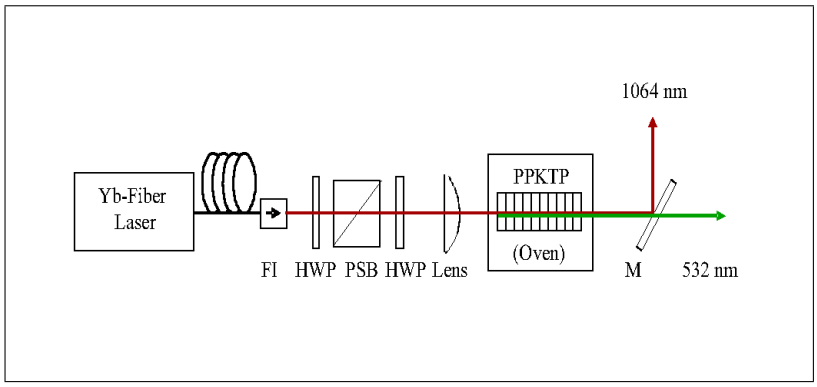

Figure 7.8: Schematic of the experimental design for single-pass SHG of the cw Yb fiber laser in PPKTP. FI, Faraday isolator, HWP, half-wave-plate; PBS, polarizing beam-splitter; L, lens (f=20 cm); M, dichroic mirror.

temperature dependence of SHG. The FWHM of the curve is $\triangle$T=3 °C, which is slightly wider than the calculated value of 2.62 °C from the Sellemier equations [79]. The effective interaction length, L_{eff}, as defined by Equation (7.1), of the PPKTP crystal is 14.84 mm for 17 mm physical length of the crystal. The discrepancy between the physical length and the measured effective length is attributed to the imperfections in the grating structure and nonideal focusing of the pump. To realize the practical high-power green source, we should have more precise knowledge of the behavior of the temperature acceptance bandwidth of the PPKTP crystal at higher pump power levels. We measured the temperature acceptance bandwidth in the PPKTP crystal at three different input pump powers, 5 W, 15 W and 25 W, with results shown in Fig. 7.10. As evident in Fig. 7.10, there is a clear shift in the perfect phase-matching temperature of the PPKTP crystal for higher pump powers and also the phase-matching temperature curves are loosing their natural $sinc^2$ shape at higher pump powers. These effects can be attributed to the low thermal conductivity [82] and high absorption of PPKTP crystal, leading to the inhomogeneous distribution of heat in the crystal, thus indicating thermal phase-mismatch. These effects are discussed in more details in Section 7.3.2.2.

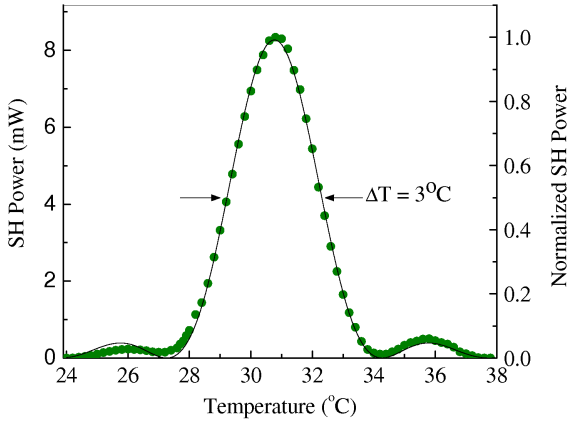

Figure 7.9: Temperature tuning curves of PPKTP at 1 W of fundamental power.

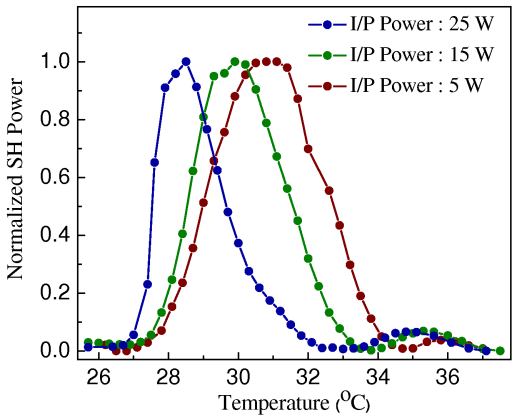

Figure 7.10: Temperature tuning curves of PPKTP at different fundamental powers.

7.3.2.2 Power scaling and thermal effects in the PPKTP crystal

We performed measurements on the SHG efficiency and SHG power up to the maximum fiber laser power of 30 W, with the results shown in Fig. 7.11. The fundamental power was measured at the input to the crystal, while the generated green power was corrected for the 6% transmission loss of mirror *M*. We obtained 6.2 W of green power at the full input power of 29.75 W, representing a single-pass conversion efficiency of 20.8%. As evident in Fig. 7.11, the quadratic increase in SH power and corresponding linear variation in efficiency are maintained up to 15 W of input power, after which saturation sets in. Beyond this value, SH power increases linearly with fundamental power. The saturation effect is attributed to the depletion of the fundamental [72] and thermal phase mismatch in the PPKTP crystal, owing to a number of factors. These include green-induced IR absorption (GRIIRA) of the fundamental, two-photon absorption (TPA) of the fundamental and generated green, and linear absorption at both wavelengths.

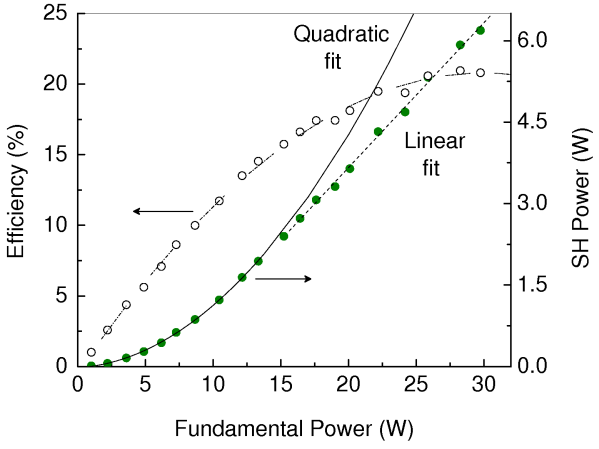

Figure 7.11: Dependence of the measured SH power and the corresponding conversion efficiency on the incident fundamental powers.

To verify any contribution from GRIIRA to thermal dephasing, we focused 6 W of green radiation from a cw laser at 532 nm (Coherent, Verdi-10) to a beam radius

of 34 μm inside the crystal to obtain similar maximum green power density (0.33 MW/cm^2) as in the SHG experiments. The arrangement resulted in the simultaneous focusing of the fundamental fiber laser IR beam to a waist radius of 28 μm inside the crystal, close to 37 μm used in the SHG experiments. We then measured the variation in transmitted IR power at different green power levels over 10 minutes periods. However, we observed no difference in the transmitted IR power with and without green radiation, indicating the absence of GRIIRA up to the maximum green power of 6 W.

We also investigated the possible role of TPA by recording the crystal transmission at both the fundamental and green wavelengths at power levels up to 30 W and 6 W, respectively. We obtained a linear increase in the transmitted power with the input power at both wavelengths, as shown in Fig. 7.12, from which linear absorption losses of 0.3%/cm at 1064 nm (Fig. 7.12 (a)) and 4.5%/cm at 532 nm (Fig. 7.12 (b)) were deduced, in agreement with previous results [83].

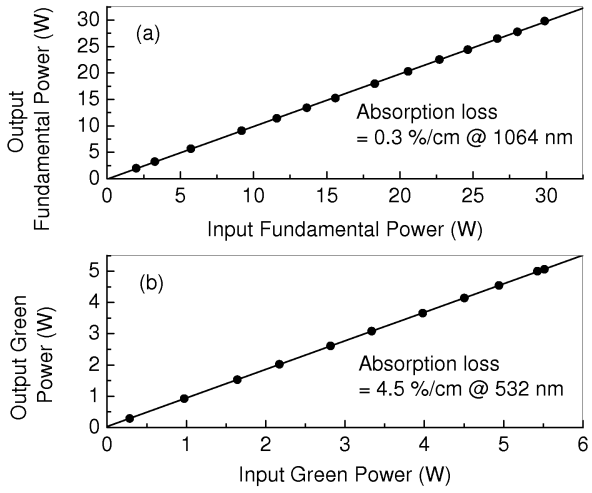

Figure 7.12: Linear dependence of the transmitted power with the input power at (a) fundamental (1064 nm), and (b) SH (532 nm) in the PPKTP crystal showing no evidence of TPA.

These measurements thus confirmed that the thermal dephasing in the PPKTP

crystal was also not due to TPA, but a result of intrinsic linear absorption of the IR and the green, leading to increased heating of the crystal at higher powers. We determined a normalized conversion efficiency of ∼1.2%/W below 15 W of fundamental power, monotonically decreasing to ∼0.7%/W with the rise in input power to 29.75 W, confirming increased thermal dephasing due to linear absorption at higher powers. The normalized efficiency values do not account for absorption losses in the crystal. From the normalized efficiency of 1.2%/W and the focusing parameter of ξ =1.28 (h∼0.85), the effective nonlinearity is calculated as d_{eff} ∼7.63 pm/V for the 17 mm grating, corresponding to d_{33} ∼12 pm/V. This value is 77.9% of previous results [80], which we attribute to crystal absorption of the green and IR power, laser linewidth, and imperfections in the grating structure such as missing periods and duty factor variations. Considering the absorption losses of 0.3%/cm at 1064 nm and 4.5%/cm at 532 nm, we determined a normalized efficiency of ∼1.33%/W below 15 W of fundamental power, resulting in d_{eff} ∼8.6 pm/V, corresponding to d_{33} ∼13.5 pm/V for a 14.8 mm PPKTP crystal with 50% duty factor. As the missing periods are included in the effective length, the deviation in the calculated d_{33} from earlier value [80] can be due to the grating duty factor and the laser linewidth. However, using the Sellmeier equations [79], the calculated FWHM spectral acceptance of the 17 mm crystal (0.157 nm) is much wider than the laser linewidth (12.5 MHz), confirming the discrepancy due to the duty factor of the grating.

To gain further insight into the thermal effects in the PPKTP crystal, we recorded the SHG phase-matching temperature at different fundamental powers, as shown in Fig. 7.13. Although no significant shift in the phase-matching temperature was observed at the lower input powers, a monotonous decrease in the phase-matching temperature, at a rate of 0.19 °C/W, was measured above 15 W, further confirming crystal heating at higher input powers. At lower powers, linear absorption does

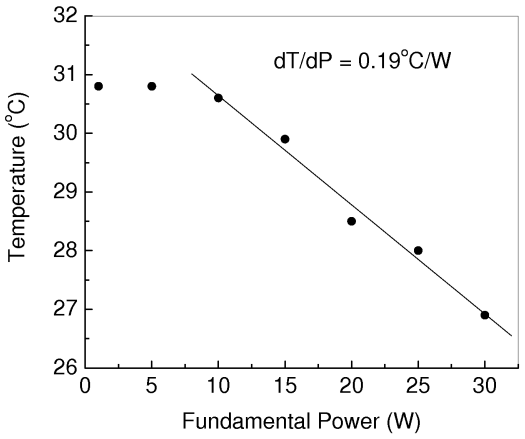

Figure 7.13: Dependence of the phase-matching temperature on the fundamental power of the PPKTP crystal.

not significantly affect the phase-matching temperature, whereas at higher powers it heats the crystal, reducing the optimum value for phase-matching and thus requiring a reduction in crystal temperature for maximum green generation. Since phase-matching for the present PPKTP sample is near room-temperature, further optimization of the crystal temperature using Peltier cooling or the use of a grating period for higher phase-matching temperature could potentially lead to increased green power and efficiency at the higher input powers up to 30 W and above, with the possibility of power scaling of green beyond 6 W. Proper management of the generated heat or inclusion of the crystal heating effects in the grating design are other possible strategies to achieve the highest SH power and efficiency.

7.3.2.3 Single-frequency operation

We analyzed the output spectrum at 532 nm using a scanning confocal interferometer (FSR = 1 GHz, Finesse $\sim$ 400). A typical fringe pattern at 25 W of fundamental power (5 W of green) is shown in Fig. 7.14, verifying single-frequency operation. The instantaneous linewidth, measured directly and without accounting for the interferometer resolution, is 8.5 MHz. The same behavior was observed throughout

the pumping range with similar linewidth, confirming robust single-mode operation at all pump powers.

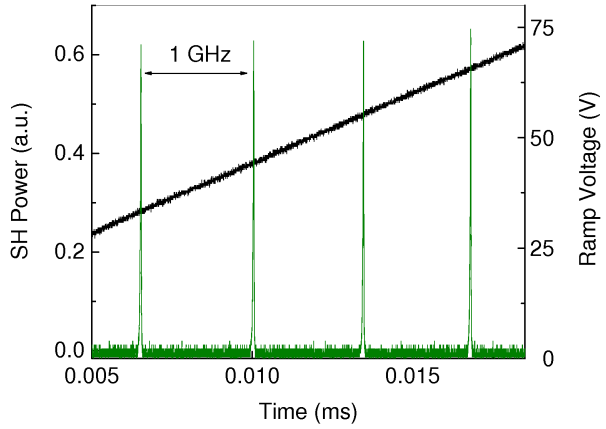

Figure 7.14: Single-frequency spectrum of the green output as recorded by a scanning Fabry-Perot interferometer.

7.3.2.4 Power stability

The generated green power stability for different input pump powers over 60 minutes are shown in Fig. 7.15. Although the output power is very stable with a peak-to-peak power fluctuation of 2.5% at 10 W and 8.6% at 20 W of fundamental power, the SH power degradation has been observed at a higher fundamental powers above $\sim$ 20 W. This degradation in the output power can be attributed to local heating of the PPKTP crystal due to absorption at fundamental, but mostly due to the absorption of the SH radiation. However, the degradation in SH power can be resorted with slight translation of the crystal in the transverse direction relative to the direction of the beam propagation, indicating highly localized light-induced heating effects due to the low thermal conductivity of the PPKTP [82]. Similar output power degradation effect has already been reported for a comparatively low fundamental power of 6.8 W [84]. In our case, the SH power generated at low fundamental

power (< 20 W) is moderately stable over longer periods of time, indicating better performance of PPKTP crystal for low-power SHG operation.

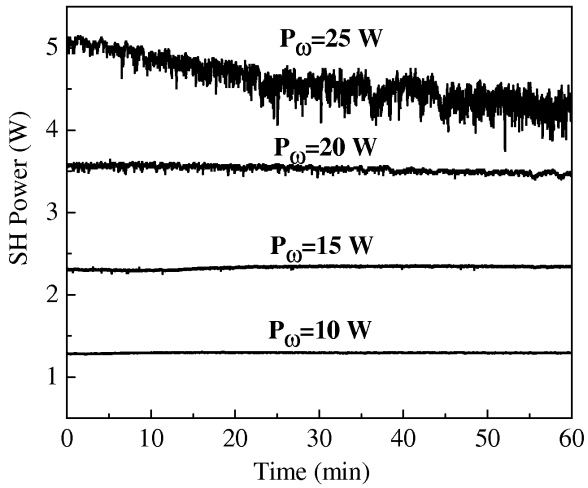

Figure 7.15: SH power stability of PPKTP crystal recorded over one hour at various fundamental power levels.

7.3.2.5 Beam profile

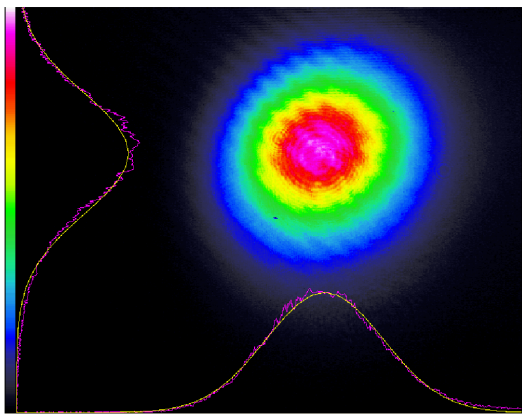

Figure 7.16: TEM_{00} energy distribution, beam profiles (pink curves), and Gaussian fits (yellow curves) of the generated green beam in the far-field.

The far-field energy distribution of the green output beam at 5 W, together with the intensity profile and the Gaussian fits, recorded at 25 W of input power, are

shown in Fig. 7.16. Using a $f = 25$ cm focal length lens and scanning beam profiler, we measured M^2 values of the beam as $M_x^2 \sim 1.29$ and $M_y^2 \sim 1.31$, confirming TEM_{00} spatial mode. Similar M^2 values were measured at different input power levels up to 30 W, showing a small variation in M_x^2 from 1.25 to 1.29 and M_y^2 from 1.2 to 1.34. The M^2-measurement technique is described in Appendix B.

7.4 SHG of high-power, cw, fiber laser in MgO: sPPLT crystal

As mentioned in Section 7.3.2.4, the generation of stable high-power green radiation in PPKTP is limited to a maximum fundamental power of 20 W, due to the degradation of the green power at higher fundamental powers. Therefore, further enhancement in the green power necessities the use of alternative materials. In this section, we describe the use of MgO:sPPLT for high-power operation.

7.4.1 Experimental configuration

The configuration of the experimental setup is similar to the schematic shown in Fig. 7.8. The fundamental pump source is a 30 W, cw, single-frequency Yb fiber laser (IPG Photonics, YLR-30-1064-LP-SF) at 1064 nm, delivering a linearly polarized output beam with a diameter of 3 mm, M^2 factor <1.01, a measured instantaneous linewidth of 12.5 MHz, and a measured frequency-stability of <120 MHz over 1 hour and <50 MHz over 30 minutes. The nonlinear crystal is a 30-mm-long commercially available MgO:sPPLT sample (HC Photonics Corporation, Taiwan), containing a single grating (Λ=7.97 μm), and housed in an oven with a temperature stability of $\pm$0.1 °C. The crystal faces have <0.5% reflectivity at 1064 nm, with >99% transmission at 532 nm. A dichroic mirror, coated for >99% reflectivity at 1064 nm

and >94% transmission at 532 nm, separates the generated green from the input fundamental.

Photograph of the real time cw green source using MgO:sPPLT crystal working in the lab. is shown in Fig. 7.17.

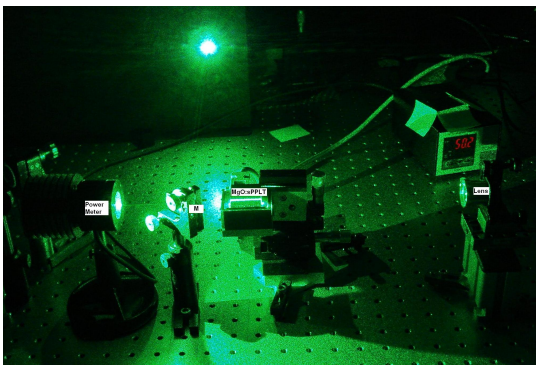

Figure 7.17: Picture of the cw green source using MgO:sPPLT crystal.

7.4.2 Results and discussions

7.4.2.1 Temperature acceptance bandwidth

In order to characterize the MgO:sPPLT sample, we first studied the dependence of SHG power on crystal temperature. We focused 1 W fundamental power to a beam waist of 37 μm at the center of the crystal, resulting green radiation with a maximum power of 12.6 mW at a phase-matching temperature of 52.6 °C, as shown in Fig. 7.18. The measured temperature acceptance bandwidth (FWHM) $\triangle T_{Exp}$ is 1.33 °C. The broadening of the experimental temperature acceptance bandwidth, compared to the theoretical temperature acceptance bandwidth, $\triangle T_{Theo}$ ~0.96 °C, calculated from the Sellmeier equations [52], can be attributed to the imperfections such as duty factor and missing periods in the grating structure and non-ideal focusing. As the long crystal has narrow theoretical temperature acceptance bandwidth (0.96 °C), one necessitates a temperature controller with a stability better than ±0.01 °C

for more precise study of the crystal. To verify the effect of focusing on temperature acceptance bandwidth, we focused the fundamental beam to a beam waist of 90 μm at the center of the crystal, resulting a SH power of 4.3 mW with a temperature acceptance bandwidth, $\triangle T_{Exp}$, of 1.1 °C at a phase-matching temperature 52.8 °C. As, the generated green power is much lower than that of the fundamental power, the small shift in phase-matching temperature with focusing can be attributed to the absorption of fundamental power. The calculated effective nonlinear interaction lengths, defined by Equation (7.1), for beam waists 90 μm and 37 μm are 26.2 mm and 21.6 mm respectively. Thus, shallow focusing along with better temperature control using thermoelectric cooler with higher temperature stability can improve the temperature acceptance bandwidth giving the possibility of nonlinear interaction through out the crystal length. Although, the shallow focusing enhances the effective nonlinear interaction length of the crystal, for a fixed fundamental power of 30 W, we generated less SH power (2.34 W) at 90 μm beam waist compared to 7.59 W of SH power at 37 μm beam waist. Therefore, one needs to optimize the system to generate maximum SH power for a given fundamental power.

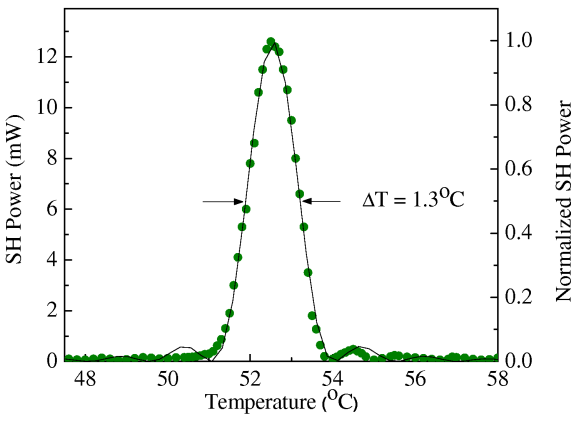

Figure 7.18: Temperature dependence of the SH power (filled circles) and the $sinc^2$ fit (solid curve) at 1 W fundamental power focused to a beam waist of 37 μm at the center of the crystal. The resulting temperature bandwidth is 1.33 °C.

To realize the high-power green source using MgO:sPPLT crystal, one should have clear idea about the characteristic temperature acceptance bandwidths of the crystal at high-powers. Figure 7.19 shows the temperature acceptance bandwidth of 30-mm-long MgO:sPPLT crystal for three different fundamental powers, 10 W, 20 W, and 30 W, focused to a 37 μm beam waist at the center of the crystal. The blue shift in the optimum phase-matching temperature with the increase of the fundamental power (Fig. 7.19) is moderately low as compared to that of PPKTP (Fig. 7.10) due to the high thermal conductivity of MgO:sPPLT crystal [55], implying a better candidate for high-power operation.

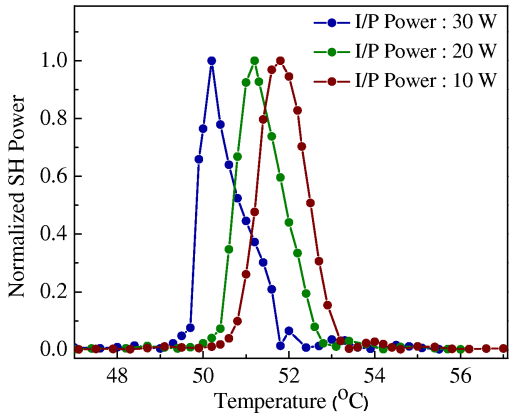

Figure 7.19: Temperature dependence of SH powers (filled circles) and the $Sinc^2$ fit (solid curve) at different fundamental powers focused to a beam waist of 37 μm at the center of the crystal.

7.4.2.2 Optimization of the SHG operation

To optimize the SHG process, we used several focusing conditions corresponding to different values of the focusing parameter $\xi = L/b$ [45]. Here L is the crystal length and b=kw_{op}^2 is the confocal parameter of the pump, with k=$2\pi n_p/\lambda_p$, where n_p, λ_p, and w_{op} are the refractive index, wavelength, and waist radius of the fundamental pump beam inside the crystal, respectively. We measured maximum generated

SH powers and corresponding optimum phase-matching temperatures using seven different focusing conditions, ξ=0.32, 0.81, 1.23, 1.74, 2.48, 4.50, and 6.60 at fixed fundamental power of 29.5 W at the input to the crystal. The results are shown in Fig. 7.20. For weak focusing (ξ <2.48), the maximum SH power increases with the increase in ξ, whereas for tight focusing (ξ >2.48), it decreases with increasing ξ. Interestingly, the extrapolated power curve has a clear peak near ξ ∼2.84, corresponding to the theoretical prediction for optimum SHG in the cw (or long-pulse) limit [45]. We obtained a maximum SH power of 9.64 W at ξ=2.48 (w_{op} ∼31 μm), corresponding to a single-pass conversion efficiency of 32.7% . It is also clear in Fig. 7.20 that the phase-matching temperature decreases with tighter focusing. This is to be expected, since the crystal heating effects due to various absorption mechanisms including green-induced IR absorption (GRIIRA) of fundamental, two-photon absorption (TPA) of fundamental and green, and linear absorption at both wavelengths, are stronger under tight focusing, leading to a greater optically induced temperature rise in the crystal, and therefore necessitating lower externally applied heat to the sample for perfect phase-matching. GRIIRA is not expected to make a significant contribution to crystal heating at these power densities, because of its suppression due to MgO doping [85]. To investigate the role of TPA, however, we recorded crystal transmission at the fundamental up to 30 W, and at the green up to 9 W using a commercial cw green source (Coherent, Verdi-10) as shown in Fig. 7.21. We obtained a linear increase in the transmitted power with the input power at both the wavelengths, thus also confirming the absence of TPA. From the measurements, we deduced a linear absorption loss of 0.17%/cm at 1064 nm (Fig. 7.21 (a)) and 1.58%/cm at 532 nm (Fig. 7.21 (b)), implying far higher contribution to crystal heating would be expected from the green absorption than the fundamental absorption.

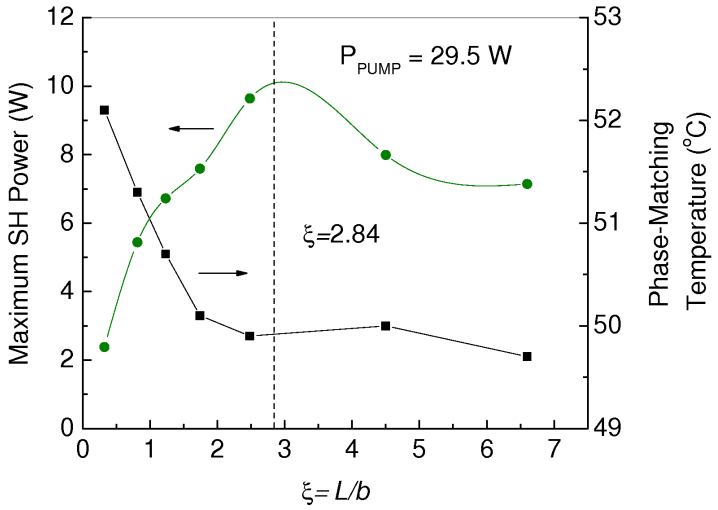

Figure 7.20: Maximum SH power and corresponding phase-matching temperature as a function of the focusing parameter, L/b. The vertical dashed line corresponds to the optimal focusing condition (L/b~2.84) prescribed by Boyd and Kleinman [45]
.

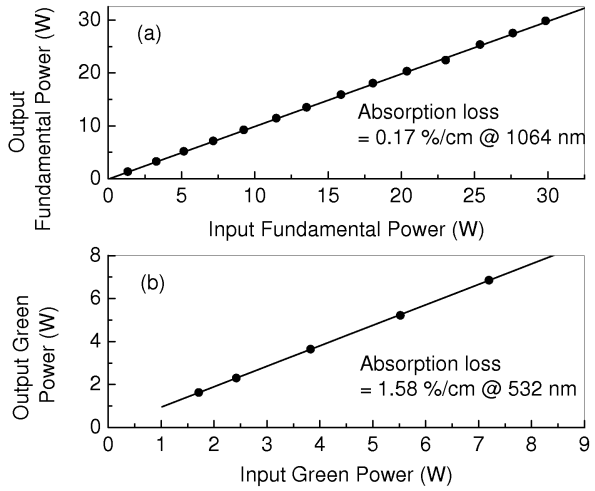

Figure 7.21: Linear dependence of the transmitted power with the input power at (a) fundamental (1064 nm), and (b) SH (532 nm) in the MgO:sPPLT crystal showing no evidence of TPA.

This is also evident in Fig. 7.20, where at a fixed fundamental power of 29.5 W, we observe a strong correlation between the generated SH green power and the corresponding phase-matching temperature. On the other hand, given the significant linear absorption of 0.17%/cm at 1064 nm, the role of fundamental absorption to crystal heating can not be entirely neglected. To verify this contribution, under the focusing condition of ξ=1.74, we rotated the fundamental polarization such that the generated green power was less than 100 mW at 29.5 W of fundamental power. By increasing the fundamental power from 1 W to 29.5 W, we observed a drop in the phase-matching temperature from 52.5 °C to 51.6 °C, clearly indicating still significant contribution of the fundamental absorption to the thermal effects. These studies thus confirm that thermal effects in the MgO:sPPLT crystal were neither due to GRIIRA nor TPA, but a result of intrinsic linear absorption in the IR and green. It has been suggested that the maximum available SH power is limited by the thermal effects resulting either from only the absorption of the fundamental radiation [86] or only the SH power [87]. Our present studies together with our earlier results described in Chapter 5 and also in Ref. [88], confirm that the thermal effects are due to the absorption of both the fundamental and SH power, with the major contribution from the green.

From the measurement of the generated green power in Fig. 7.20, the normalized conversion efficiency was calculated to vary from 0.42%/W at ξ=0.32 to 1.26%/W at ξ=6.60, with a maximum of 1.70%/W at ξ=2.48. The normalized efficiency is not limited by the fundamental linewidth, since the calculated FWHM spectral acceptance bandwidth (0.082 nm) of the 30-mm crystal using Sellmeier equations [52] is much wider than the laser linewidth (12.5 MHz).

We also observed that the extrapolated efficiency curves for all pump powers up to 30 W has a clear peak near ξ ~2.84, corresponding to the theoretical prediction

for optimum SHG in the cw (or long-pulse) limit [45], as shown in the Fig. 7.22. This observation implies that the theoretical prediction for the optimum SHG in the cw operation does not depend upon the thermal effects arising from crystal heating at high-powers.

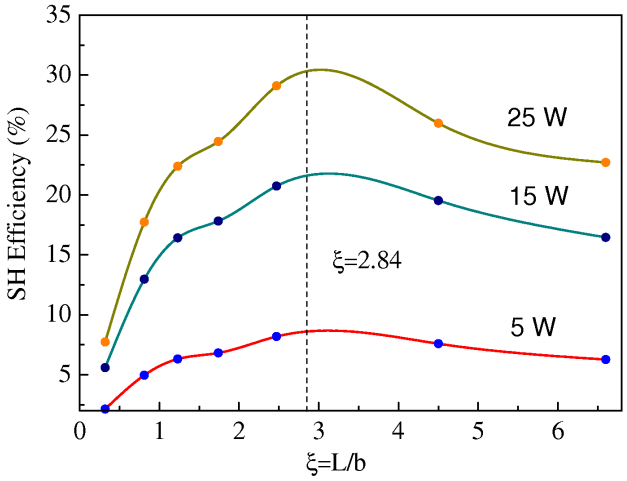

Figure 7.22: Maximum SH efficiency as a function of the focusing parameter L/b for various fundamental power levels, showing a clear peak near (L/b~2.84), as prescribed by Boyd and Kleinman [45].

7.4.2.3 Power scaling and thermal issues

To characterize the power scalability of SHG, we recorded the SHG power and efficiency at ξ=2.48 (w_{op} ~31μm) up to the maximum available fiber laser power, with the results shown in Fig. 7.23. We obtained 9.64 W of green power at the full fundamental power of 29.5 W at a single-pass efficiency of 32.7%. The quadratic increase in the SH power and the corresponding linear variation in the SHG efficiency are maintained up to a fundamental power of 22 W (Fig. 7.23), after which saturation sets in. The saturation effect is also evident from the deviation of the linearity of the SHG power with the square of the fundamental power, in the inset of Fig. 7.23, and is attributed to the pump depletion, back-conversion and thermal phase-mismatch

effects in the MgO:sPPLT crystal.

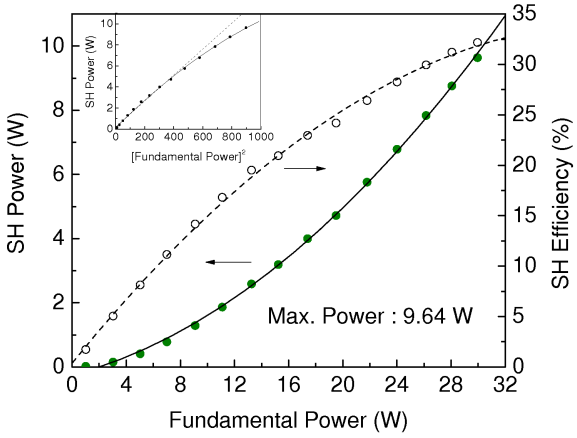

Figure 7.23: Variation of the cw SH power and corresponding conversion efficiency with the fundamental power. Inset: Variation of the SH power as a function of square of the fundamental power.

To verify the contribution of the fundamental depletion and back-conversion to the saturation effect, we chopped the fundamental beam at a frequency of 530 Hz, with 5.5% duty cycle, in order to characterize the SH output without thermal effects, with the results shown in Fig. 7.24. We observed a quadratic variation of the generated average green power and corresponding linear variation of the conversion efficiency up to the highest fundamental power, showing no sign of saturation. In the inset of Fig. 7.24, the linear variation of average SHG power with the square of fundamental power, as expected, also implies the saturation effect is only due to the thermal phase-mismatch effects in the MgO:sPPLT crystal.

For further evidence of the saturation effect due to heat-induced phase-mismatching, we measured the generated green power with the fundamental power for two different thermal management schemes:

Scheme (a): Crystal is heated from three sides including bottom side, with the top side covered with Teflon to prevent the dissipation of the heat generated in the crystal due the absorption of light

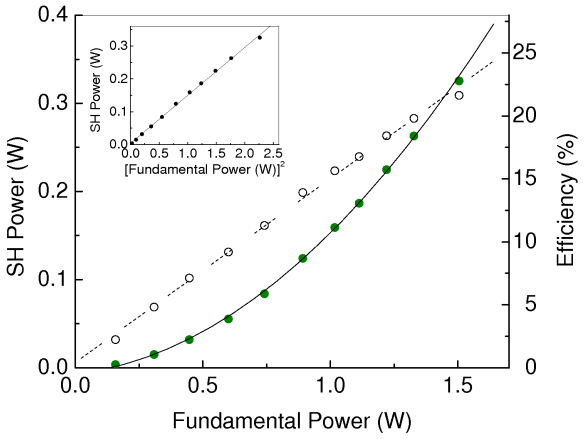

Figure 7.24: Variation of the quasi-cw SH power and corresponding conversion efficiency with average fundamental power. Inset: SH power as a function of square of the average fundamental power.

Scheme (*b*): Crystal is heated from two sides including bottom side, top side is open to air for heat dissipation and the other side was covered with Teflon.

As evident in Fig. 7.25, the generated green power is almost equal in both thermal management schemes up to an input pump power of ∼21 W, after which the generated green power is saturated in Scheme (*a*), whereas it still increases in the Scheme (*b*) with the increase in fundamental power. Due to the closed heating configuration, the heat generated due to light absorption in Scheme (*a*) is not dissipated in air. As a result, a temperature gradient is created in the crystal along the light propagation direction, which limits the effective interaction length of the crystal. In case of Scheme (*b*), as the top side of the crystal is open to air, the generated heat desipated in the air easily and thus generating a weaker temperature gradient along the length of the crystal. Hence, further increases in the green power is possible with the proper thermal management of the crystal.

We also recorded the decrease in the optimum phase-matching temperature at a rate of 0.08 °C/W in cw pumping at fundamental powers beyond 10 W, as shown in Fig 7.26, whereas we observed no change in the phase-matching temperature at all

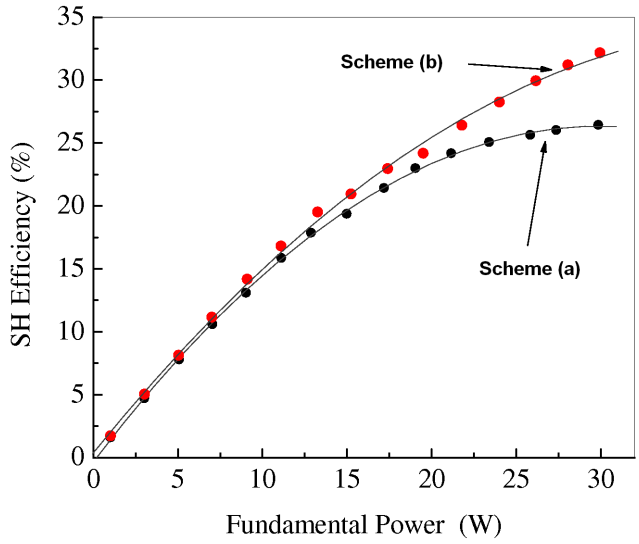

Figure 7.25: Dependence of the generated green on the incident fundamental power at two different thermal management schemes.

power levels in quasi-cw pumping, signifying that the thermal effects are due to the absorption of both the fundamental and generated SH green power. We believe that further increases in the SH power beyond 9.64 W will be possible using a pump beam waist ∼29 μm (ξ=2.84) and improved thermal management to overcome saturation.

7.4.2.4 Single-frequency-stability

The transmission spectrum of the generated green at the highest power of 9.64 W, monitored through a confocal scanning interferometer (FSR = 1 GHz, Finesse ∼400), is shown in Fig. 7.27, confirming reliable single-mode operation with an instantaneous linewidth of ∼6.5 MHz. Similar behavior was observed throughout the pumping range with the same instantaneous linewidth, confirming robust single-mode operation at all fundamental powers.

The frequency-stability of the generated green, measured at 9.64 W using a wavemeter (High Finesse, WS/U-30), is shown in Fig. 7.28. Under free-running conditions and in the absence of thermal isolation, the green output exhibits a

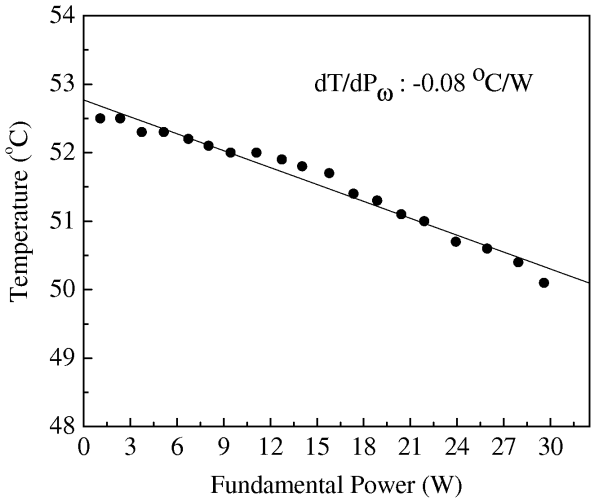

Figure 7.26: Dependence of the phase-matching temperature on fundamental power for MgO:sPPLT crystals.

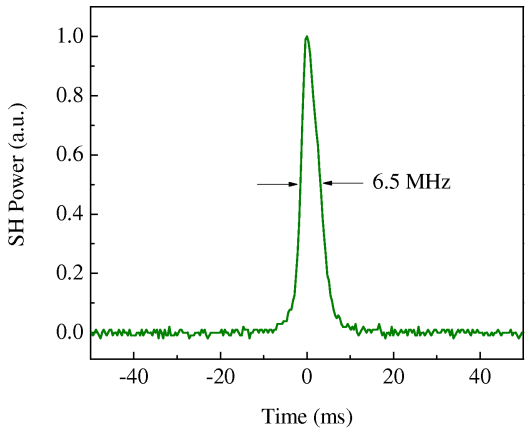

Figure 7.27: Single-frequency spectrum of the green output recorded by a scanning Fabry-Perot interferometer.

peak-to-peak frequency fluctuation <115 MHz over 90 minutes, with a short-term stability of 32 MHz over 30 minutes. This compares to a frequency-stability of 2.2 GHz over 40 minutes measured for a commercial cw frequency-doubled Nd:YVO_4 laser at 532 nm (Coherent, Verdi-10) in our laboratory, as evident in Fig. 7.29.

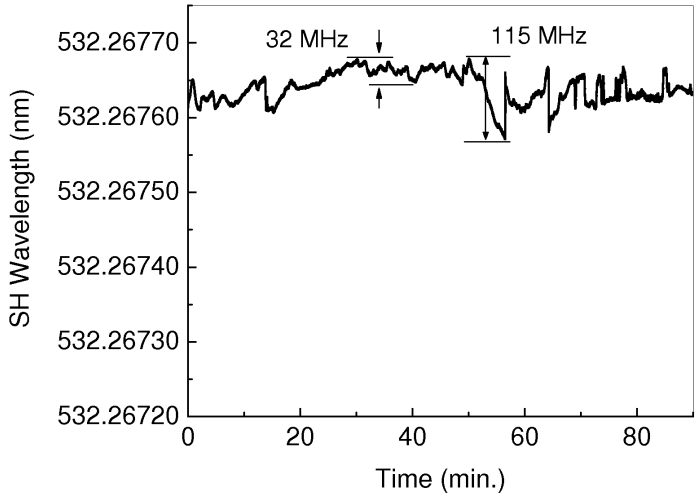

Figure 7.28: Frequency-stability of the SH green beam at 9.64 W over 90 minutes.

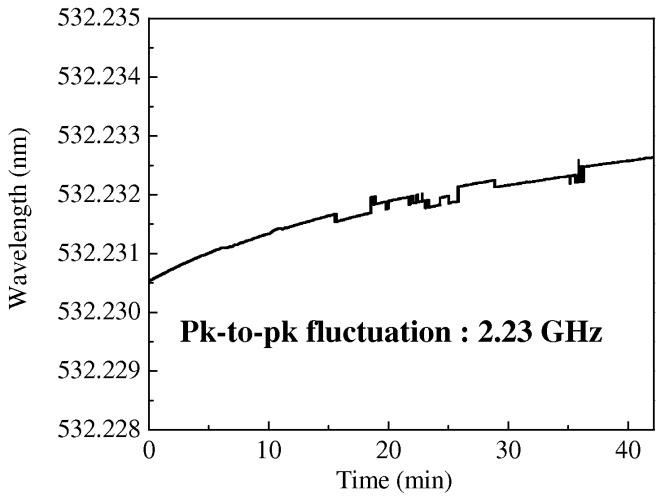

Figure 7.29: Frequency-stability of the output green radiation from a commercial Verdi-10 laser at 10 W over 40 minutes.

7.4.2.5 Power stability

The power stability and spectral output near the maximum green power of 9.64 W are shown in Fig. 7.30. Under free-running conditions and in the absence of thermal isolation, the green power exhibits a peak-to-peak fluctuation of 7.6% over the first 8 hours and 9% over 13 hours. This power fluctuation is attributed mainly to the change in the laboratory environment. No evidence of the output power and beam quality degradation for repeated and continuous operation of the device over 13 hours implies the absence of photorefractive damage of the MgO:sPPLT crystal at high-power visible radiations. Further improvements in green power stability, below 3%, are expected through improved thermal isolation and better temperature control.

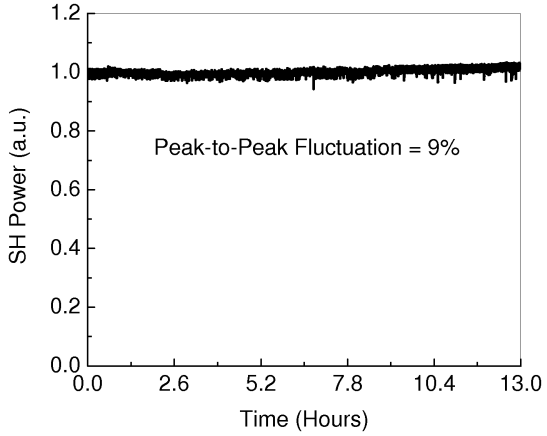

Figure 7.30: Power stability of the cw green source over 13 hours.

7.4.2.6 Beam profile

The far-field energy distribution of the green output beam at 9.64 W together with the intensity profile and the Gaussian fits, generated at 30 W of input power, are shown in Fig. 7.31. Although the beam profiles confirm TEM_{00} spatial mode, full confirmation requires M^2 value measurements.

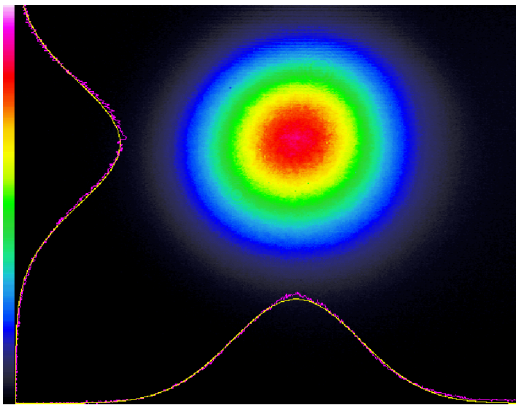

Figure 7.31: TEM_{00} energy distribution, beam profiles (pink curves), and Gaussian fits (yellow curves) of the generated green beam in the far-field at 9.64 W.

Using a f=25 cm focal length lens and scanning beam profiler, we measured M^2 values of the beam of different green power generated at different input pump powers as shown in Fig. 7.32. The measured M^2 of the green radiation of power 9.64 W to

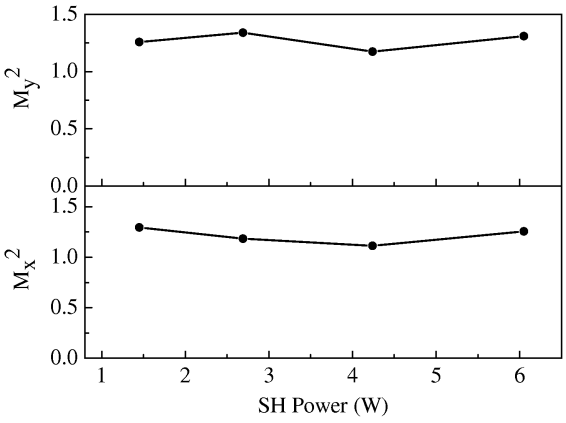

Figure 7.32: Variation of M^2 values of the generated green radiation at different powers.

be $M_x^2 \sim 1.29$ and $M_y^2 \sim 1.23$ with an ellipticity ~0.96, confirming TEM_{00} spatial mode. As evident in Fig. 7.32, the green output beam at different powers shows a similar M^2-values, with a small variation in M_x^2 from 1.11 to 1.29 and M_y^2 from 1.17 to 1.33.

7.5 Conclusions

In this Chapter, we have demonstrated efficient, high-power, narrow-linewidth, green sources in compact and practical design using single-pass SHG of the high-power solid-state and fiber lasers using PPKTP and MgO:sPPLT as nonlinear crystals. Frequency-doubling of the tunable thin-disk solid-state Yb:YAG laser in the PPKTP crystal has generated single-frequency green radiation tunable across 511.9−517.3 nm with a maximum cw power of 1.2 W at 8.8% single-pass conversion efficiency.

Further enhancement of the generated green power is achieved by single-pass SHG of a 30-W Yb fiber laser in a 17-mm-long PPKTP crystal, resulting a 6.2 W green radiation at 532 nm in spatial beam profile (M^2 <1.33) at 30 W of fundamental power with a single-pass conversion efficiency as high as 20.8%. We have measured the effective nonlinear coefficient of the PPKTP crystal along with its absorption losses at both the fundamental and SH wavelengths and have addressed all thermal issues resulting in PPKTP crystal at high-power operation. However, the strong thermal effects at high fundamental power and low thermal conductivity of PPKTP crystal has restricted its stable operation to the fundamental powers below 20 W.

Hence, for high-power operation, the alternative nonlinear crystal, MgO:sPPLT, has been deployed. Using a 30-mm-long crystal, we have generated 9.6 W of cw, single-mode radiation at 532 nm with a conversion efficiency as high as 32.7% using simple, single-pass SHG of a cw, single-frequency Yb fiber laser near room-temperature. This source exhibits a natural peak-to-peak power stability better than 9% over 13 hours with an instantaneous linewidth of 6.5 MHz and frequency-stability better than 32 MHz over 30 minutes. We have generated green output beam with TEM_{00} spatial profile with M^2 <1.33 at all fundamental powers. With more stringent thermal control and optimized focusing, further improvements in green power and efficiency as well as power scaling are feasible. We have observed

no deterioration in the output power and spatial beam quality during repeated measurements and with continuous operation over 13 h, confirming stable power and robust TEM_{00} spatial mode, making the device particularly attractive as a pump source for cw SROs as well as cw and mode-locked Ti:sapphire lasers.

Chapter 8

Fiber-laser-based, green-pumped cw SRO

This Chapter constitutes with the following journal publication:

1. *Continuous-wave, singly-resonant optical parametric oscillator pumped by fiber-laser based green source at 532 nm*
   G. K. Samanta, S. Chaitanya Kumar, Ritwick Das, and M. Ebrahim-Zadeh
   Optics Letters (Communicated) 2009.

8.1 Motivation

Continuous-wave SROs have had profound impact in the field of laser technology due to their wide wavelength tunablity and narrow linewidth radiation from a single compact source. Before the development of quasi-phase-matched nonlinear materials, operation of cw SROs were difficult due to the high oscillation thresholds (typically several watts) in birefringent nonlinear crystals [6]. The major breakthrough in the cw SRO technology came due to the advent of periodically-poled materials, in particular PPLN [7], where high effective nonlinearity and long interaction length of the materials used to bring the operating threshold of the SROs within the limit of watts [60].

The onset of photorefractive damage under exposure to visible radiation has lim-

ited high-power operation of the MgO:PPLN mainly to the near- and mid-infrared. On the other hand, MgO:sPPLT is an alternative material for high-power frequency conversion under visible pumping because of its increased resistance to photorefractive damage. Due to relatively low effective nonlinearity (d_{eff} ~10 pm/V) of the MgO:sPPLT crystal, the cw SRO based on MgO:sPPLT crystal has higher oscillation threshold [13; 58; 70] compared to PPLN based cw SRO [60].

At the same time, for further progress in cw SRO technology, it is imperative to devise new strategies and improved architectures capable of reducing system complexity and cost, while maintaining or enhancing the device performance with regard to all important operating parameters. A major step in this direction is the deployment of more simplified and cost-effective pump sources based on the rapidly advancing fiber laser technology to replace the more complex and relatively expensive cw solid-state laser pump sources which have been predominantly used to date. This approach has already been extensively demonstrated by using cw fiber-laser-based pump sources at 1064 nm in combination with PPLN [89–91], providing high-power, single-frequency, cw radiation with wide tunability in the near- and mid-IR. However, extension of cw fiber laser technology to the green, necessary for pumping visible and near-IR (<1 μm) cw SROs based on, for example, MgO:sPPLT has so far not been possible, because of the difficulty in generating sufficient cw pump power with the required characteristics to drive the SRO. As, a result the realization of cw SROs, till date, using MgO:sPPLT crystal pumped in the visible [13; 58; 70] were only possible using commercially available, relatively expensive intracavity frequency-doubled solid-state green sources (e.g. Verdi 10, Coherent), due to the scarcity of alternative high-power source.

We have developed a compact high-power green source at 532 nm by frequency-doubling of a high-power cw fiber laser at 1064 nm, in a simple and compact experi-

mental design as described in Section 7.4 and reported in [92]. Using such a source, we have developed a high-power, single-frequency cw out-coupled SRO (OC-SRO) based on MgO:sPPLT crystal, pumped in the green by a frequency-doubled fiber laser, as described in this Chapter.

8.2 Experimental configuration

The schematic of the cw OC-SRO is shown in Fig. 8.1. A single-frequency, cw Yb fiber laser (IPG Photonics, YLR-30-1064-LP-SF) at 1064 nm, delivering power up to 30 W with a measured instantaneous linewidth of 12.5 MHz [93], and a frequency-stability of <120 MHz over 1 hour and <50 MHz over 30 minutes, is frequency-doubled into the green to pump the OC-SRO. A convex lens (L_1) of focal length f=17.5 cm is used to focus the fundamental beam at the center of the nonlinear crystal to a beam waist of 31 μm. The nonlinear crystal is a 30-mm-long MgO:sPPLT (HC Photonics Corporation, Taiwan), containing a single grating (Λ=7.97 μm), and housed in an oven with a temperature stability of $\pm$0.1 °C. A dichroic mirror, M, coated for >99% reflectivity at 1064 nm and >94% transmission at 532 nm, separates the generated green from the input fundamental. At the highest available fundamental power of 29.5 W at the input of the crystal, the green source can deliver cw, single-frequency output power up to 9.64 W at 532 nm with a conversion efficiency as high as 32.7% in a TEM_{00} spatial profile with peak-to-peak power stability of 9% over 13 hours and frequency-stability <32 MHz over 30 minutes [92].

For reliable operation of our green source, we operated it at the highest power level and varied input green power to the OC-SRO using a power attenuator comprising a half-wave-plate and polarizing beam-splitter cube. A second half-wave-plate was used to yield the correct pump polarization for phase-matching relative to the

crystal orientation. The OC-SRO is configured in a compact ring cavity comprising two concave mirrors, M_1 and M_2, of radius of curvature r=100 mm, and two plane reflectors, M_3 and M_4. Mirrors M_1, M_2, and M_3 have high reflectivity (>99.5%) over the signal wavelength range of 800−1100 nm, where as mirror M_4, which is an output-coupler (OC), has varying transmission (T=0.71%−1.1%) across the signal wavelength range. All mirrors have high transmission (T=85−90%) for the idler over 1100−1400 nm, thus ensuring SRO operation. A convex lens (L_2) of focal length f=15 cm is used to focus the pump at the center of the crystal. The angle of incidence on the concave mirrors, M_1 and M_2, is limited to ∼5° to minimize astigmatism. A plane mirror, M_5, with characteristics identical to cavity mirrors and also high reflecting (>99%) at 532 nm, is used as a cutoff filter for the signal and any residual pump, to enable measurements of the idler output. The pump beam waist at the center of the crystal is ∼30 μm, corresponding to a signal beam waist ∼40 μm at 900 nm. The nonlinear crystal for SRO is identical to the crystal used for SHG into the green. It is 1 mol.% bulk MgO:sPPLT, 1-mm-thick, 2.14-mm-wide, and 30-mm-long, with a single grating period of (Λ=7.97 μm), as described in Chapters 4 and 5. The crystal temperature is similarly controlled using an oven with a stability of ±0.1 °C and maximum operating temperature of 250 °C. The crystal faces are antireflection coated (R<1%) over 800−1100 nm, with high transmission (T>98%) at 532 nm. The residual reflectivity of the coating over the idler range of 1100−1400 nm is 1%−15%. For frequency selection, a 500-μm-thick uncoated fused silica etalon (FSR =206 GHz, Finesse ∼0.6) is used at the second cavity waist between M_3 and M_4. The total optical length of the cavity including the crystal and etalon is 711 mm, corresponding to a FSR∼422 MHz.

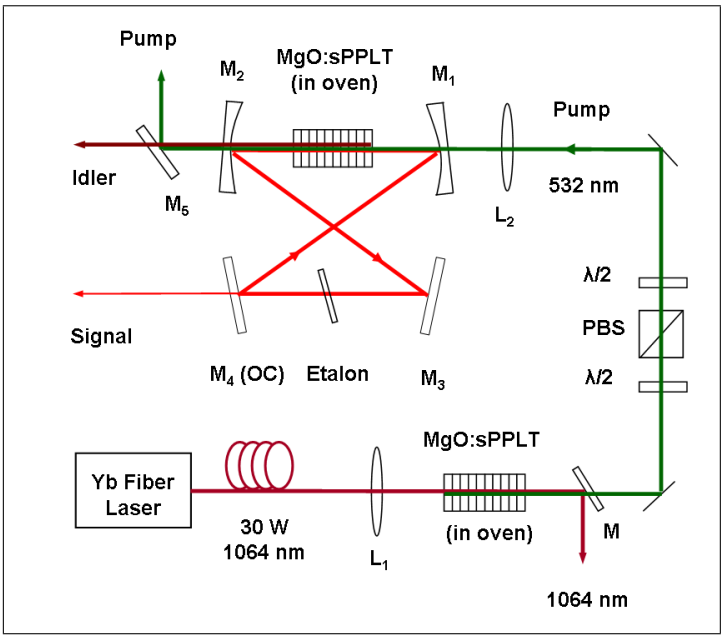

Figure 8.1: Schematic of the experimental design of MgO:sPPLT based cw OC-SRO. HWP, half-wave-plate; PBS, polarizing beam-splitter; M, mirror, L; lens.

8.3 Results and discussions

8.3.1 Power across the tuning range of OC-SRO

The extracted signal and idler output power across the tuning range of the OC-SRO, varying the crystal temperature from 59 °C to 236 °C (as shown in Section 4.2.3.1 and also reported in [58]) in 3 °C temperature interval, is shown in Fig. 8.2. Although our SHG source provides maximum green power of 9.64 W as shown in Section 7.4.2.3 and in [92], the available pump power at the input to the cw OC-SRO crystal was limited to 7.3 W, due to the unoptimized optics used to deliver pump beam to the OC-SRO. The coupled-out signal power, as shown in Fig. 8.2 (a), varies from 725 mW at 1000 nm (59 °C) to 277 mW at 855 nm (236 °C) towards the extreme of the tuning range, with a maximum of 800 mW at 927 nm (122 °C) due to the optimum coupling of 1.04% [88]. Correspondingly, the idler power varies from 1.9 W at 1136 nm (T=59 °C) to 745 mW at 1408 nm (236 °C) with a maximum

power of 2.1 W at 1168 nm (74 °C), as shown in the Fig. 8.2 (b). As evident in the Fig. 8.2 (b), the idler power is nearly constant at ∼1.8 W in the wavelength range of 1136 nm to 1252 nm, which is 42% of the total idler tuning range, and monotonically decreasing towards the extreme of the tuning range due to different factors, including thermal lensing at higher crystal temperatures and higher pump powers, as discussed in Chapters 4 and 5, and also reported in [58; 70]. Unlike

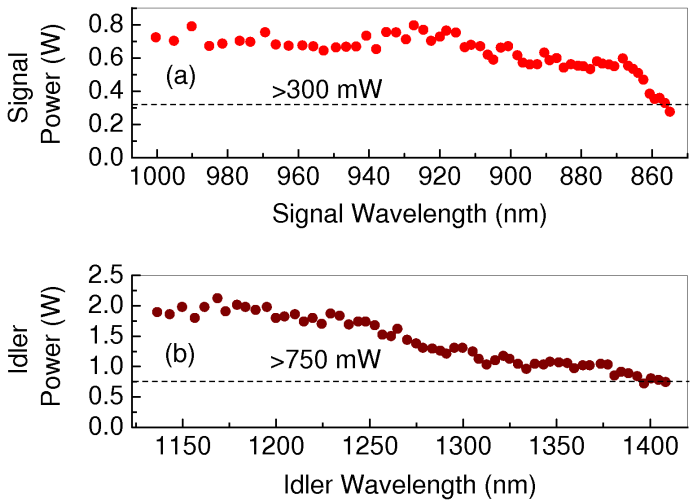

Figure 8.2: (a) Extracted signal power, and (b) idler output power, across the tuning range of OC-SRO.

our previous report on OC-SRO [88], here we generate more than 745 mW of idler power throughout the entire tuning range, which is 1.5 times higher than before [88], and simultaneously coupled out a signal power in excess of 300 mW throughout the entire signal tuning range. The enhancement of the idler power can be attributed to the reduction of pump and intracavity signal power density, and hence the thermal effects due to the loose focusing of the pump. Further enhancement of the signal and idler power throughout the entire tuning range can be achieved with increased input power to the OC-SRO [88] using optimized optics, and at the same time reducing the thermal effect with loose focusing. The pump depletion of the OC-SRO remains

close to ∼55% over most of the tuning range, before declining to ∼34% at the extreme of the tuning range.

8.3.2 Signal and idler power-stability of the OC-SRO

We have recorded the power stability of the out-coupled signal at 971 nm and corresponding idler at 1176 nm for a crystal temperature of 80 °C, as shown in Fig. 8.3. As evident in the Fig. 8.3 (a), the signal power exhibits slightly better peak-to-peak power fluctuation (10.7%) than idler power, which has peak-to-peak power fluctuation of 11.7% (Fig. 8.3(b)) over 40 minutes. The power instability of the signal and idler can be attributed to the green pump power fluctuation, which is measured to be ∼8% [92], and also due to the thermal effects of the nonlinear crystal. Therefore, further improvement of the power stability of the signal and idler can be possible with higher pump power stability along with reducing the thermal effects of the nonlinear crystal using loose pump focusing.

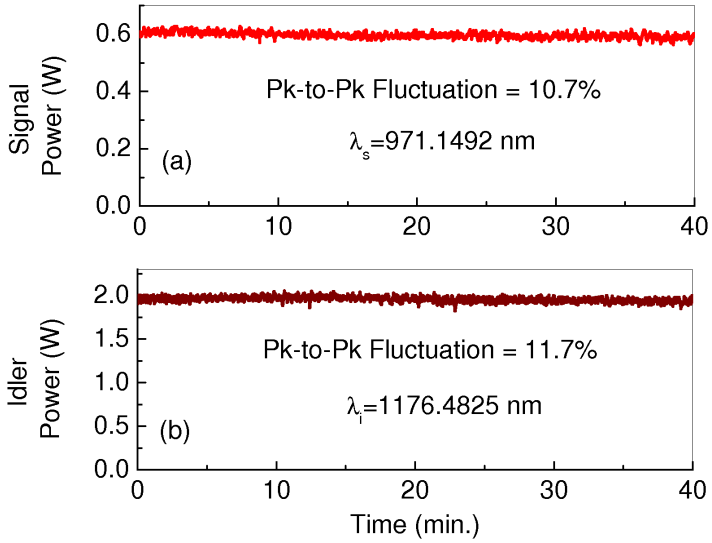

Figure 8.3: Power stability of (a) out-coupled signal and (b) idler over 40 minutes. The crystal temperature is 80 °C.

8.3.3 Signal-frequency-stability of the cw OC-SRO

The frequency-stability of the out-coupled signal radiation at 971 nm for a crystal temperature of 80 °C, measured using a wavemeter (High finesse, WS/U-30), is shown in Fig. 8.4. Under free-running conditions, the signal output exhibits a peak-to-peak frequency fluctuation <75 MHz over 15 minutes. As evident in Fig. 8.4, there is a periodic variation of the signal frequency deviation with time. If we zoom in to observe the short-term frequency-stability at any instant of time as shown in the inset of Fig. 8.4, then we can observe that the signal frequency remains stable to better than 10 MHz, (limited by the relative accuracy of the wavemeter) over short period of time (10 seconds) and then shifts to another frequency. This frequency jitter can be attributed to pump frequency jitter, pump and

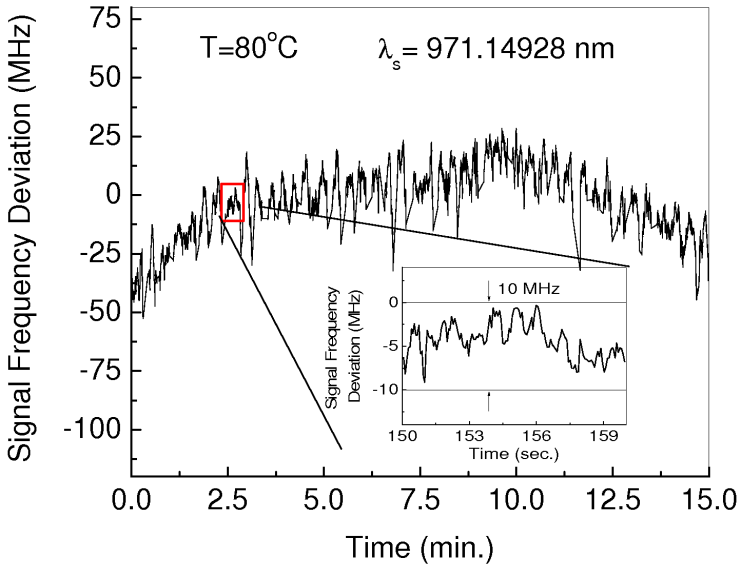

Figure 8.4: Long-term frequency-stability of the signal at wavelength 971 nm for the crystal temperature of 80 °C over 15 minutes, and (inset) short-term frequency-stability over 10 seconds.

intracavity signal induced thermal noise, mechanical vibration of the experimental setup and also jitter of the measurement instrument (wavemeter). Hence, long-term

frequency-stability of the system can be improved with active stabilization along with temperature controller of better temperature stability ($< \pm 0.1$ °C). We have also observed similar signal frequency-stability of the OC-SRO across the tuning range. Due to the limitation of the spectral coverage of our wavemeter, we could not record the frequency-stability of the non-resonant idler. However, we believe that idler will not have better frequency-stability than signal due to the frequency instability of the pump [92].

8.3.4 Beam profile of the signal radiation

The far-field energy distribution of the signal radiation at 971 nm at a distance > 2 m away from the OC-SRO, together with the intensity profile and the Gaussian fits along the two orthogonal axes, are shown in Fig. 8.5. Although the data

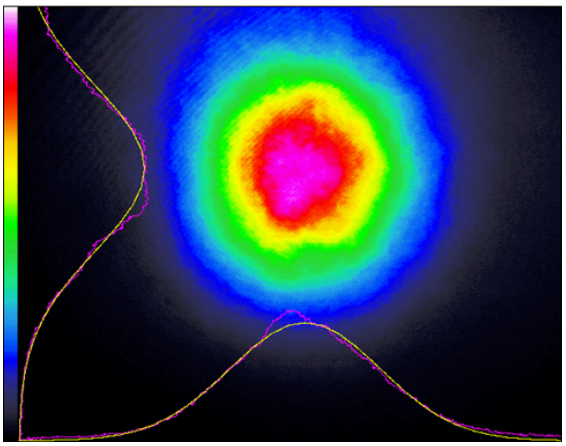

Figure 8.5: Far-field TEM_{00} energy distribution and intensity profiles of the generated signal beam at crystal temperature 80 °C (971 nm) recorded at a distance 2 m away from OC-SRO

appear to confirm a Gaussian distribution, we measured, using a focusing lens of 25-cm focal length and scanning beam profiler, the M^2 of the signal radiation and corresponding idler radiation. Operating the OC-SRO at the highest available input power, we have measured the M^2-value of the signal and the idler at five different

crystal temperatures starting from 80 °C to 200 °C in 30 °C temperature intervals, as shown in Fig. 8.6. The M^2 of the signal radiation increases from $M_x^2 \sim 1.13$, $M_y^2 \sim 1.13$ at 80 °C (971 nm) to $M_x^2 \sim 1.52$, $M_y^2 \sim 1.47$ at 200 °C (874 nm), where as the M^2 of the corresponding idler radiation across the tuning range is comparable to M^2 of the pump ($M_x^2 \sim 1.28$, $M_y^2 \sim 1.24$), with a small variation in M_x^2 from 1.26 to 1.18 and M_y^2 from 1.26 to 1.12. The increase in M^2 value of the signal radiation with the crystal temperature signifies the thermal lensing effect of the OC-SRO at higher crystal temperatures [70].

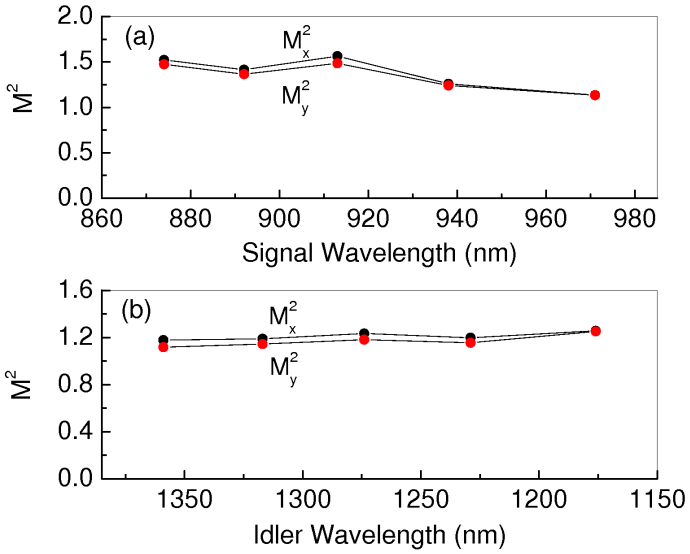

Figure 8.6: Variation of M^2 for (a) signal, and (b) idler across the tuning range of the OC-SRO

8.4 Conclusions

In conclusion, we have demonstrated a cw OC-SRO based on MgO:sPPLT, providing continuously tunable radiation across 855−1408 nm, pumped in the green by external single-pass frequency-doubling of a cw Yb-fiber laser. The non-resonant idler output of the OC-SRO exhibits a maximum power up to 2 W in a TEM_{00} spatial

mode (M^2 <1.26), with a peak-to-peak power stability <11.7% over 40 minutes. Optimum output coupling (T=1.04%) of the resonant signal of the cw OC-SRO provides single-frequency signal radiation up to a power of 800 mW, with a peak-to-peak power stability <10.7% over 40 minutes. in a TEM_{00} spatial mode with M^2 <1.52. Without any active stabilization, the resonant signal exhibits a natural long-term frequency-stability <75 MHz over 15 minutes. and short-term frequency-stability <10 MHz over 10 seconds. With increased pump power to the OC-SRO using optimized optics and reduced thermal lensing with loose pump focusing, further improvements in the output power of the OC-SRO across the tuning range are feasible. Simultaneous, stable, single-frequency operation and high output power performance over a tuning range of 553 nm in good spatial beam quality, make the OC-SRO an attractive source particularly for high-resolution spectroscopic applications.

Chapter 9

Summary and outlook

In this thesis, we have demonstrated high-power, single frequency, visible pumped cw laser sources with wide tunable emission (580 nm) in the near-IR (across 848−1430 nm), using singly resonant optical parametric oscillators with a single tuning parameter (temperature). The minimum oscillation threshold of such devices is about 2.84 W and generate output powers typically from 750 mW to 2.59 W across the wavelength range from 1167 nm to 1427 nm with a peak-to-peak power stability <11.7% over 40 minutes. A finite out-coupling of the narrow linewidth (∼3 MHz) resonating signal of the SRO extends the tuning range down to 848 nm with practical output powers as much as 1.23 W with a peak-to-peak power stability of <10.7% over 40 minutes for high resolution spectroscopic applications. The sources exhibit a total extraction efficiency as high as 40% and have a diffraction limited output beam in TEM_{00} spatial mode (M^2 <1.26). Without any active stabilization, the resonating signal exhibits a mode-hop-free oscillation with natural frequency-stability <10 MHz over 10 seconds, limited by the absolute accuracy of the wavemeter used.

We also have demonstrated a practical solid-state laser source tunable across the 425−489 nm spectral range in the blue. This is to our knowledge by far the broadest tuning range of any cw source in the blue. It employs the intracavity frequency-

doubling of the near-IR cw SRO. The source exhibits high output power of up to 1.27 W in spatial beam quality over the entire tuning range in the blue region with additional optical radiation with practical power >100 mW over 850−915 nm wavelength range, with 970 mW at 900 nm, and high-power up to 2.6 W across the wavelength range of 1167−1422 nm. The blue source exhibits mode-hop-free, single-frequency (linewidth ∼8.5 MHz) radiation with a natural frequency stable better than 280 MHz, limited by the resolution of the wavemeter.

We have demonstrated three narrow linewidth, cw, green sources in a compact and practical design using the single-pass SHG of a high-power cw solid-state laser and a fiber laser in PPKTP and MgO:sPPLT nonlinear crystals. One of the green sources is tunable across 511.9−517.3 nm with a maximum cw power of 1.2 W by frequency-doubling of the tunable thin-disk solid-state Yb:YAG laser in PPKTP, while the other two green sources exhibit high-green powers of 6.2 W and 9.6 W at 532 nm with single-pass frequency-doubling of the high power fiber laser in PPKTP and MgO:sPPLT, respectively. These are to the best of our knowledge by far are the highest powers at 532 nm available using these crystals. The green source of power 9.6 W exhibits a natural peak-to-peak power stability better than 9% over 13 hours with an instantaneous linewidth of 6.5 MHz with frequency-stability <32 MHz over 30 minutes and nearly-diffraction-limited TEM_{00} spatial profile with M^2 <1.33, making the device particularly attractive as a pump source for cw SROs as well as for cw and mode-locked Ti:sapphire lasers. Using this green source, we have also verified the reliable operation of a cw SRO.

As a direction of the future work, the performance of the SRO in terms of power-stability, frequency-stability and output power across the signal wavelength range can further be improved by proper thermal management of the device heating effects due to pump and signal absorption, active stabilization of the cavity length and

using optimum output coupling of the intracavity signal of the SRO. The demonstrated tuning range of the blue is limited by the grating period of the MgO:sPPLT crystal, and so can be extended to cover the entire range of 300−530 nm using alternative gratings. The use of other grating periods will also enable blue generation at lower temperatures, reducing the effects of thermal lensing, and thus extending the higher powers to the shorter wavelengths. Moreover, by resonating the idler wave in the 1140−1420 nm range, tunable generation across the 570−710 nm will also be possible, making this a promising approach for the generation of high-power, widely tunable, cw radiation across the 300−700 nm spectral range. Using walk-off compensation schemes, we can use longer crystals and hence we can further increase the blue powers. The output green power of the SHG source can also be increased further by proper thermal management of the crystal heating effects. Such a high power green source can be use to develop cw and mode-locked Ti:sapphire lasers.

Appendix A

Measurement of crystal absorption

The schematic of the experimental setup for the measurement of the crystal absorption is shown in Fig. A.1. In this simple experimental setup, we can measure (1) reflection loss at the crystal faces, (2) linear absorption and two-photon absorption (TPA) of the nonlinear crystal at both the wavelengths, (3) green-induced infrared absorption (GRIIRA), (4) photorefraction, and (5) the thermal lensing effect of the nonlinear crystal. Here, both the green (532 nm) and the infrared (1064 nm) light were propagated along the length of the crystal and made to overlap inside the crystal, so that the change of infrared absorption in the presence of green light can be monitored. Mirror, M_1, having high reflectivity at 532 at an angle of incidence of 45° and high transitivity at 1064 nm, is used to combine both the beams. Mirror M_2 also has the same coating specification as M_1, and is used to separate the beams to monitor them individually. As GRIIRA and TPA effects depend up on power density, we have used an achromatic lens (L_1) to focus both the beams at the center of the crystal. The beam waists are maintained similar to that of the optical parametric oscillator (OPO) experiments (Chapters 4, 5, 6, and 8) and also to that of the SHG experiments (Chapter 7) to verify the contribution of GRIIRA and TPA of the crystal in those experiments. The infrared beam was focused to a

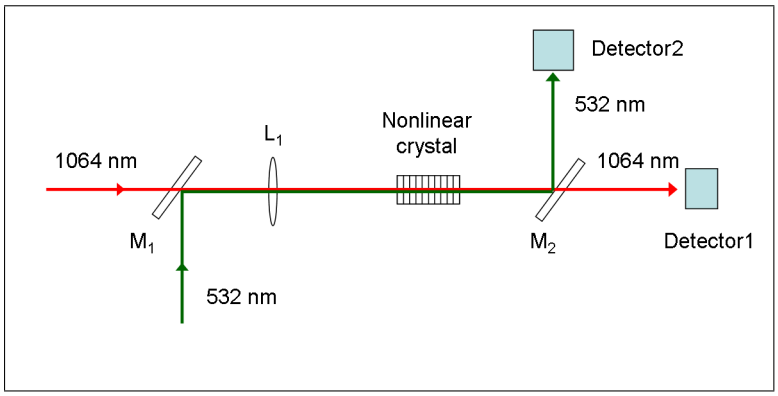

Figure A.1: Schematic diagram of the experimental setup for GRIIRA, linear absorption loss, two photon absorption, and thermal lensing measurements

waist radius of 28 μm and green beam to a waist radius of 34 μm. The infrared power was varied to a maximum of 30 W, resulting a maximum power density of 2.4 MW/cm^2. Similarly, maximum available green power is 9 W resulting a power density of 0.49 MW/cm^2. To measure the linear absorption and TPA we recorded transmitted power with the increase of input power for both the beams separately. For accurate measurement of the absorption losses of the crystal, we have considered the reflection loss of the crystal faces. To measure the reflectivity of the crystal faces, we tilted the crystal faces slightly to record the reflected power out of incident beam direction and recorded the reflected power with the increase of input power.

The typical transmission characteristics of the MgO:sPPLT crystal is shown in Fig. A.2 at 1064 nm and 532 nm. Using the transmission data of from Fig. A.2, along with Beer-Lambert's (Equation (A.1)), we calculated the absorption coefficient of MgO:sPPLT crystal to be 8.4×10^{-4}/cm and 0.007/cm at 1064 nm and 532 nm, respectively.

$$\mathbf{I(z)} = \mathbf{I_0} e^{-\alpha c z} \tag{A.1}$$

where $\mathbf{I_0}$ is the incident power, α is the absorption coefficient, c is the concentration of the crystal, and z is the length of the crystal.

The transmitted power in the presence of the TPA can be represented as

$$\mathbf{I(z)} = \frac{\mathbf{I_0}}{1 + \beta c z \mathbf{I_0}} \tag{A.2}$$

where β is the TPA cross-section of the medium. As the transmission data (Fig. A.2) of MgO:sPPLT crystal is linear at both the wavelengths, therefore there is no evidence of the TPA in the crystal at these power densities.

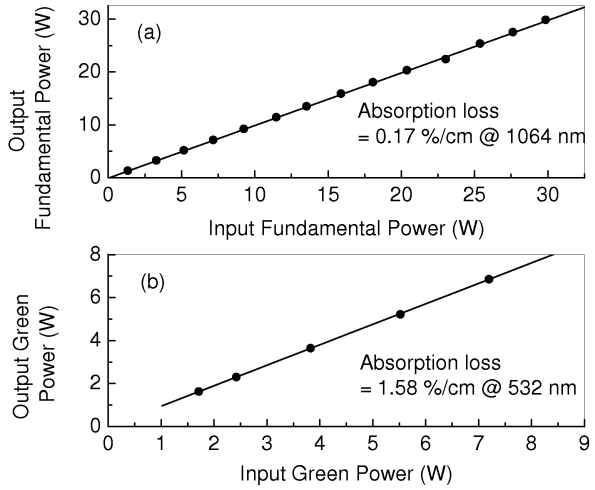

Figure A.2: Linear dependence of the transmitted power with the input power at (a) fundamental (1064 nm), and (b) SH (532 nm) of the MgO:sPPLT crystals, showing no evidence of the TPA.

For GRIIRA measurements, we kept the infrared power fixed (1 W) and increased green power density up to 0.49 MW/cm^2, and correspondingly measured the change in the transmitted infrared power continuously over 10 minutes for each green power density. The transmitted infrared power was measured in the presence and in the absence of green. A mechanical chopper was used to block and unblock the green light to the crystal. The typical example of green-induced infrared absorption and

photorefraction as a function of time for an undoped, nearly-stoichiometric $LiNbO_3$ crystal ([Li]/[Nb] = 0.988) [94] is shown in Fig. A.3. In our experiment, there was no change in infrared power in the presence of green, showing no evidence of GRIIRA at these green power densities. It has been reported that GRIIRA in stoichiometric $LiTaO_3$ is strongly suppressed even without MgO doping, as shown in Fig. A.4 [85].

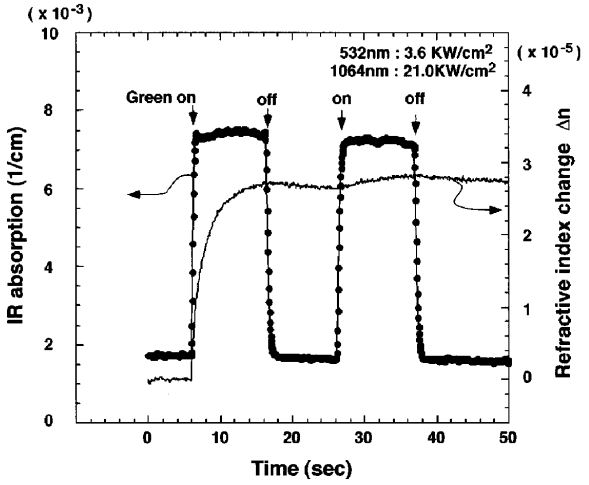

Figure A.3: Example of the change of the infrared absorption and photorefraction by green light irradiation in an undoped nearly stoichiometric $LiNbO_3$ crystal [94].

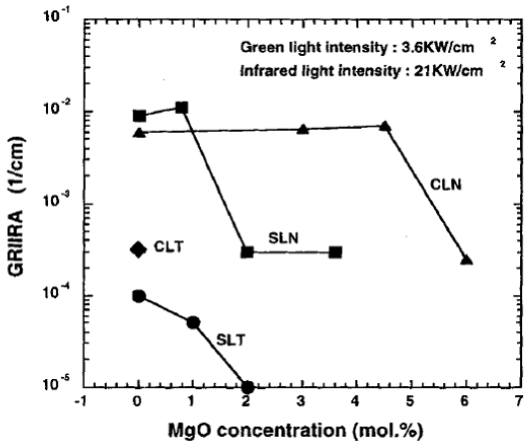

Figure A.4: GRIIRA versus MgO concentration in $LiNbO_3$, and $LiTaO_3$ crystals [85].

For thermal lensing, one beam can be used as the probe beam to monitor the thermal lensing due to other beam (pump beam). The beam diameter of the probe beam is first measured in the absence of pump beam using a beam-profiler at different positions after the crystal, and using ABCD ray matrix we can estimate the initial beam waist at the center of the crystal. Now, as we increase the pump power, thermal lensing will appear due to different absorption mechanisms of the crystal, and as a result focusing position of the probe beam will accordingly change depending on the power of the induced thermal lens. Using the same technique, we measure the beam diameter of the probe, and correspondingly estimate beam waist of the probe beam in the center of the crystal, and hence the power of the thermal lens as a function of pump power.

Appendix B

Measurement of M^2

The operation threshold of the parametric devices depends critically on several properties of the pump laser including the beam quality. Among all of the features of the pump laser, operation threshold of parametric device increases very acutely with the deviation of the beam profile from perfect TEM_{00} (M^2=1) mode. Beside that, optimum cavity design necessitates initial pump beam diameter. Hence, it is useful to measure the beam diameter as well as the M^2 of the laser beam.

Conventionally laser beam diameter is measured using the knife edge technique, where the laser beam is cut in transverse direction and corresponding power is recorded. Differentiating the resulting variation of the transmitted power with the position of the knife edge, the intensity profile of the laser beam can be obtained. Repeating this measurement on both sides of the focused point, and using simple mathematical steps [95], one can obtain M^2 parameter of the laser beam. The resolution of this method is limited only by the accuracy with which the knife edge can be positioned. It also has the advantage that it can be used for high-power lasers. This method is used as the basis for a number of commercial beam-profiling and M^2-measurement devices.

Here, we use a commercially available beam-profiler, which uses a scanning nar-

row slit for beam-profiling. The resolution of this method is limited only by the width of the slit. It also can be used for high-power laser beam profiling.

The schematic of the experimental setup for M^2 measurement is shown in Fig. B.1. To measure the far-field spatial profile, we placed a long focal length (f = 25 cm) convex lens (L_1) at a distance typically >2 meters away from the laser. The beam diameter along two orthogonal axes (X and Y) is measured using a beam-profiler (Nanoscan, PHOTON Inc., USA), which has a rotating narrow slit and pyroelectric detector for high laser power (<1 W). As all high-power lasers work reliably at the highest power level, and as we can not allow entire laser power to the beam profiler, we used a power attenuator comprising a half-wave-plate and a polarizing beam-splitter to reduce the input laser power to the beam-profiler to a power <500 mW.

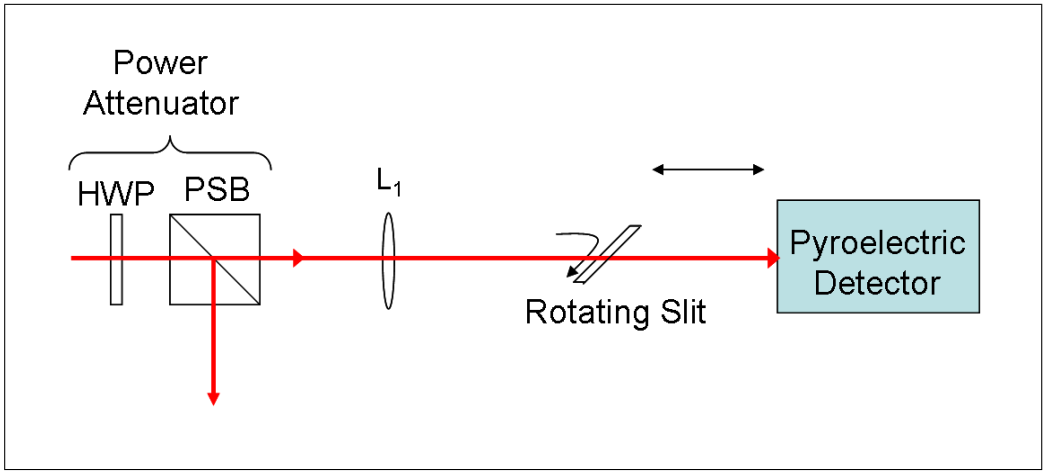

Figure B.1: Schematic diagram of the experimental setup for M^2-value measurement. HWP, half wave-plate, PSB, polarizing beam-splitter.

The typical beam profiles along X and Y directions of a 10-W green laser (Verdi-10, Coherent) recorded using the beam-profiler are shown in Fig. B.2. We have recorded beam diameters along X and Y directions at different positions on both sides of the lens focus, by translating the beam-profiler along the beam is shown in

Fig. B.3.

The formula for M^2 is given as

$$\mathbf{M^2} = \frac{\pi \times D_{min}^2}{2\lambda \times 2Z_r} \tag{B.1}$$

where $Z_r = \mid Z_{max} - Z_{min} \mid /2$ is the Rayleigh length, λ is the wavelength of the laser, D_{min} is the beam diameter at the beam waist, Z_{max} is the distance along the beam propagation where the beam diameter is 1.414× D_{min} ($\sqrt{2}D_{min}$), and Z_{min} is the distance along the beam propagation on the other side of the waist where the beam diameter is 1.414× D_{min} ($\sqrt{2}D_{min}$).

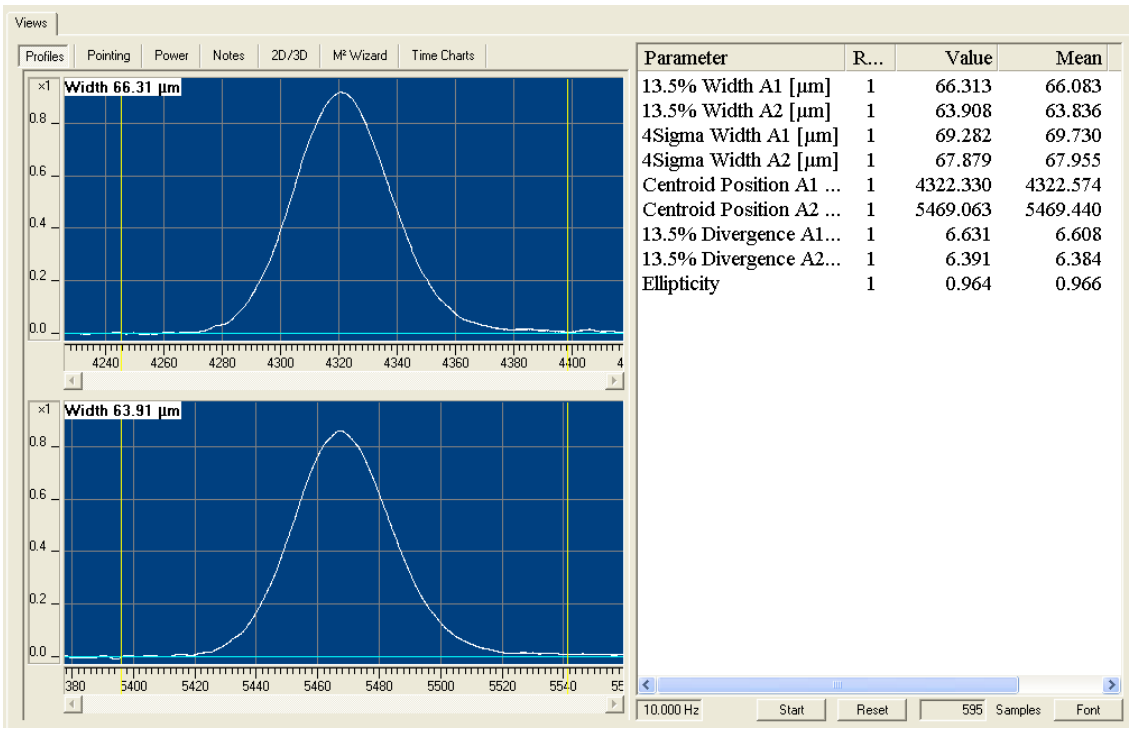

Figure B.2: Typical beam profiles along X and Y directions of a 10 W green laser.

Now, using equation (B.1) and the experimental data as shown in Fig. B.3, we measured M_x^2 ∼1.29 and M_y^2 ∼1.23 for the green pump beam as shown in Section

7.4.2.6.

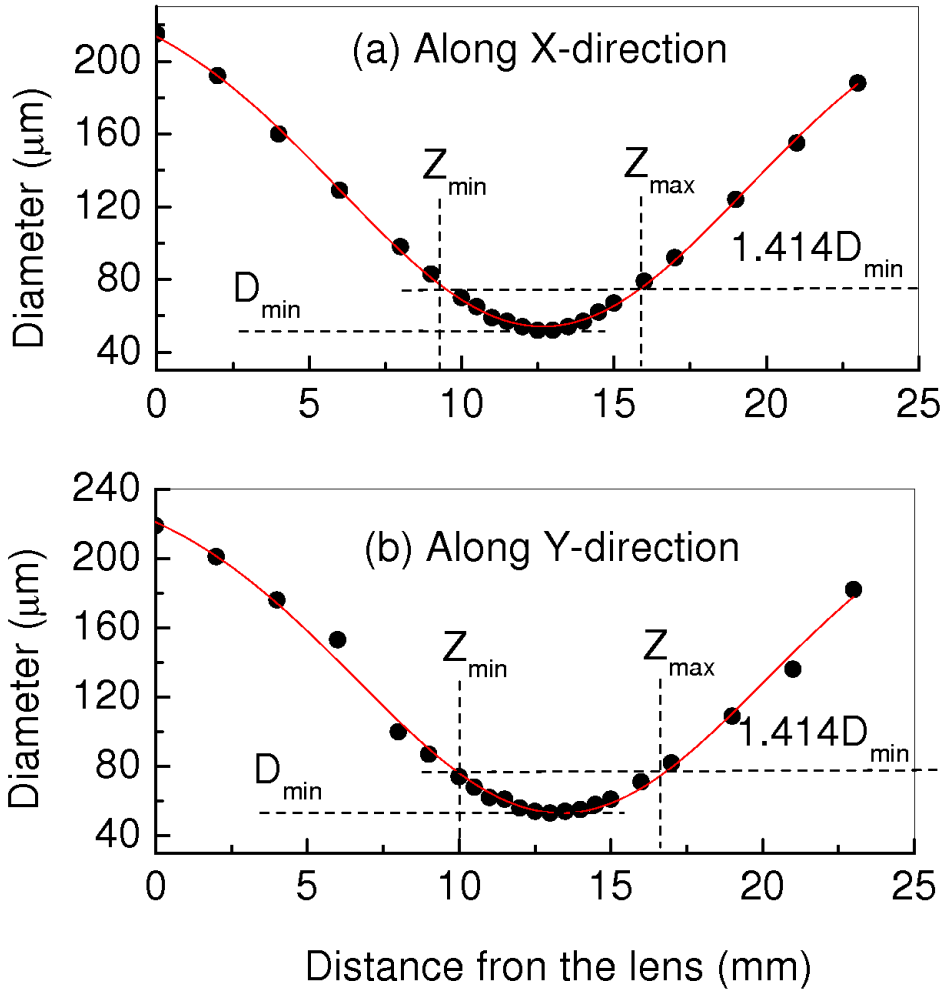

Figure B.3: Beam diameter on both side of the focal point of the lens along (a) X direction and (b) Y direction. Red lines are Gaussian fit to the data.

Bibliography

[1] M. Ebrahim-Zadeh. *Mid-infrared ultrafast and continuous-wave optical parametric oscillators*. Springer, pp. 179–218, 2003.

[2] J. A. Giordmaine and R. C. Miller. Tunable coherent parametric oscillation in $LiNbO_3$ at optical frequencies. *Physical Review Letters*, 14(24):973–976, Jun 1965.

[3] M. Ebrahim-Zadeh and I. T. Sorokina. *Mid-infrared coherent sources and applications, chap. Mid-infrared optical parametric oscillators and applications*. Springer, pp. 347–375, 2007.

[4] M. Ghotbi, A. Esteban-Martin, and M. Ebrahim-Zadeh. BiB_3O_6 femtosecond optical parametric oscillator. *Optics Letters*, 31(21):3128–3130, 2006.

[5] M. Ghotbi, A. Esteban-Martin, and M. Ebrahim-Zadeh. Tunable, high-repetition-rate, femtosecond pulse generation in the ultraviolet. *Optics Letters*, 33(4):345–347, 2008.

[6] S. T. Yang, R. C. Eckardt, and R. L. Byer. Continuous-wave singly resonant optical parametric oscillator pumped by a single-frequency resonantly doubled Nd:YAG laser. *Optics Letters*, 18(12):971–973, 1993.

[7] Walter R. Bosenberg, Alexander Drobshoff, Jason I. Alexander, Lawrence E. Myers, and Robert L. Byer. 93%-pump depletion, 3.5-W continuous-wave, singly resonant optical parametric oscillator. *Optics Letters*, 21(17):1336–1338, 1996.

[8] M. M. J. W. van Herpen, S. E. Bisson, and F. J. M. Harren. Continuous-wave operation of a single-frequency optical parametric oscillator at 4–5 μm based on periodically poled $LiNbO_3$. *Optics Letters*, 28(24):2497–2499, 2003.

[9] P. E. Powers, Thomas J. Kulp, and S. E. Bisson. Continuous tuning of a continuous-wave periodically poled lithium niobate optical parametric oscillator by use of a fan-out grating design. *Optics Letters*, 23(3):159–161, 1998.

[10] J. Henderson and R. Stafford. Intra-cavity power effects in singly resonant cw OPOs. *Applied Physics B*, 85:181–184, 2006.

[11] S. Bahbah, F. Bretenaker, and C. Drag. Single-frequency quasi-continuous red radiation generated by a green-pumped singly resonant optical parametric oscillator. *Optics Letters*, 31(9):1283–1285, 2006.

[12] U. Strössner, A. Peters, J. Mlynek, S. Schiller, J.-P. Meyn, and R. Wallenstein. Single-frequency continuous-wave radiation from 0.77 to 1.73 μm generated by a green-pumped optical parametric oscillator with periodically poled $LiTaO_3$. *Optics Letters*, 24(22):1602–1604, 1999.

[13] Jean-Michel Melkonian, Thu-Hien My, Fabien Bretenaker, and Cyril Drag. High spectral purity and tunable operation of a continuous singly resonant optical parametric oscillator emitting in the red. *Optics Letters*, 32(5):518–520, 2007.

[14] T.-H. My, C. Drag, and F. Bretenaker. Single-frequency and tunable operation of a continuous intracavity-frequency-doubled singly resonant optical parametric oscillator. *Optics Letters*, 33(13):1455–1457, 2008.

[15] P. A. Franken, A. E. Hill, C. W. Peters, and G. Weinreich. Generation of optical harmonics. *Physical Review Letters*, 7(4):118–119, 1997.

[16] T. H. Maiman. Stimulated optical radiation in ruby. *Physical Review Letters*, 187:493–494, 1960.

[17] J. A. Armstrong, N. Bloembergen, J. Ducuing, and P. S. Pershan. Interactions between light waves in a nonlinear dielectric. *Physical Review*, 127(6):1918–1939, 1962.

[18] R. L. Sutherland. *Handbook of nonlinear optics*. Second Edition, Marcel Dekker, Inc., 1996.

[19] R. W. Boyd. *Nonlinear optics*. Second Edition, Academic Press, 2003.

[20] A. Yariv. *Quantum electronics*. Second Edition, John Wiley and sons, New York, 1989.

[21] J. A. Giordmaine. Mixing of light beams in crystals. *Physical Review Letters*, 8(1):19–20, Jan 1962.

[22] P. D. Maker, R. W. Terhune, M. Nisenoff, and C. M. Savage. Effects of dispersion and focusing on the production of optical harmonics. *Physical Review Letters*, 8(1):21–22, Jan 1962.

[23] W. R. Bosenberg, W. S. Pelouch, and C. L. Tang. High-efficiency and narrow-linewidth operation of a two-crystal $\beta - BaB_2O_4$ optical parametric oscillator. *Applied Physics Letters*, 55:1952–1954, 1989.

[24] A. V. Smith, D. J. Armstrong, and W. J. Alford. Increased acceptance bandwidths in optical frequency conversion by use of multiple walk-off-compensating nonlinear crystals. *Journal of the Optical Society of America B*, 15(1):122–141, 1998.

[25] L. E. Myers, R. C. Eckardt, M. M. Fejer, R. L. Byer, W. R. Bosenberg, and J. W. Pierce. Quasi-phase-matched optical parametric oscillators in bulk periodically poled $LiNbO_3$. *Journal of the Optical Society of America B*, 12(11):2102–2116, 1995.

[26] M. M. Fejer, G. A. Magel, D. H. Jundt, and R. L. Byer. Quasi-phase-matched second harmonic generation: tuning and tolerances. *IEEE Journal of Quantum Electronics*, 28(11):2631–2654, 1992.

[27] R. H. Kingston. Parametric amplification and oscillation at optical frequencies. *Proceedings of IRE*, 50:472, 1962.

[28] R. L. Byer and A. Piskarskas. Optical parametric oscillation and amplification. *Journal of Optical Society of America B*, 10(9):1656–1656, 1993.

[29] M. H. Dunn and M. Ebrahimzadeh. Parametric generation of tunable light from continuous-wave to femtosecond pulses. *Science*, 286:1513–1517, 1999.

[30] M. Ebrahimzadeh and M. H. Dunn. Optical parametric oscillators. *OSA Handbook of Optics, McGraw-Hill, New York*, 4:2201–2712, 2000.

[31] S. E. Harris. Tunable optical parametric oscillators. *Proceedings of IEEE*, 57:2096–2113, 1969.

[32] M. Henriksson. *Nanosecond tandem optical parametric oscillators for mid-infrared generation*. Thesis dissertation, KTH, Sweden, 2006.

[33] N. P. Barnes and V. J. Corcoran. Parametric generation processes: spectral bandwidth and acceptance angles. *Applied Optics*, 15(3):696–699, 1976.

[34] V. G. Dimitriev and G. G. Gurzadyan. *Handbook of Nonlinear Optical Crystals*. Springer-Verlag, Berlin, Germany, 1991.

[35] G. D. Boyd, A. Ashkin, J. M. Dziedzic, and D. A. Kleinman. Second-harmonic generation of light with double refraction. *Physical Review*, 137(4A):A1305–A1320, Feb 1965.

[36] D. J. Kuizenga. Optimum focusing conditions for parametric gain in crystals with double refraction. *Applied Physics Letters*, 21:570–572, 1972.

[37] D. T. Reid, C. McGowan, M. Ebrahim-zadeh, and W. Sibbett. Characterization and modeling of a noncollinearly phase-matched femtosecond optical parametric oscillator based on KTA and operating beyond 4 μm. *IEEE journal of Quantum Electronics*, 33:1–9, 1997.

[38] P. E. Powers, C. L. Tang, and L. K. Cheng. High-repetition-rate femtosecond optical parametric oscillator based on RbTiOAsO_4. *Optics Letters*, 19(18):1439–1441, 1994.

[39] A. Ashkin, G. D. Boyd, J. M. Dziedzic, R. G. Smith, A. A. Ballman, J. J. Levinstein, and K. Nassau. Optically-induced refractive index inhomogeneities in $LiNbO_3$ and $LiTaO_3$. *Applied Physics Letters*, 9:72, 1966.

[40] Y. Furukawa, K. Kitamura, S. Takekawa, A. Miyamoto, M. Terao, and N. Suda. Photorefraction in $LiNbO_3$ as a function of $[Li]/[Nb]$ and MgO concentrations. *Applied Physics Letters*, 77:2494–6, 2000.

[41] Y. Furukawa, M. Sato, K. Kitamura, Y. Yajima, and M. Minakata. Optical damage resistance and crystal quality of $LiNbO_3$ single crystals with various $(Li)/(Nb)$ ratios. *Journal of Applied Physics*, 72:3250–4, 1992.

[42] M. Bass and D. W. Fradin. Surface and bulk laser-damage statistics and the identification of intrinsic breakdown processes. *IEEE journal of Quantum Electronics*, 9:890896, 1973.

[43] M. Ebrahim-zadeh, A. J. Henderson, and M. H. Dunn. An excimer-pumped $\beta - BaB_2O_4$ optical parametric oscillator tunable from 354 nm to 2.370 μm. *IEEE journal of Quantum Electronics*, 26:1241–1252, 1990.

[44] J. T. Verdeyen. *Lasers Electronics*. Third Ed., Prentice Hall, Englewood Cliffs, New Jersey, 1995.

[45] G. D. Boyd and D. A. Kleinman. Parametric interaction of focused gaussian light beams. *Journal of Applied Physics*, 39(8):3597–3639, 1968.

[46] C. C. Davis. *Lasers and Electro-Optics*. Cambridge University Press, Cambridge, 1996.

[47] K. Schneider, ∗P. Kramper, S. Schiller, and J. Mlynek. Toward an optical synthesizer: a single-frequency parametric oscillator using periodically poled $LiNbO_3$. *Optics Letters*, 22(17):1293–1295, 1997.

[48] M. E. Klein, C. K. Laue, D.-H. Lee, K.-J. Boller, and R. Wallenstein. Diode-pumped singly resonant continuous-wave optical parametric oscillator with wide continuous tuning of the near-infrared idler wave. *Optics Letters*, 25(7):490–492, 2000.

[49] T. Hatanaka, K. Nakamura, T. Taniuchi, H. Ito, Y. Furukawa, and K. Kitamura. Quasi-phase-matched optical parametric oscillation with periodically poled stoichiometric $LiTaO_3$. *Optics Letters*, 25(9):651–653, 2000.

[50] S.-Yu Tu, A. H. Kung, Z. D. Gao, and S. N. Zhu. Efficient periodically poled stoichiometric lithium tantalate optical parametric oscillator for the visible to near-infrared region. *Optics Letters*, 30(18):2451–2453, 2005.

[51] M. E. Klein, D.-H. Lee, J.-P. Meyn, B. Beier, K.-J. Boller, and R. Wallenstein. Diode-pumped continuous-wave widely tunable optical parametric oscillator based on periodically poled lithium tantalate. *Optics Letters*, 23(11):831–833, 1998.

[52] A. Bruner, D. Eger, M. B. Oron, P. Blau, M. Katz, and S. Ruschin. Temperature-dependent sellmeier equation for the refractive index of stoichiometric lithium tantalate. *Optics Letters*, 28(3):194–196, 2003.

[53] J. E. Bjorkholm, A. Ashkin, and R. G. Smith. Improvement of optical parametric oscillators by nonresonant pump reflection. *Quantum Electronics*, 6(12):797–799, 1970.

[54] D. S. Hum, R. K. Route, K. Urbanek, R. L. Byer, and M. M. Fejer. Generation of 10.5-W cw 532-nm radiation by SHG in vapor-transport-equilibrated, periodically-poled, near-stoichiometric lithium tantalate. In *Conference on Lasers and Electro-Optics/Quantum Electronics and Laser Science Conference and Photonic Applications Systems Technologies*, page CThG2. Optical Society of America, 2006.

[55] N. Ei Yu, S. Kurimura, Y. Nomura, and K. Kitamura. Stable high-power green light generation with thermally conductive periodically poled stoichiometric lithium tantalate. *Japanese Journal of Applied Physics*, 43(10A):L1265–L1267, 2004.

[56] M. Nakamura, S. Takekawa, K. Terabe, K. Kitamura, T. Usami, H. Ito, and Y. Furukawa. Near-stoichiometric $LiTaO_3$ for bulk quasi-phase-matched devices. *Ferroelectrics*, 273(6):199–204, 2002.

[57] M. Katz, R. K. Route, D. S. Hum, K. R. Parameswaran, G. D. Miller, and M. M. Fejer. Vapor-transport equilibrated near-stoichiometric lithium tantalate for frequency-conversion applications. *Optics Letters.*, 29(15):1775–1777, 2004.

[58] G. K. Samanta, G. R. Fayaz, Z. Sun, and M. Ebrahim-Zadeh. High-power, continuous-wave, singly resonant optical parametric oscillator based on mgo:spplt. *Optics Letters*, 32(4):400–402, 2007.

[59] J. E. Bjorkholm. Some effects of spatially nonuniform pumping in pulsed optical parametric oscillators. *Quantum Electronics*, 3(7):109–118, 1971.

[60] A. Henderson and R. Stafford. Intra-cavity power effects in singly resonant cw OPOs. *Applied Physics B: Lasers and Optics*, 85(2–3):181–184, 2006.

[61] T. Takakura, K. Iga, and T. Tako. Linewidth measurement of a single longitudinal mode AlGaAs laser with fabry-perot interferometer. *Japanese Journal of Applied Physics*, 19(12):L725–L727, 1980.

[62] M. Fujise and M. Ichikawa. Linewidth measurement of a 1.5 μm range DFB laser. *Electronics Letters*, 19(6):231–232, 1985.

[63] J. Hirohashi, V. Pasiskevicius, S. Wang, and F. Laurell. Picosecond blue-light-induced infrared absorption in single-domain and periodically poled ferroelectrics. *Journal of Applied Physics*, 101(033105):1–3, 2007.

[64] K. Sakai, Y. Koyata, and Y. Hirano. Blue light generation in a ridge waveguide MgO:LiNbO−3 crystal pumped by a fiber bragg grating stabilized laser diode. *Optics Letters*, 32(16):2342–2344, 2007.

[65] C. Czeranowsky, E. Heumann, and G. Huber. All-solid-state continuous-wave frequency-doubled Nd:YAG BiBO laser with 2.8-W output power at 473 nm. *Optics Letters*, 28(6):432–434, 2003.

[66] Q. H. Xue, Q. Zheng, Y. K. Bu, F. Q. Jia, and L. S. Qian. High-power efficient diode-pumped Nd:YVO_4/LiB_3O_5 457 nm blue laser with 4.6 W of output power. *Optics Letters*, 31(8):1070–1072, 2006.

[67] F. Falcoz, F. Balembois, P. Georges, A. Brun, and D. Rytz. All-solid-state continuous-wave tunable blue-light source by intracavity doubling of a diode-pumped Cr:LiSAF laser. *Optics Letters*, 20(11):1274–1276, 1995.

[68] Masood Ghotbi and M. Ebrahim-Zadeh. Optical second harmonic generation properties of BiB_3O_6. *Optics Express*, 12(24):6002–6019, 2004.

[69] M. Ghotbi and M. Ebrahim-Zadeh. 990 mw average power, 52% efficient, high-repetition-rate picosecond-pulse generation in the blue with BiB_3O_6. *Optics Letters*, 30(24):3395–3397, 2005.

[70] G. K. Samanta, G. R. Fayaz, and M. Ebrahim-Zadeh. 1.59 W, single-frequency, continuous-wave optical parametric oscillator based on MgO:sPPLT. *Optics Letters*, 32(17):2623–2625, 2007.

[71] H. Furuya, A. Morikawa, K. Mizuuchi, and K. Yamamoto. High-beam-quality continuous wave 3 W green-light generation in bulk periodically poled MgO:$LiNbO_3$. *Japanese Journal of Applied Physics*, 45(8B):6704–6707, 2006.

[72] F. J. Kontur, I. Dajani, Yalin Lu, and R. J. Knize. Frequency-doubling of a cw fiber laser using PPKTP, PPMgSLT, and PPMgLN. *Optics Express*, 15(20):12882–12889, 2007.

[73] S. V. Tovstonog, S. Kurimura, I. Suzuki, K. Takeno, S. Moriwaki, N. Ohmae, N. Mio, and T. Katagai. Thermal effects in high-power CW second harmonic generation in mg-doped stoichiometric lithium tantalate. *Optics Express*, 16(15):11294–11299, 2008.

[74] S. Greenstein and M. Rosenbluh. Dynamics of cw intra-cavity second harmonic generation by PPKTP. *Optics Communications*, 238(4-6):319–327, 2004.

[75] R. Le Targat, J.-J. Zondy, and P. Lemonde. 75% -efficient blue generation from an intracavity PPKTP frequency doubler. *Optics Communications*, 247(4-6):471–481, 2005.

[76] Z. Sun, G. K. Samanta, G R. Fayaz, M. Ebrahim-Zadeh, C Canalias, V. Pasiskevicius, and F Laurell. Efficient generation of tunable cw single frequency green radiation by second harmonic generation in periodically-poled $KTiOPO_4$. In *Conference on Lasers and Electro-Optics/Quantum Electronics and Laser Science Conference and Photonic Applications Systems Technologies*, page CTuK1. Optical Society of America, 2007.

[77] G. R. Fayaz, M. Ghotbi, and M. Ebrahim-Zadeh. Efficient second-harmonic generation of tunable femtosecond pulses into the blue in periodically poled KTP. *Applied Physics Letters*, 86(6):061110, 2005.

[78] Z. M. Liao, S. A. Payne, J. Dawson, A. Drobshoff, C. Ebbers, D. Pennington, and L. Taylor. Thermally induced dephasing in periodically poled KTP frequency-doubling crystals. *Journal of the Optical Society of America B*, 21(12):2191–2196, 2004.

[79] K. Kato and E. Takaoka. Sellmeier and thermo-optic dispersion formulas for ktp. *Applied Optics*, 41(24):5040–5044, 2002.

[80] M. V. Pack, D. J. Armstrong, and A. V. Smith. Measurement of the $\chi^{(}2)$ tensors of $KTiOPO_4$, $KTiOAsO_4$, $RbTiOPO_4$, and $RbTiOAsO_4$ crystals. *Applied Optics*, 43(16):3319–3323, 2004.

[81] C. Canalias, S. Wang, V. Pasiskevicius, and F. Laurell. Nucleation and growth of periodic domains during electric field poling in flux-grown $KTiOPO_4$ observed by atomic force microscopy. *Applied Physics Letters*, 88(3):0329053, 2006.

[82] J. D. Bierlein and H. Vanherzeele. Potassium titanyl phosphate: properties and new applications. *Journal of the Optical Society of America B*, 6(4):622–633, 1989.

[83] G. Hansson, H. Karlsson, S. Wang, and F. Laurell. Transmission measurements in KTP and isomorphic compounds. *Applied Optics*, 39(27):5058–5069, 2000.

[84] Z. M. Liao, S. A. Payne, J. Dawson, A. Drobshoff, C. Ebbers, D. Pennington, and L. Taylor. Thermally induced dephasing in periodically poled KTP frequency-doubling crystals. *Journal of the Optical Society of America B*, 21(12):2191–2196, 2004.

[85] K. Kitamura, Y. Furukawa, S. Takekawa, T. Hatanaka, H. Ito, and V. Gopalan. Non-stoichiometric control of $LiNbO_3$ and $LiTaO_3$ in ferroelectric domain engineering for optical devices. *Ferroelectrics*, 257:235–243, 2001.

[86] D. S. Hum, R. K. Route, G. D. Miller, V. Kondilenko, A. Alexandrovski, J. Huang, K. Urbanek, R. L. Byer, and M. M. Fejer. Non-stoichiometric control of $LiNbO_3$ and $LiTaO_3$ in ferroelectric domain engineering for optical devices. *Journal of Applied Physics*, 101(9):093108, 2007.

[87] S. V. Tovstonog, S. Kurimura, I. Suzuki, K. Takeno, S. Moriwaki, N. Ohmae, N. Mio, and T. Katagai. Thermal effects in high-power CW second harmonic generation in Mg-doped stoichiometric lithium tantalate. *Optics Express*, 16(15):11294–11299, 2008.

[88] G. K. Samanta and M. Ebrahim-Zadeh. Continuous-wave singly-resonant optical parametric oscillator with resonant wave coupling. *Optics Express*, 16(10):6883–6888, 2008.

[89] P. Gross, M. E. Klein, T. Walde, K.-J. Boller, M. Auerbach, P. Wessels, and C. Fallnich. Fiber-laser-pumped continuous-wave singly resonant optical parametric oscillator. *Optics Letters.*, 27(6):418–420, 2002.

[90] I. Lindsay, B. Adhimoolam, P. Groß, M. Klein, and K. Boller. 110 GHz rapid, continuous tuning from an optical parametric oscillator pumped by a fiber-amplified DBR diode laser. *Optics Express*, 13(4):1234–1239, 2005.

[91] A. Henderson and R. Stafford. Low threshold, singly-resonant cw OPO pumped by an all-fiber pump source. *Optics Express*, 14(2):767–772, 2006.

[92] G. K. Samanta, S. Chaitanya Kumar, and M. Ebrahim-Zadeh. Stable, 9.6 W, continuous-wave, single-frequency, fiber-based green source at 532 nm. *Optics Letters*, (34)(10):1561–1563, 2009.

[93] G. K. Samanta, S. Chaitanya Kumar, M. Mathew, C. Canalias, V. Pasiskevicius, F. Laurell, and M. Ebrahim-Zadeh. High-power, continuous-wave, second-harmonic generation at 532 nm in periodically poled $KTiOPO_4$. *Optics Letters*, 33(24):2955–2957, 2008.

[94] Y. Furukawa, K. Kitamura, A. Alexandrovski, R. K. Route, and M. M. Fejer. Green-induced infrared absorption in MgO doped $LiNbO_3$. *Applied Physics Letters*, 78(14):1970–1972, 2001.

[95] D. Wright. Beamwidths of a diffracted laser using four proposed methods. *Optical and Quantum Electronics*, 24(9):S1129–S1135, 1992.